Shadows of Kerr–de Sitter naked singularities

Zdeněk Stuchlík[*] and Daniel Charbulák[†]

Research Centre for Theoretical Physics and Astrophysics, Institute of Physics, Silesian University in Opava, Bezručovo nám. 13, CZ-746 01 Opava, Czech Republic

(Received 3 November 2021; revised 27 September 2023; accepted 29 January 2024; published 5 March 2024)

We present a classification of Kerr–de Sitter spacetimes based on the presence of horizons, ergospheres, and the characteristics of photon motion. We utilize the concept of local escape cones for isotropically radiating point sources to create shadows of the Kerr–de Sitter naked singularities within a class containing astrophysically relevant parameters. For completeness, we also consider in the construction photons entering the region of negative radii of the naked singularity spacetimes. The shadow construction is associated with two astrophysically significant families of local reference frames (or local observers). The first family represents locally nonrotating frames that, near the so-called static radius in Kerr–de Sitter spacetimes, exhibit characteristics similar to those of static observers at large distances in asymptotically flat spacetimes. The second family involves radially escaping geodesic frames, which are suitable for constructing the shadow near the cosmological horizon of Kerr–de Sitter spacetimes. We explore how the aberration effect, caused by the motion of free observers due to the repulsive influence of the cosmological constant, modifies the shadow in comparison to those related to stationary locally nonrotating observers.

DOI: 10.1103/PhysRevD.109.064008

I. INTRODUCTION

The appearance of the shadow of a black hole (BH) has generated considerable interest in the astrophysical community, especially after the first image of the neighborhood of the BH located at the center of the galaxy M87 was taken by the Event Horizon Telescope (EHT) [1–8], and we can therefore expect a further increase in this interest after the image of the neighborhood of the BH at the center of our Galaxy, known as the source SgrA* [9–14].

Starting from the pioneering work on the modeling the shadow shape of BHs in the asymptotically flat spacetimes, namely nonrotating Schwarzschild BHs [15,16], the Schwarzschild BHs surrounded by an accretion disk [17], and the rotating Kerr BHs [18–20], shadows of BHs or other compact (no-horizon) objects, such as wormholes, have been modeled in the framework of general relativity (GR) by considering many variants of the BH configurations, using different spacetime geometries, with or without the presence of matter, using different approaches, and also using alternative theories of gravity [21].

For example, the braneworld Kerr-Newman BHs have been studied in [22–26]. Of particular interest are optical phenomena around the regular BHs [27,28] constructed in the framework of GR combined with various variants of nonlinear electrodynamics [29–33]. BHs surrounded by the test fields or dark matter were examined in [34–39]. Some remarkable results have been obtained in alternative models of gravity, including the M-theory [40], Einstein-Æther theory [41], Einstein-Cartan-Sciama-Kibble theory [42], or Gauss-Bonnet gravity [43]. A comprehensive review of variants of BH spacetimes in which the optical phenomena have been studied, can be found in [44].

The shadows associated with the no-horizon compact objects have also been studied for spherically symmetric naked singularities (NSs) [45,46], deformed NSs [47], wormholes [48–52], Kerr NSs [53,54], braneworld Kerr-Newman NSs [55–57], or standard Kerr-Newman BH and NS [15,58]. So-called BH impostors have also been treated, e.g., in [59].

Considerable effort has also gone into finding an alternative to the Kerr NS spacetime, which does not show the region of causality violations (time machine [60]), which is predicted to be in the vicinity of the ring singularity [61]. For this reason, "stringy" solutions corresponding to rapidly rotating compact objects, so-called superspinars, have been introduced, where the interior is described by assumed stringy effects, and the exterior is described by the standard Kerr NS geometry [62–64]; their astrophysical properties have been studied in [65,66]. The pathological causality violation region is then covered by the correctly behaving region, the boundary of the inner solution is expected at a radius $r \geq 0$. Optical phenomena associated with Kerr superspinars have been studied in [53,54], where it has been shown that the superspinar shadow depends on the position of the boundary of the external Kerr spacetime and

[*]zdenek.stuchlik@physics.slu.cz
[†]daniel.charbulak@physics.slu.cz

 © 2024 American Physical Society

differs significantly from the BH shadow. The distinction between Kerr NSs and BHs has been studied in [54,66,67].

A comprehensive review of analytical studies of the shadows of BHs and other compact objects with a presentation of different approaches has recently been published in [68]. A common feature of these studies is the focus on the area of the photon spheres in the case of spherically symmetric spacetimes, or photon shells in the case of the axially symmetric and stationary spacetimes, surrounding the central gravitating objects, as they play a crucial role in defining the shadow.

The validity of the weak cosmic censorship conjecture, which forbids the appearance of naked singularities, clothing each one in an event horizon [69], is still an open question [70,71]. The conversion of a BH into a NS due to particle capture or perturbation processes seems highly improbable as possible conversions due to perturbations considered in the linear regime [72–74] are corrected by the inclusion of backreaction (second order) effects [75–80]. However, it has been shown that gravitational collapse can lead to NSs [81–84], and, furthermore, the Kerr superspinars having exterior with the Kerr NS geometry can be considered as primordial, being remnants of the initial stringy phase of the evolution of the Universe [62,63,66,85]. Therefore, we believe that it is worthwhile to study the construction of the shadow of both the complete Kerr NS spacetimes and the Kerr superspinars to test their observational relevance, as we can expect that in the near future we will be able to distinguish very subtle details of the compact objects due to the use of the long baseline interferometric measurements.

The accelerated expansion of the Universe caused by dark energy, that can be related to the vacuum energy [86], can be conveniently represented by the relic cosmological constant [87]. This constant is thought to have a significant impact not only in cosmology [15,88,89], but also in astrophysical processes related to the formation of large galaxies and the accretion onto supermassive black holes [90–94], as well as on the dark matter halos in large galaxies or their clusters [95,96]. Therefore, the shadows of BHs in asymptotically de Sitter spacetimes, specifically those of Kerr–de Sitter (KdS) BHs, were found for locally nonrotating reference frames (LNRFs), frames related to circular geodesic orbits, and for radially freely falling/escaping (geodesic) frames [97]. For an alternative KdS BH solution and its shadow see [98,99]. Furthermore, the impact of the observer's state of motion on the BH shadow was considered, including that of the Sgr A*, as described in [100]. In other recent works, BHs embedded in the expanding de Sitter universe have been studied in [101–103], including rotating [97] and charged and rotating BHs [104], while the connection with the Friedman-Lemaître-Robertson-Walker cosmological metric has been considered in [105].

In the present paper we deal with the shadow of KdS NS spacetimes, taking into account also the photons entering the sheet of $r < 0$ in terms of the complete Kerr geometry—we must stress that, for completeness, we also consider the influence of this region, which is controversial because it requires reinterpretation of the Kerr geometry for distant observers at $r < 0$, and it also includes the causality violation region [61]. Therefore, in the calculations of the KdS NS shadow we consider the ring singularity at $r = 0$, $\theta = \pi/2$, and photons moving in both the sheets $r > 0$ and $r < 0$, focusing attention on the special class of the KdS NS spacetimes (see Sec. III D 3) that enables the existence of spherical photon shells at radii $r < 0$, which determine the shadow along with the spherical photon shells at $r > 0$.

Various methods exist for calculating the shadow of compact objects, including one which incorporates astrometric observables [106]. In this study, we employ the concept of light escape cones (LECs) and complementary light capture cones (LCCs) related to the locally nonrotating frames (LNRFs) to determine the shadow. In a given reference frame, the LEC (LCC) is defined as the set of directions, given by the directional angles related to the frame sky, of the emitted photons that escape to infinity (cannot escape to infinity). The LNRFs are a very convenient platform for describing the optical effects [18], representing the most natural generalization of the static observers of the Schwarzschild spacetimes, and a relevant tool in studies of astrophysical phenomena in the vicinity of rotating black holes [19]. Of course, the shadow of a compact object (a BH or a NS) can be constructed for any observer moving in the spacetime related to the compact object. Usually, we construct the shadow as seen by distant free observers, i.e., observers for whom the relativistic effects can be considered negligible, namely observers located on Earth. In the asymptotically flat Kerr spacetimes, the distant observers are ideally realized by the static observers (LNRFs) at infinity. The KdS spacetimes are not asymptotically flat, so to keep the similarity with the Kerr spacetimes, we have to look for a region that can be considered as nearly flat, where free observers can be defined as being nearly static. Intuitively, it is clear that in an expanding universe such near-flat regions correspond to the outer regions and close vicinity of gravitationally bound systems such as galaxies and their clusters, where the influence of gravity and universe expansion is sufficiently suppressed. Of course, the situation is quite different for an observer orbiting close to a K(dS)BH or NS with or without an accretion disk [54,57,97]. For the construction of the shadow for BH objects in the expanding universe with the cosmological constant (see [102]).

We follow the KdS BH shadow calculation method used in [97], where the LECs were calculated relative to different reference frames, namely the accelerated LNRFs, the geodesic radially falling/escaping frames, and the circular geodesic frames. In this paper, due to the extended

variability and complexity of the KdS NS spacetimes, we limit ourselves to the KdS NS spacetimes of the class containing the parameters allowed by the observational constraints, given namely by enormously low value of the relic cosmological constant ($\Lambda \sim 10^{-52}$ m^{-2}) implied by cosmic observations, and the constraints on the mass and spin of the compact object given by observations of active galactic nuclei in large galaxies, or even by the whole galactic clusters [93,95]. This class of KdS NS spacetimes allows the existence of the so-called static radius [88,91,94,107,108]—the spacetime at and around this radius represents the best local approximation to the asymptotically flat region of the Kerr spacetimes [107,108]; the static radius also represents an upper limit on the extent of gravitationally bound systems (dark matter halos) in spacetimes with the relic cosmological constant [95,109]. At the static radius, the LNRF observers can be thought of as geodesic stationary observers located at an unstable equilibrium point where the gravitational attraction of the central object is just balanced by the cosmic repulsion of the dark energy (cosmological constant).

To simulate the appearance of the KdS NS shadow to a freely escaping observer near the cosmological horizon, we use the radially escaping geodesic reference frames, which move purely radially relative to the LNRFs [54].

The concept of LECs (and complementary LCC) allows to construct the BH or NS shadows relative to any observer, including those orbiting very close to the central object (see, e.g., [54,57]). Here we consider the standard case of a shadow (silhouette) cast by a compact object located between a very distant observer and an illuminating source much larger than the compact object [18]. To construct the LEC and the shadow, we assume the source of light (emitter) located at the position of the observer and study the motion of photons emitted in different directions. We then use the results of the LEC construction to construct the shadows. In our analysis we concentrate on special classes of geodesics, namely so-called principal null congruence geodesics remaining on fixed latitude [88], and in particular the null geodesics corresponding to the spherical photon orbits, which can be located in regions of both positive and negative radii.

The present paper is organized as follows. In Sec. II we briefly summarize the basic geometric properties of the KdS backgrounds, namely, the event horizons and the ergosphere, and present the corresponding separation of the KdS spacetimes in the $(a^2 - y)$–parameter plane. This separation is related to the classification of the KdS spacetimes introduced in [110]. In the following, the construction of the shadow refers only to the KdS NS spacetimes with parameters that are realistic from the point of view of astrophysics, i.e., with the relict cosmological constant and masses observed in the centers of active galactic nuclei. In such spacetimes, at the so-called static radius, the gravitational attraction of the central object is just balanced by the cosmic repulsion [111]. In Sec. III we study the motion of photons entering the region of negative radii in the selected class of the KdS NS spacetimes, thus extending the detailed study of [110] concentrated on the region of positive radii. First, the constants of the photon motion are introduced and the Carter equations of motion are presented. Then the range of allowed motion constants is investigated. Furthermore, special photon trajectories are studied, namely, constant latitude trajectories and the spherical photon orbits (SPOs). A special subsection is devoted to the study of the locally measured orientation of the SPOs with respect to the azimuthal direction, including orbits in the region of negative radii. In Sec. IV the directional angles of photons in the LNRFs are defined and their relation to the motion constants is established. The section concludes with the construction of the NS shadows as seen in LNRFs located at the static radius, which is chosen because it represents, together with its surroundings, the best local approximation to flat spacetime in the KdS spacetimes [107,108]. In Sec. V the local reference frames radially moving (escaping) in the LNRFs are introduced, following geodesics of the spacetime, and the shadow is constructed in these frames as they approach the cosmological horizon. Section VI presents a discussion and some conclusions.

II. KERR–DE SITTER GEOMETRY AND ITS BASIC PROPERTIES

The Kerr–de Sitter spacetimes [61] are determined by the mass parameter M, the spin parameter $a = J/M$, where J is the angular momentum of the central object, and the cosmological constant Λ, which can be conveniently replaced by the dimensionless cosmological parameter $y = \frac{1}{3}\Lambda M^2$.

A. Line element

To describe the Kerr–de Sitter geometry we use the standard Boyer-Lindquist spheroidal coordinates t, r, θ, ϕ, expressed in the geometric unit system with $c = G = 1$. In the following, for simplicity, we use the dimensionless ratios of the parameter a introduced above and coordinates—$s/M \to s, t/M \to t, r/M \to r, a/M \to a$. In the following we assume $M > 0, a > 0$, $\Lambda > 0$. The line element of the geometry then takes the form [88,89]

$$\begin{aligned} \mathrm{d}s^2 = &-\frac{\Delta_r}{I^2\rho^2}(\mathrm{d}t - a\sin^2\theta\mathrm{d}\phi)^2 \\ &+\frac{\Delta_\theta \sin^2\theta}{I^2\rho^2}[a\mathrm{d}t - (r^2 + a^2)\mathrm{d}\phi]^2 \\ &+\frac{\rho^2}{\Delta_r}\mathrm{d}r^2 + \frac{\rho^2}{\Delta_\theta}\mathrm{d}\theta^2, \end{aligned} \tag{1}$$

where

$$\Delta_r = (1 - yr^2)(r^2 + a^2) - 2r, \tag{2}$$

$$\Delta_\theta = 1 + a^2 y \cos^2\theta, \tag{3}$$

$$I = 1 + a^2 y, \tag{4}$$

$$\rho^2 = r^2 + a^2 \cos^2\theta. \tag{5}$$

B. Singularities

The behavior of the Riemann invariant $R_{\alpha\beta\gamma\delta}R^{\alpha\beta\gamma\delta}$ of the Kerr–de Sitter geometry [61] demonstrates the existence of a physical singularity determined by the condition,

$$\rho^2 = 0, \tag{6}$$

which is satisfied when

$$r = 0, \qquad \cos\theta = 0. \tag{7}$$

Thus the singularity is a ring of radius a located in the equatorial plane $\theta = \pi/2$. Using the interior of the ring singularity, the Kerr–de Sitter geometry can be extended into the region of negative radii, see, e.g., [61,112–114].

C. Horizons

The coordinate pseudosingularities of the KdS geometry occur at radii where

$$\Delta_r = 0 \tag{8}$$

and define the horizons of the KdS spacetimes. Equation (8) can alternatively be written in the form

$$a^2 = a_h^2(r;y) \equiv \frac{yr^4 - r^2 + 2r}{1 - yr^2}. \tag{9}$$

The function $a_h^2(r;y)$ was analyzed in [108]—here we present a summary of the results of that paper.

In the following we concentrate on the study of the repulsive cosmological constant, i.e., we assume $y > 0$. Then the function $a_h^2(r;y)$ defined in the relation (9) has two divergent points

$$r_{d(h)}^{\pm} = \pm\frac{1}{\sqrt{y}}, \tag{10}$$

which represents limits on the loci of the cosmological horizons—the radius $r_{d(h)}^{+} = 1/\sqrt{y}$ limits the cosmological horizon at the region of positive radii, while $r_{d(h)}^{-} = -1/\sqrt{y}$ limits the secondary cosmological horizon at the region of negative radii.

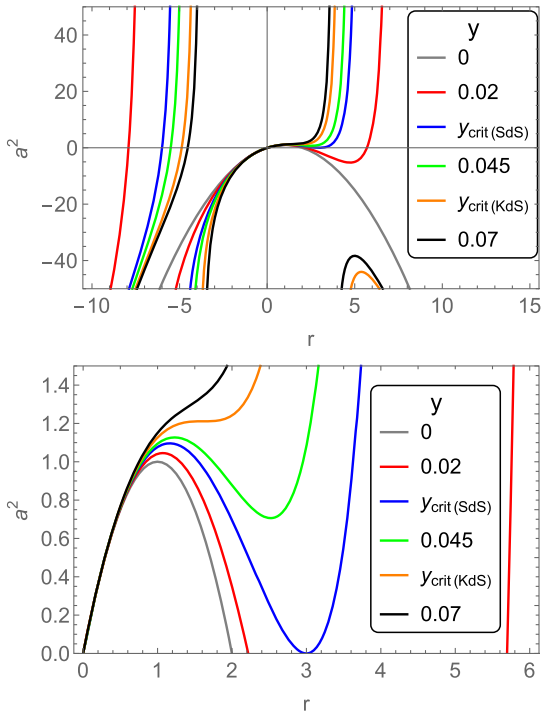

FIG. 1. Top: plot of the functions $a_h^2(r;y)$ given for some appropriately chosen values of the cosmological parameter y. These functions are steeply increasing near the discontinuity point at $r = r_{d(h)}^{-} = -1/\sqrt{y}$, where $a_h^2(r;y) \to +\infty$ as $r \to r_{d(h)}^{-}$ from the left, which is illustrated by the almost vertical lines at $r < 0$. Bottom: the same in detail focusing on the region $r > 0$ and the admissible part $a^2 > 0$.

The behavior of the function $a_h^2(r;y)$ is illustrated in Fig. 1. It must be emphasized that only the regions where $a^2 \geq 0$ are physically relevant.

The separation of the KdS spacetimes is governed by the existence of the local extrema of the function $a_h^2(r;y)$ depending on the cosmological parameter y, i.e., the local maximum, $a_{\max(h)}^2(y)$, and the local minimum, $a_{\min(h)}^2(y)$, induce the partition into the BH and NS spacetimes in the parameter space $(a^2 - y)$ [108]. We therefore present the following classification.

(1) Case $0 < y \leq y_{\rm crit}(\mathrm{SdS}) \equiv 1/27 \doteq 0.03704$
   (i) The function $a_h^2(r;y)$ has a positive maximum $a_{\max(h)}^2(y) > 0$ and negative minimum $a_{\min(h)}^2(y) < 0$ (see the red curve in Fig. 1).
   (ii) for $y = y_{\rm crit(SdS)}$, $a_{\min(h)}^2(y) = 0$ (see the blue curve in Fig. 1); $y_{\rm crit(SdS)}$ denotes the critical value of the cosmological parameter which allows existence of the Schwarzschild-de Sitter BH spacetimes.
   (a) $0 < a^2 < a_{\max(h)}^2(y)$
   The geometry describes a BH spacetimes; Eq. (8) has four real distinct roots

$r_c^- < 0 < r_i < r_o < r_c$, corresponding respectively to the radius of the secondary cosmological horizon in the region $r < 0$, the inner BH horizon, the outer BH horizon and the cosmological horizon (at the standard region of positive radii).

(b) $a^2 = a^2_{\mathrm{max}(h)}(y)$
Extreme BH spacetimes where the inner and outer BH horizons merge, $r_i = r_o$.

(c) $a^2_{\mathrm{max}(h)}(y) < a^2$
The geometry describes the NS spacetimes, which are only equipped with the two cosmological horizons $r_c^- < 0 < r_c$.

(2) Case $y_{\mathrm{crit}}(\mathrm{SdS}) < y \le y_{\mathrm{crit}}(\mathrm{KdS})$

$$\equiv 16(26\sqrt{3} - 45)/9 \doteq 0.05924$$

(i) The function $a_h^2(r; y)$ has both local extrema $a^2_{\mathrm{max}(h)}(y)$ and $a^2_{\mathrm{min}(h)}$ positive, $0 < a^2_{\mathrm{min}(h)} < a^2_{\mathrm{max}(h)}(y)$ (see green curve in Fig. 1)—these extrema converge for $y = y_{\mathrm{crit}}(\mathrm{KdS})$ to an inflection point at

$$a^2_{\mathrm{crit}} \equiv 3(3 + 2\sqrt{3})/16 \doteq 1.21202$$

(see the orange curve in Fig. 1); $y_{\mathrm{crit}}(\mathrm{KdS})$ and a^2_{crit} denote the critical values of the cosmological parameter and the spin parameter, respectively, for which the Kerr–de Sitter BH spacetimes can still exist.

(a) $a^2 < a^2_{\mathrm{min}(h)}(y)$ or $a^2_{\mathrm{max}(h)}(y) < a^2$
The geometry describes a NS spacetimes with two cosmological horizons, as in the previous NS case.

(b) $a^2_{\mathrm{min}(h)}(y) < a^2_{\mathrm{max}(h)}(y)$
The geometry describes a BH spacetimes with two cosmological horizons and two BH horizons as in the previous BH case.

(3) Case $y > y_{\mathrm{crit}}(\mathrm{KdS})$
The function $a_h^2(r; y)$ has no local extrema (see the black curve in Fig. 1), and the geometry describes NS spacetimes with two cosmological horizons as in the previous NS cases.

For completeness, we also describe all limit cases of BH-NS spacetimes.

The limit case $a^2 = a^2_{\mathrm{min}(h)}(y)$ corresponds to the coalescence of the BH outer horizon and the cosmological horizon $r_o = r_c$—the marginal NS spacetime.

The limit case $a^2 = a^2_{\mathrm{max}(h)}(y)$ corresponds to the merging of the inner and outer BH horizons $r_i = r_o$—the extreme BH spacetime.

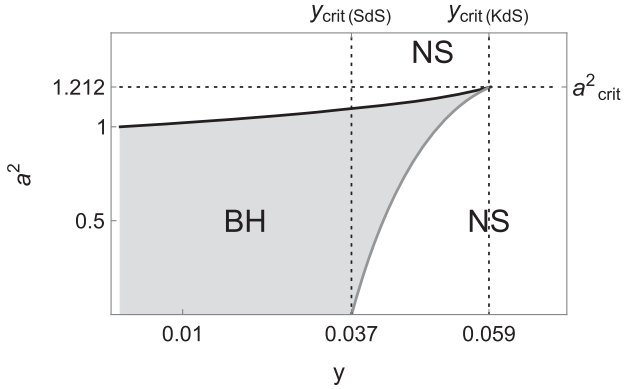

FIG. 2. Plot of the functions $a^2_{\mathrm{max}(h)}(y)$ (black curve) and $a^2_{\mathrm{min}(h)}(y)$ (gray curve) and the induced partition of the KdS spacetimes into the KdS BH spacetimes (gray area) and the KdS NS spacetimes (white area). Critical values of the spacetime parameters are included.

The extreme case $y = y_{\mathrm{crit(KdS)}}$ and $a^2 = a^2_{\mathrm{crit}}$ corresponds to the ultraextreme NS spacetime with $r_i = r_o = r_c$ [108].

The behavior of the local extrema $a^2_{\mathrm{max}(h)}(y)$ and $a^2_{\mathrm{min}(h)}(y)$ as a function of the cosmological parameter y is shown in Fig. 2.

In this article we pay special attention to the sheet of negative r, so we specify the position of the secondary cosmological horizon r_c^-. Its position should be constrained by the relations $r^-_{z(h)} < r_c^- < r^-_{d(h)} < 0$, where $r^-_{z(h)} < 0$ is the zero point of the function $a_h^2(r, y)$, which is located at

$$r^-_{z(h)} = \begin{cases} \frac{-2}{\sqrt{3y}} \cos\left[\frac{1}{3}\arccos\sqrt{27y}\right], & \text{for } y \le y_{\mathrm{crit}}(\mathrm{SdS}) \\ \frac{-2}{\sqrt{3y}} \cosh\left[\frac{1}{3}\,\mathrm{arg\,cosh}\sqrt{27y}\right], & \text{for } y > y_{\mathrm{crit}}(\mathrm{SdS}), \end{cases} \tag{11}$$

and the upper limit $r^-_{d(h)}$ is the negative one from the two divergent points $r^{\pm}_{d(h)} = \pm 1/\sqrt{y}$ of the function $a_h^2(r; y)$. Note that the negative roots $r^-_{z(h)}$ of the function $a_h^2(r; y)$ can have no physical meaning by themselves, since no analytic extension of the Schwarzschild–de Sitter manifold ($a^2 = 0, y > 0$) to negative radii over the ring singularity at $r = 0$ exists. In the pure Kerr spacetimes ($a^2 > 0, y = 0$) there are at most two positive roots of Eq. (8).

D. Ergosphere

The ergosphere is the space-time region that allows the extraction of rotational energy, which is part of the total gravitational mass M, from the BH or NS by the so-called Penrose process and its variants [19,115–120]. In the

ergosphere also photons with negative covariant energy can exist [97,110], allowing the so-called radiative Penrose process [115]. The ergosphere is bounded by the surfaces of the static limit (ergosurfaces) and the horizons [61,97,108]. All matter within the ergosphere is dragged by the rotation of spacetime and is corotating in the positive ϕ-direction, with an angular velocity of $\Omega = \frac{d\phi}{dt} > 0$ [15]. Matter in the ergosphere corotates relative to observers whose proper time is equal to or very close to the coordinate time. In the asymptotically flat Kerr spacetimes, the coordinate time t is the proper time of static observers at infinity (and very close for static distant observers). In the KdS spacetimes the coordinate time t is close to the proper time of static observers in unstable equilibrium at the static radius, where the spacetime is closest to the flat spacetime [107].

For the Kerr spacetimes, the ergosphere has recently been studied in [121–125], the influence of the cosmological constant has been studied, e.g., in [56,108,126]. Here we briefly discuss for the KdS NS spacetimes the existence and extension of the ergosphere as a function of on the spacetime parameters a^2, y and its relation to other relevant surfaces representing the spacetimes.

The ergoshere is characterized by the condition $g_{tt} > 0$. Its boundary, i.e., the ergosurface (the surface of the static limit) is given by the condition,

$$g_{tt} \equiv \frac{a^2 \sin^2\theta \Delta_\theta - \Delta_r}{I^2\rho^2} = 0, \tag{12}$$

which leads to a quartic equation with respect to the variable r. However, in the equatorial plane ($\theta = \pi/2$) that is of most interest because of the strongest effects induced by the rotation of the spacetime; Eq. (12) is reduced to

$$a^2 - \Delta_r = 0, \tag{13}$$

which has the solution

$$r = 0, \tag{14}$$

independent of the space-time parameters, while the other solutions are given by the cubic equation

$$yr^3 + (a^2 y - 1)r + 2 = 0. \tag{15}$$

In the case $y > 0$, Eq. (15) always has just one negative root $r^{(-)}_{\rm erg}$, which reads

$$r^{(-)}_{\rm erg} = \begin{cases} -2\sqrt{\frac{1-a^2y}{3y}}\cos\left[\frac{1}{3}\arccos\sqrt{\frac{27y}{(1-a^2y)^3}}\right], & \text{for } a^2 < 1/y; \\ -\sqrt[3]{\frac{2}{y}}, & \text{for } a^2 = 1/y; \\ -2\sqrt{\frac{a^2y-1}{3y}}\sinh\left[\frac{1}{3}\sinh^{-1}\sqrt{\frac{27y}{(a^2y-1)^3}}\right], & \text{for } a^2 > 1/y. \end{cases} \tag{16}$$

Under the conditions we are dealing with, $a^2 > 0$, $y > 0$, the inequality $r^-_{(c)} < r^{(-)}_{\rm erg} < 0$ holds; these surfaces thus restrict the ergoregion in the region of negative radii, $r < 0$—this part of the ergoregion lies between the cosmological horizon and the ergosurface that touches the cosmological horizon at the symmetry axis $\theta = 0, \pi$. Note that the ergoregion at negative radii has character independent of the spacetime parameters. In the following discussion we concentrate on the properties of the ergosurfaces in the region of positive radii, $r > 0$.

If $0 < a^2 < a^2_{{\rm erg}-s}(y)$ and $0 < y < y_{\rm crit(SdS)}$, then Eq. (15) has, in addition to the negative solution (16), two positive roots $r^{\pm}_{\rm erg}$, which read

$$r^{\pm}_{\rm erg} = 2\sqrt{\frac{1-a^2y}{3y}}\cos\left[\frac{\pi}{3} \pm \frac{1}{3}\arccos\sqrt{\frac{27y}{(1-a^2y)^3}}\right], \tag{17}$$

which satisfies the relation $0 < r^+_{\rm erg} < r^-_{\rm erg}$. Here the function $a^2_{{\rm erg}-s}(y)$, which is related to the existence of the ergosphere, is given in the form

$$a^2_{{\rm erg}-s}(y) \equiv \frac{1 - 3y^{1/3}}{y}. \tag{18}$$

In the relevant interval $0 < y \le y_{\rm crit(SdS)}$, where the function $a^2_{{\rm erg}-s}(y)$ takes positive values, $0 \le a^2_{{\rm erg}-s}(y) < 1/y$. The critical parameter $y_{\rm crit(SdS)}$ is zero of the function $a^2_{{\rm erg}-s}(y)$. Its asymptotic behavior reads $a^2_{{\rm erg}-s}(y) \to \infty$ for $y \to 0^+$.

For $a^2 = a^2_{{\rm erg}-s}(y)$, these radii merge at the static radius [127]

$$r_s = y^{-1/3}, \tag{19}$$

as can be checked by inserting the function $a^2_{{\rm erg}-s}(y)$ into expression (17).

If $a^2 > a^2_{{\rm erg}-s}(y)$, or $y_{\rm crit(SdS)} < y$, the two roots are irrelevant, since they become to be complex. Furthermore, the static radius does not exist for spacetimes with $a^2 > a^2_{{\rm erg}-s}(y)$, as shown in [108]. We will not consider such spacetimes for the construction of the shadow, as they do not conform to the astrophysical constraints.

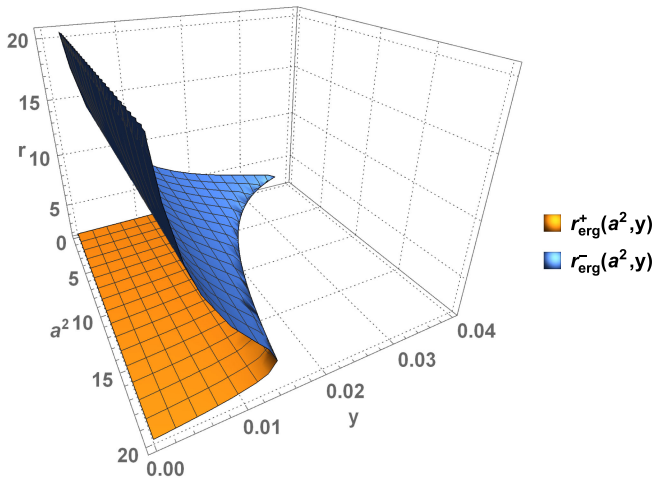

FIG. 3. Dependence of radii $r^{+}_{\mathrm{erg}}, r^{-}_{\mathrm{erg}}$ on the spacetime parameters a^2, y. The lower 3D-graph has constant value $r^{+}_{\mathrm{erg}} = 2$ for $y = 0$ independently of the spin a^2, while the upper 3D-graph tends to infinity. These graphs are connected by an edge whose projection into the $(a^2 - y)$-plane is the function $a^2_{\mathrm{erg}-s}(y)$, while the projection into the $(r - y)$-plane is the dependence of the static radius r_s on the cosmological constant $r_s = y^{-1/3}$.

In the region of positive radii, the ergosphere interferes with the equatorial plane at radii limited by the conditions

$$0 \le r \le r^{+}_{\mathrm{erg}} \quad \text{and} \quad r^{-}_{\mathrm{erg}} \le r < \infty$$
$$\text{for } a^2 < a^2_{\mathrm{erg}-s}(y) \quad \text{and} \quad 0 < y \le y_{\mathrm{crit(SdS)}}, \tag{20}$$

or

$$0 \le r < \infty \quad \text{for } a^2_{\mathrm{erg}-s}(y) \le a^2 \quad \text{or} \quad y_{\mathrm{crit(SdS)}} < y. \tag{21}$$

In the Kerr case ($y = 0$), Eq. (15) becomes linear and has the well-known solution $r = 2$, which is the limit for radius of the "inner" ergosurface $r = r^{+}_{\mathrm{erg}}$ as $y \to 0^{+}$, while the "outer" ergosurface $r = r^{-}_{\mathrm{erg}}$ does not exist, with $r^{-}_{\mathrm{erg}} \to \infty$ as $y \to 0^{+}$. the behavior of both radii as a function of the spacetime parameters a^2, y is illustrated in Fig. 3. Recall that in the BH spacetimes the region between the outer and inner horizons, where $g_{rr} < 0$, must be excluded, since the BH rotational energy (covariant) cannot be extracted from this region by classical processes. Considering the energy extraction from a BH we restrict the ergospheres to the regions above the outer horizon and below the cosmological horizon.

The function $a^2_{\mathrm{erg}-s}(y)$ has the inverse form

$$y_{\mathrm{erg}}(a^2) \equiv \frac{1}{a^2} + \frac{3\sqrt[3]{2}}{(a^{10} + \sqrt{4a^{18} + a^{20}})^{1/3}} - \frac{3(a^{10} + \sqrt{4a^{18} + a^{20}})^{1/3}}{\sqrt[3]{2}a^6}. \tag{22}$$

It has been shown in [110] that the inverse function $y_{\mathrm{erg}}(a^2)$ in the parameter plane $(y - a^2)$ determines the boundary between the KdS spacetimes where the radial photon motion exhibits the-so called divergent repulsive barrier (DRB), in the spacetimes where two separated ergoregions exist, one near the BH horizon and the other near the cosmological horizon, and the restricted repulsive barrier (RRB), in the BH spacetimes where only one ergoregion exists between the BH and cosmological horizons. Note that in the case of RRB (DRB) the photons incoming with high-axial angular momentum Φ [see Eq. (37)] from the vicinity of the cosmological horizon can (cannot) reach the surface $r = 0$. The notion of these concepts is illustrated in Sec. III C. The structure of the ergosphere is thus related to the character of the photon motion.

Outside the equatorial plane, the distribution of the points of the ergosurface can be described by the dependence of their latitudinal coordinate on the radial coordinate in the form

$$\theta_{\mathrm{erg}}(r) = \arcsin \sqrt{\frac{I - \sqrt{I^2 - 4y\Delta_r}}{2a^2 y}}. \tag{23}$$

The extension of the ergosphere is then given by the inequality $\theta_{\mathrm{erg}}(r) \le \theta \le \pi - \theta_{\mathrm{erg}}(r)$. From Eq. (23) it follows that for $a^2 \le 1/y$, the ergosurface is connected to the ring singularity, i.e., $\theta_{\mathrm{erg}}(0) = \pi/2$. However, for $a^2 > 1/y$, it is separated from the singularity and it intersects the disc $r = 0$ at the latitudinal coordinate

$$\theta_{\mathrm{erg}}(0) \equiv \theta_{\mathrm{erg}(0)} = \arcsin \sqrt{\frac{1}{a^2 y}}. \tag{24}$$

From Eq. (24) it can be seen that for $a^2 y \to \infty$, the ergosurface shrinks to infinitesimal extension in the neighborhood of the symmetry axis.

E. Division of the KdS spacetimes by relations of horizons and ergosurfaces

From the discussion of Eqs. (16), (17), (23), and (24) it follows that the functions $a^2_{\mathrm{erg}-s}(y)$ and $1/y$ play a crucial role in determining of the character of the ergosphere. The behavior of these functions, together with the functions $a^2_{\mathrm{min\,/\,max}(h)}(y)$, induces the partitioning of the KdS spacetimes according to the relations of horizons and ergosurfaces, shown in Fig. 4. In Fig. 5 we show the 3D representation of the distribution of the horizons, ergosurfaces and the static radius for some selected representative values of the spacetime parameters a^2, y, corresponding to individual cases of the spacetime division shown in Fig. 4, including the borderline cases. For convenience, we have used the so-called Kerr-Schild coordinates x, y, z (here the coordinate y should not be confused with the cosmological parameter), which appropriately represent the neighborhood

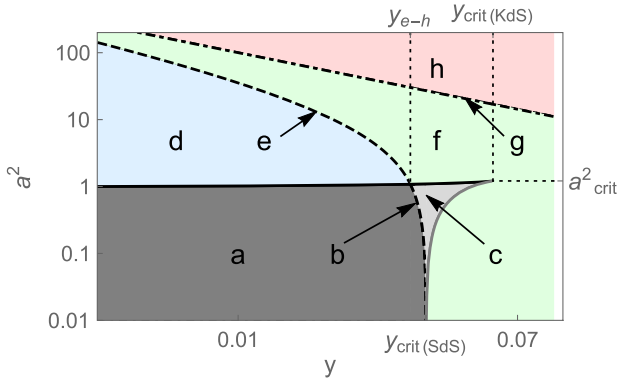

FIG. 4. Plot of the functions $a^2_{\text{max}(h)}(y)$ (black curve), $a^2_{\text{min}(h)}(y)$ (gray curve), $a^2_{\text{erg}-s}(y)$ (black dashed curve) and $1/y$ (black dash-dotted curve) and the induced separation of the KdS spacetimes according to the relations of horizons and ergosurfaces; critical values of the spacetime parameters are included. The functions $a^2_{\text{max}(h)}(y)$, $a^2_{\text{min}(h)}(y)$ represent the partitioning of the spacetimes into the BH and NS cases, as in Fig. 2. The function $a^2_{\text{erg}-s}(y)$ determines the partition into the spacetimes endowed with two separated ergoregions and the static radius (below the curve) and one ergoregion and no static radius (the rest of the parametric plane). The accompanying captions (a)–(h) refer to the individual cases shown in Fig. 5. The dark gray region corresponds to the BH spacetimes with two ergoregions and the static radius [see Fig. 5(a)]; the light gray region corresponds to the BH spacetimes with one ergoregion and no static radius [see Fig. 5(c)]; the blue region represents the NS spacetimes with two separated ergoregions and the static radius [see Fig. 5(d)]; the green region represents the NS spacetimes with one ergoregion and no static radius [see Fig. 5(f)]. The function $1/y$, represented as a straight line due to the logarithmic scale on both axes, separates the spacetimes with $a^2 > 1/y$ (the red region), whose ergosurface is separated from and surrounded by the ring singularity; the ergosphere then extends outside the ergosurface, which has the shape of a rotating ellipsoid, while the inner region, where $g_{tt} < 0$, is restricted to the vicinity of the spin axis [see Fig. 5(h)]. The boundary cases are shown in Figs. 5(b), 5(e), and 5(g). The spacetimes with $a^2 \lesseqgtr 1/y$ also differ in the character of the latitudinal photon motion (see [110]). As shown in the text below, the different character of the ergoregions is directly related to the properties of the photon motion, namely the spacetimes with two ergospheres are characterized by the divergent barrier DRB of the radial photon motion, while the spacetimes with one ergosphere are characterized by the repulsive barrier RRB of the radial photon motion (see Sec. III C for explanation). The displayed value y_{e-h}, which gives the intersection of the functions $a^2_{\text{erg}-s}(y)$, $a^2_{\text{max}(h)}(y)$, yields $y_{e-h} = 0.033185$, the corresponding value a^2_{e-h} (not shown) is $a^2_{e-h} = 1.0832$.

of the ring singularity, related to the Boyer-Lindquist coordinates r, θ by the relations

$$x^2 + y^2 = (r^2 + a^2)\sin^2\theta, \qquad z^2 = r^2\cos^2\theta. \tag{25}$$

The ergosphere of KdS BH spacetimes was discussed in [108], where the existence of the ergosphere was demonstrated also in the vicinity of the cosmological horizon. The Penrose process in both BH and cosmological ergoregions was also studied in [128].

We must emphasize that in the following the construction of the shadow is concentrated on the KdS NS spacetimes with the static radius and the DRB of the photon motion, since only this type of the NS spacetimes can be relevant from the point of view of the restrictions coming from astrophysical and cosmological observations [94].

In Sec. III F, we present a complete classification of the KdS spacetimes based on the properties of the horizons, ergosurfaces and the static radius, taking into account also the properties of the null geodesics. We use the results of the previous study presented in [110], focusing on the existence and properties of the spherical photon orbits (SPOs) governing the shadows of KdS BHs or KdS NSs.

F. LNRFs

The LNRFs were introduced (see [19]) as orthonormal reference frames related to accelerated observers orbiting at fixed coordinates r, θ, with zero angular momentum Φ; observers related to the LNRFs are also called zero-angular momentum observers (ZAMOs) [18,117]. Only these frames treat the $+\phi$ and $-\phi$ directions as equivalent with respect to the local geometry, i.e., they can be regarded as nonrotating with respect to the local geometry [15]. The world lines of these frames (observers) are perpendicular to the spacelike hypersurfaces $t = \text{const}$, as can be seen from the orthonormal tetrad of the basis vectors, whose angular velocity is given by the metric coefficients,

$$\Omega_{\text{LNRF}} = -\frac{g_{t\phi}}{g_{\phi\phi}} = \frac{a[\Delta_\theta(r^2 + a^2) - \Delta_r]}{A}, \tag{26}$$

where

$$A = (r^2 + a^2)^2\Delta_\theta - a^2\Delta_r \sin^2\theta. \tag{27}$$

It is easy to show that both these functions A and Ω_{LNRF} are positive at the stationary regions $\Delta_r > 0$ of the KdS spacetime at positive radii $r > 0$. However, in the case of negative radii, a small region near the ring singularity where $A < 0$ exists. This inequality defines the causality violation region where $g_{\phi\phi} < 0$; see Sec. III E.

The tetrad of the basis vectors reads

$$e_{(t)} = \sqrt{\frac{I^2 A}{\Delta_r \Delta_\theta \rho^2}}\left(\frac{\partial}{\partial t} + \Omega_{\text{LNRF}}\frac{\partial}{\partial\phi}\right), \tag{28}$$

$$e_{(r)} = \sqrt{\frac{\Delta_r}{\rho^2}}\frac{\partial}{\partial r}, \tag{29}$$

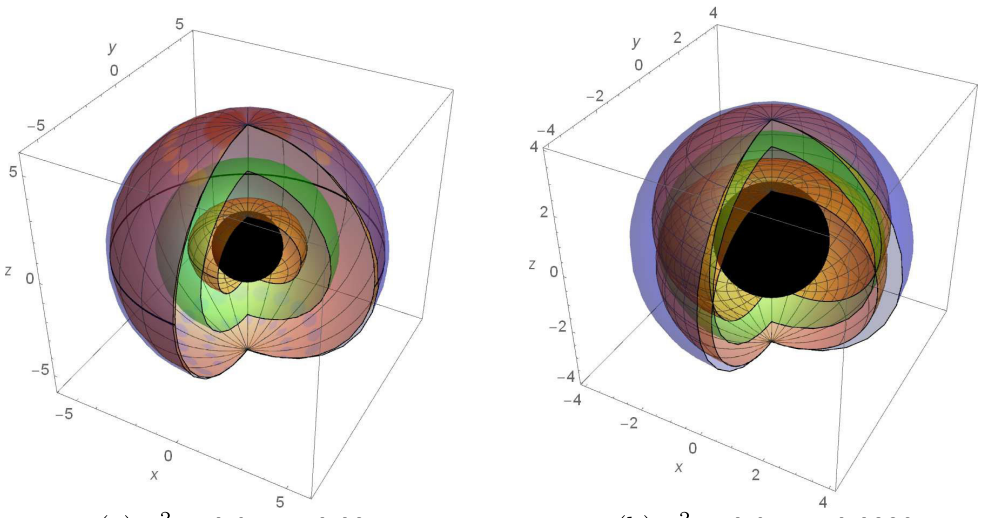

(a) $a^2 = 0.9, y = 0.02$ (b) $a^2 = 0.9, y = 0.0338$

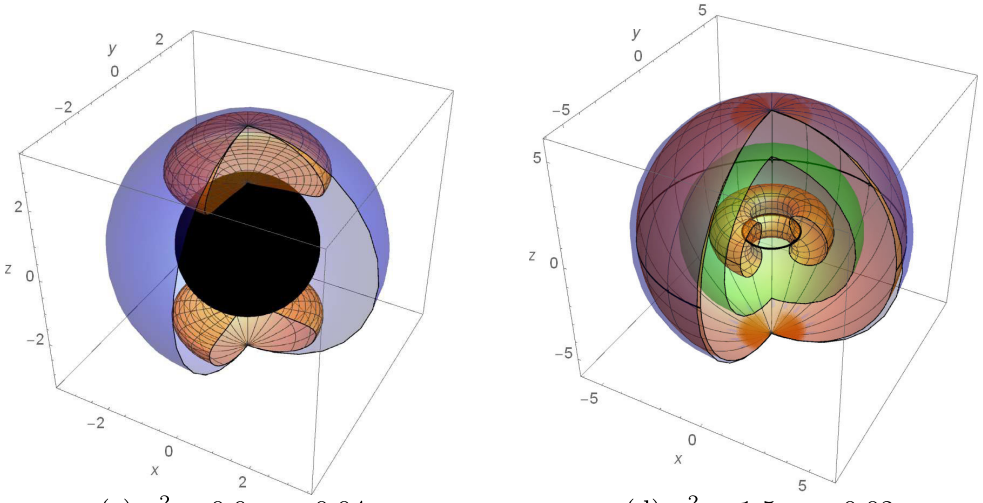

(c) $a^2 = 0.9, y = 0.04$ (d) $a^2 = 1.5, y = 0.02$

FIG. 5. Significant surfaces, i.e., horizons, ergosurfaces and static radius, if any, of the basic types of the KdS spacetimes, shown in the Kerr-Schild coordinates x, y, z in the region of positive radii (here the coordinate y should not be confused with the cosmological parameter y). The ergosurfaces are shown as orange lattice surfaces, the cosmological horizon as blue surface, the black spheres/rings represent the BH event horizon/ring singularity, the green spheres represent the static radius. The individual figures are plotted for the spacetime parameters representing the basic cases of the division of the KdS spacetimes shown in Fig. 4, so that the labels (a)–(h) in Figs. 4 and 5 correspond to each other: (a) represents the KdS BH spacetime with two separated ergospheres; the inner BH ergosphere and the outer cosmological ergosphere with the static radius and the DRB of the radial photon motion; (c) represents the KdS BH spacetime with the single ergosphere bounded between two closed ergosurfaces, one in each half-space, with no static radius and with the RRB of the radial photon motion; (d) describes the KdS NS spacetime with two separate ergospheres; the inner toroidal ergosphere connected to the ring singularity, and the cosmological ergosphere, with the static radius and the DRB of the photon motion; (f) describes the KdS NS spacetime with the only ergosphere extending outside the closed ergosurface, connected to the ring singularity, with DRB of the photon motion and no static radius; (h) represents the extreme case of the NS spacetime with the only ergosurface surrounded by the ring singularity; its latitudinal extension in the disc $r = 0$ is, according to Eq. (24), given by $\theta_0 = 45°$; (b)/(e) correspond to the boundary case between BH/NS spacetime with DRB/RRB, when the inner and outer ergosurfaces meet each other at the static radius; (g) shows the marginal case of NS spacetimes with ergosurfaces still connected to the ring singularity. In the BH cases we do not reflect the region below the event (outer) BH horizon; the spacetime structure is of the same character as in the Kerr BH spacetimes (see [61]). As far as naked singularities are concerned, we have to stress that only case (d) corresponds to the situations relevant from the point of view of astrophysics and cosmology implying that the parameter y must be very small. Note that the $r < 0$ region, not shown here, always contains the secondary cosmological horizon for both BH and NS spacetime, along with the ergosphere and ergoregion just between them.

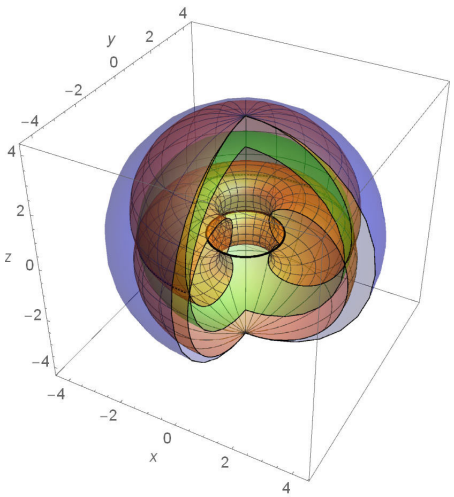

(e) $a^2 = 1.5, y = 0.0320$

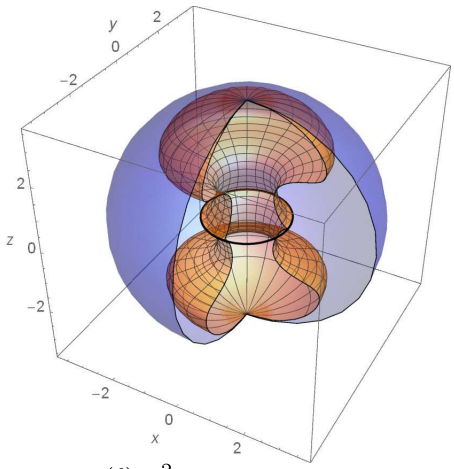

(f) $a^2 = 1.5, y = 0.04$

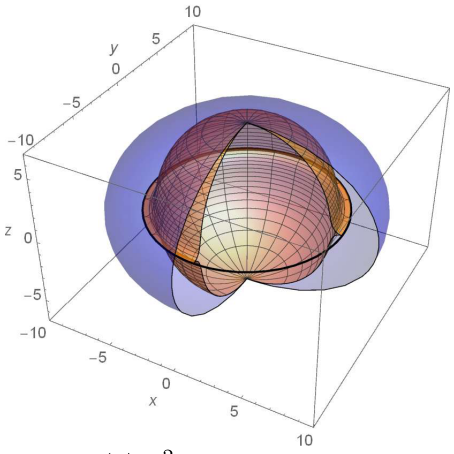

(g) $a^2 = 50, y = 0.02$

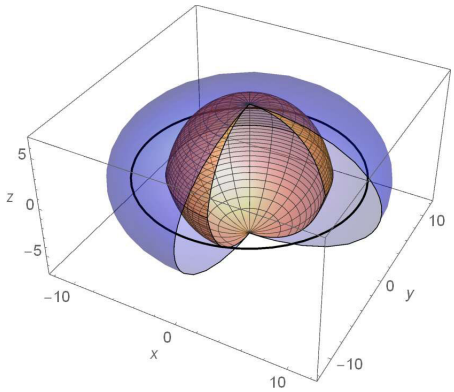

(h) $a^2 = 100, y = 0.02$

FIG. 5. (Continued).

$$e_{(\theta)} = \sqrt{\frac{\Delta_\theta}{\rho^2}}\frac{\partial}{\partial\theta}, \tag{30}$$

$$e_{(\phi)} = \sqrt{\frac{I^2\rho^2}{A\sin^2\theta}}\frac{\partial}{\partial\phi}. \tag{31}$$

The complementary tetrad of the differential 1-forms of the LNRFs is given by the relations

$$\omega^{(t)} = \sqrt{\frac{\Delta_r\Delta_\theta\rho^2}{I^2A}}\mathrm{d}t, \tag{32}$$

$$\omega^{(r)} = \sqrt{\frac{\rho^2}{\Delta_r}}\mathrm{d}r, \tag{33}$$

$$\omega^{(\theta)} = \sqrt{\frac{\rho^2}{\Delta_\theta}}\mathrm{d}\theta, \tag{34}$$

$$\omega^{(\phi)} = \sqrt{\frac{A\sin^2\theta}{I^2\rho^2}}(\mathrm{d}\phi - \Omega_{\mathrm{LNRF}}\mathrm{d}t). \tag{35}$$

The quantities characterizing a moving test particle as energy and components of angular momentum, measured locally in the LNRFs, are given by the projection of the particle 4-momentum p^μ onto the corresponding vectors of the orthonormal LNRF tetrad [18].

In the asymptotically flat Kerr spacetimes, the angular velocity of these frames $\Omega_{\mathrm{LNRF}} = \frac{d\phi}{dt}$ gives their angular velocity relative to infinity, i.e., relative to static observers located at infinity. At infinity, $\Omega_{\mathrm{LNRF}} = 0$; LNRFs correspond to the static (free or geodesic) reference frames at

infinity. In calculations of astrophysical phenomena in realistic situations, distant static frames (observers) are well approximated by the LNRFs, which are realistic approximations of the idealized static observers at infinity (see e.g. [54]).

The KdS geometry is not asymptotically flat, so the notion of the static free frames (observers) at infinity is not appropriate in such spacetimes. Therefore, we need to look for a suitable region of the KdS spacetimes that allows the existence of distant static frames that can be considered as free or nearly free, similarly to the static-free observers at infinity of the asymptotically flat Kerr spacetimes. It was shown in [107] that the region fulfilling this condition of being nearly flat is the static radius (and its vicinity), where test particles can be free in an unstable equilibrium [88,108]. The static radius exists in all the KdS NS spacetimes of astrophysical relevance that are included in class IVa considered here for the shadow construction.

We have chosen the parameters of the considered KdS spacetimes in such a way as to allow a clear and illustrative representation of the optical phenomena and properties of the NS shadow, but the values of the cosmological parameter y are much larger than those corresponding to astrophysically relevant spacetimes; for astrophysically relevant values of the parameter y we have to use logarithmic scales in demonstrating the effects on the magnitude of the shadow (see e.g. [93]).

G. Equations of geodesic motion

Due to the time and axial symmetry of the KdS spacetime, there are two Killing vector fields; the time Killing vector field $\xi_{(t)} = \partial/\partial t$ and the axial Killing vector field $\xi_{(\phi)} = \partial/\partial\phi$, such that projections

$$E = -\xi^{\mu}_{(t)} p_{\mu} = -p_t, \tag{36}$$

and

$$\Phi = \xi^{\nu}_{(\phi)} p_{\nu} = p_{\phi} \tag{37}$$

of the test particle coordinate 4-momentum p^{μ}, where

$$p^{\mu} = \frac{\mathrm{d}x^{\mu}}{\mathrm{d}\lambda}, \tag{38}$$

onto the Killing vectors are constants of motion along the geodesic (representing the covariant energy and the covariant axial angular momentum). Here λ is the affine parameter normalized so that

$$p^{\mu} p_{\mu} = -m^2, \tag{39}$$

where m is a trivial motion constant—the rest mass of the particle ($m = 0$ for photons). The energy and momentum components in a reference frame, related to local measurements in the considered frames, e.g. in the LNRFs, are given by the projections $p^{(t)} = -E_{\mathrm{LNRF}} = e^{\mu}_{(t)} p_{\mu}$, $p^{(\phi)} = \Phi_{\mathrm{LNRF}} = e^{\mu}_{(\phi)} p_{\mu}$, $p^{(r)} = e^{\mu}_{(r)} p_{\mu}$, $p^{(\theta)} = e^{\mu}_{(\theta)} p_{\mu}$. These quantities are not constants of the motion and depend on the position and velocity of the observer (frame). For definitions of the 3-vector of velocity with respect to reference frames see [19]. In the LNRFs particles with zero covariant-angular momentum, $\Phi = 0$, move perpendicular to the ϕ-direction, i.e., with $p^{\phi} = 0$.

Recall that in the KdS spacetimes, the covariant (conserved) quantities E, Φ cannot be interpreted as the energy and axial component of the angular momentum with respect to static observers at infinity, as in the Kerr spacetimes, since the KdS spacetimes are not asymptotically flat [88,89]; they are close to this interpretation for static observers near the static radius, if it exists, as shown in [107]. There is a nontrivial (fourth) motion constant, the so-called Carter constant $\mathcal{K}$, associated with the hidden symmetry of the KdS spacetime expressed by the Stachel-Killing tensor discussed in [61,129]. The geodesic motion of test particles in the KdS spacetimes is given by the Carter equations [61],

$$\rho^2 p^r = \pm\sqrt{R}, \tag{40}$$

$$\rho^2 p^{\theta} = \pm\sqrt{W}, \tag{41}$$

$$\rho^2 p^{\phi} = I\left(\frac{aP_r}{\Delta_r} - \frac{P_{\theta}\csc^2\theta}{\Delta_{\theta}}\right) \tag{42}$$

$$\rho^2 p^{t} = I\left[\frac{(r^2+a^2)P_r}{\Delta_r} - \frac{aP_{\theta}}{\Delta_{\theta}}\right], \tag{43}$$

where

$$R(r) = P_r^2 - \Delta_r(m^2 r^2 + \mathcal{K}), \tag{44}$$

$$W(\theta) = (\mathcal{K} - a^2 m^2 \cos^2\theta)\Delta_{\theta} - P_{\theta}^2 \csc^2\theta, \tag{45}$$

$$P_r = I[E(r^2+a^2) - a\Phi], \tag{46}$$

$$P_{\theta} = I(aE\sin^2\theta - \Phi). \tag{47}$$

III. MOTION OF PHOTONS

The motion of photons in the KdS spacetimes has been studied extensively in [110] for regions of positive radii $r > 0$. Here we extend this study and discuss the passage of a photon from the region of positive radii through the disc $r = 0, \theta \neq \pi/2$ to the region of negative radii $r \leq 0$, or its hit of the ring singularity at $r = 0, \theta = \pi/2$.

For the photon motion at positive radii $r > 0$, there are clear qualitative differences in the properties of the radial motion depending on the parameters a and y, and an

appropriate classification of the KdS spacetimes based on the character of the photon motion has been introduced [110]. In the present paper, we focus on the KdS NS spacetimes of the class IVa. This class corresponds to the KdS NS spacetimes with DRB, where there are two ergospheres and the static radius.

A. Constants of photon motion

Following previous works [97,110,130], for $E \neq 0$ we introduce the impact parameter

$$\ell \equiv \Phi/E, \tag{48}$$

and the associated motion constant

$$X \equiv \ell - a. \tag{49}$$

The fourth Carter's constant $\mathcal{K}$ must be non-negative [61]; $\mathcal{K} = 0$ for photons moving along the rotational axis of the spacetime $\theta = 0, \pi$, or for so-called principal null congruence (PNC) photons moving along the curves with $\theta = \text{const}$ [131]. However, $\mathcal{K}$ is usually replaced by the combination

$$Q \equiv \mathcal{K} - I^2(aE - \Phi)^2, \tag{50}$$

called the modified Carter's constant, which must be zero for the motion confined to the equatorial plane. For photon motion it is useful to consider the impact parameter related to the modified Carter constant

$$q \equiv Q/I^2E^2 = \mathcal{K}/I^2E^2 - X^2. \tag{51}$$

B. The coordinate and locally measured components of photon four-momentum

It is customary to denote the 4-momentum of a photon by $\mathbf{k}$ and its coordinate components by k^μ. Therefore, in the case of photons, Eqs. (38) and (39) become

$$k^\mu = \frac{\mathrm{d}x^\mu}{\mathrm{d}\lambda} \tag{52}$$

and

$$k^\mu k_\mu = 0, \tag{53}$$

respectively, where λ is an affine parameter. Due to the introduced motion constants X, q, Eqs. (40)–(43) then take the form,

$$\rho^2 k^r = \pm\sqrt{R}, \tag{54}$$

$$\rho^2 k^\theta = \pm\sqrt{W}, \tag{55}$$

$$\rho^2 k^\phi = I^2E\left[\frac{a(r^2 - aX)}{\Delta_r} + \frac{X + a\cos^2\theta}{\sin^2\theta\Delta_\theta}\right], \tag{56}$$

$$\rho^2 k^t = I^2E\left[\frac{(r^2 + a^2)(r^2 - aX)}{\Delta_r} + \frac{a(X + a\cos^2\theta)}{\Delta_\theta}\right], \tag{57}$$

where the functions R, W, governing the radial and latitudinal motion are of the form

$$R(r) \equiv I^2E^2[(r^2 - aX)^2 - \Delta_r(X^2 + q)], \tag{58}$$

$$W(\theta) \equiv I^2E^2\left[(X^2 + q)\Delta_\theta - \frac{(a\cos^2\theta + X)^2}{\sin^2\theta}\right]. \tag{59}$$

In a given reference frame, the locally measured 4-momentum components $k^{(a)}$ are given by the projections of the photon 4-momentum $\mathbf{k}$ onto the vectors of the tetrad—here considered as the LNRF tetrad introduced above—we arrive at the formula

$$k^{(a)} = \omega^{(a)}_\mu k^\mu. \tag{60}$$

We can also project the covariant coordinate components k_μ to the local tetrad of vectors by introducing

$$k_{(a)} = k_\mu e^\mu_{(a)}. \tag{61}$$

The orthonormality relations

$$e_{(a)}.e_{(b)} = \eta_{(a)(b)}, \tag{62}$$

where

$$\eta_{(a)(b)} = \mathbf{diag}\{-1, 1, 1, 1\} \tag{63}$$

is the Minkowski metric, and the duality relations

$$\omega^{(a)}[e_{(b)}] = \delta^{(a)}_{(b)} \tag{64}$$

then make sure that these quantities are related in a special relativistic way

$$k_{(a)} = \eta_{(a)(b)}k^{(b)}. \tag{65}$$

C. Motion constants of photons reaching the disc $r = 0$ and the region of negative radii $r < 0$

We determine the range of values of the motion constants q, X corresponding to photons coming from the region of positive radii $r > 0$ and either hitting the ring singularity at $r = 0$, or continuing into the region of negative radii. the motion of these photons in the region of $r < 0$ will be considered in the next section concentrating on the SPOs and the $\theta = \text{const}$. motion governing the shadow.

It is convenient to first determine the range of relevant values of the motion constant q.

1. Range of the parameter q

The reality condition of the radial motion at a given radius r_e

$$R(r_e; X, q) \geq 0 \tag{66}$$

implies that no photons with $q > 0$ can reach the ring singularity or the disc $r = 0$, nor enter the region of $r < 0$, as shown by the equality

$$R(r = 0; X, q) = -a^2 q. \tag{67}$$

The surface $r = 0$ can only be reached by photons in the so-called vortical type of the motion, with the motion constant $q \leq 0$ [88,131]; the upper limit $q = 0$ corresponds to the equatorial motion terminating at the ring singularity.

The reality condition of the radial motion expressed by the inequality (66) implies a restrictive condition on the values of the motion constant q, at a given radius r_e, in the form

$$q \leq q_{\max}(X; r_e), \tag{68}$$

where

$$q_{\max}(X; r) \equiv \frac{(r^2 - aX)^2}{\Delta_r} - X^2. \tag{69}$$

The constraint implied by the radial equation of motion thus gives the upper limit on the parameter q.

For a given value of the motion constant q, we can define an effective potential related to the motion constant X. The radial motion is governed by the effective potential (see [110,130])

$$X^r_{\pm}(r; q, y, a^2) \equiv \frac{ar^2 \pm \sqrt{\Delta_r [r^4 + q(a^2 - \Delta_r)]}}{a^2 - \Delta_r}; \tag{70}$$

the equality $X = X^r_{\pm}(r; q, y, a^2)$ determines the turning points of the radial motion. The functions $X^r_{\pm}(r; q, y, a^2)$, discussed in detail in [110], delimit the forbidden region in the $(r - X)$-plane, acting as a repulsive barrier (RB) of the radial photon motion, where the inequality (66) is not satisfied. This barrier can be either divergent (DRB) or restricted (RRB), independent of the spacetime parameters; the DRBs diverge at two radii $r > 0$, while the RRBs have no divergent points at $r > 0$, thus being restricted from above for values of the axial angular momentum parameter X [130,132]. A detailed discussion of the properties of the effective potential of the radial motion can be found in [110] and for KdS BHs also in [97]. Here, for illustration, we present in Fig. 6 typical cases of the behavior of $X^r_{\pm}(r; q, y, a^2)$, relevant for the motion near the disk $r = 0$. For completeness, both DRB and RRB cases are included—we can see that in both types of spacetimes the photons with $q = 0$ cannot enter the $r < 0$ region, while in the $q < 0$ case the $r < 0$ region is available for some family of photons, while it is unavailable for the other family.

The lower limit of the parameter q follows from the reality condition of the latitudinal motion at given latitudinal angle θ_e

$$W(\theta_e; X, q) \geq 0. \tag{71}$$

For a given latitudinal angle θ_e, the condition (71) can be rewritten in the form

$$q \geq q_{\min}(X; \theta_e), \tag{72}$$

where

$$q_{\min}(X; \theta_e) \equiv \frac{\cot^2 \theta_e}{\Delta_{\theta_e}} [(1 - a^2 y \sin^2 \theta_e) X^2 + 2aX + a^2 \cos^2 \theta_e]. \tag{73}$$

The condition that guarantees the possibility of the latitudinal motion for at least some angle $0 \leq \theta_e \leq \pi$ is then (see [110])

$$q \geq q^{\theta}_{\min}(X), \tag{74}$$

where $q^{\theta}_{\min}(X)$ is defined piecewise as

$$q^{\theta}_{\min}(X) \equiv \begin{cases} 0, & \text{for } X < X_{\max(q_2)} \text{ or } X > 0; \\ q_2(X; y, a), & \text{for } X_{\max(q_2)} \leq X < -a; \\ q_1(X), & \text{for } -a \leq X \leq 0; \end{cases} \tag{75}$$

and the auxiliary functions $q_1(X)$, $q_2(X; y, a)$ are defined by the relations

$$q_1(X) \equiv -X^2 \tag{76}$$

and

$$q_2(X; y, a) \equiv -\frac{[2a + X(1 - a^2 y)]^2}{I^2}. \tag{77}$$

The limit value

$$X_{\max(q_2)} = \frac{2a}{a^2 y - 1} \tag{78}$$

is the local maximum of the function $q_2(X; y, a)$.

The function $q^{\theta}_{\min}(X)$ has a global minimum $q = -a^2$ at $X = -a$, i.e., at the intersection of the functions $q_1(X)$,

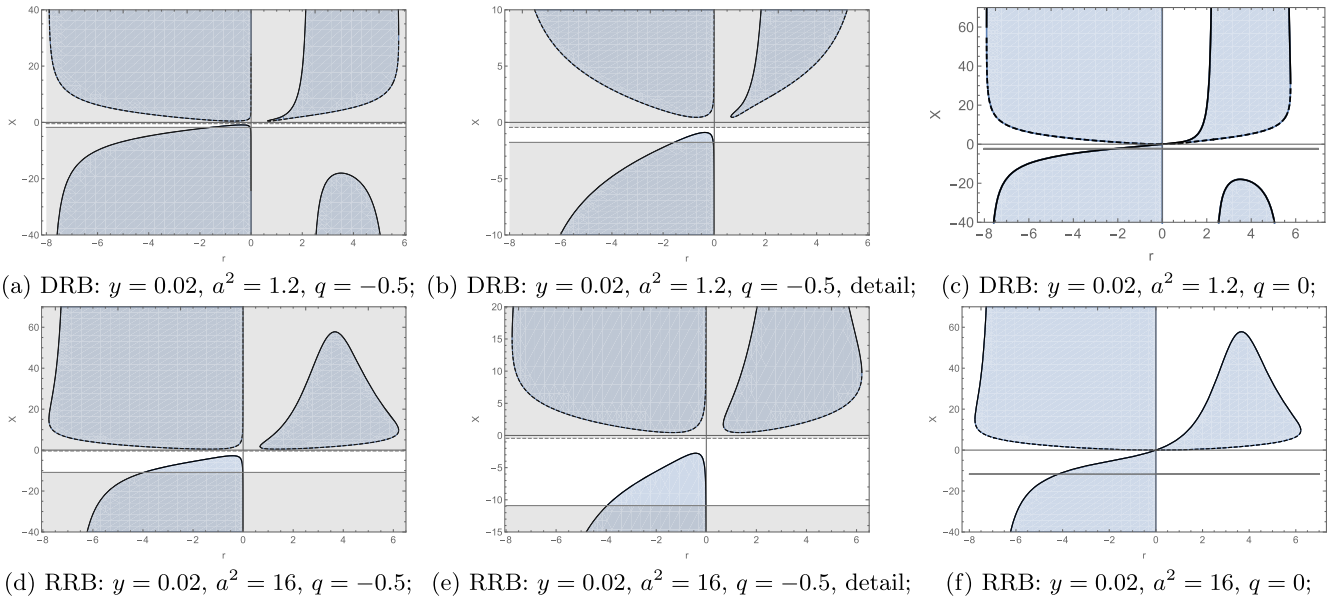

(a) DRB: $y = 0.02$, $a^2 = 1.2$, $q = -0.5$; (b) DRB: $y = 0.02$, $a^2 = 1.2$, $q = -0.5$, detail; (c) DRB: $y = 0.02$, $a^2 = 1.2$, $q = 0$;

(d) RRB: $y = 0.02$, $a^2 = 16$, $q = -0.5$; (e) RRB: $y = 0.02$, $a^2 = 16$, $q = -0.5$, detail; (f) RRB: $y = 0.02$, $a^2 = 16$, $q = 0$;

FIG. 6. Types of the effective barriers to the radial motion of photons that are relevant for entry into the $r < 0$ region. Upper row: the effective potentials $X_{+/-}(r)$ of the radial photon motion (full/dashed black curves) in the KdS NS spacetime with parameters $a^2 = 1.2$, $y = 0.02$ representing the spacetimes with divergent barrier of the radial photon motion (DRB); (a) for photons with motion constant $q = -0.5$; (b) the same in detail; (c) for photons with the motion constant $q = 0$. Bottom row: behavior of the effective potentials $X_{+/-}(r)$ in the KdS NS spacetime with parameters $a^2 = 16$, $y = 0.02$ representing the spacetimes with restricted barrier of the radial photon motion (RRB); (d) for photons with motion constant $q = -0.5$; (e) the same in detail; (f) for photons with the motion constant $q = 0$. In the case $q < 0$ (left and middle column), photon motion in both types of spacetimes is allowed for $X^{\theta}_{\rm min} \le X \le X^{\theta}_{\rm max}$ [see Eqs. (83)–(85)]. The allowed area is represented by a white band whose boundaries, indicated by a horizontal gray solid/gray dashed line, correspond to the values $X^{\theta}_{\rm min/max}$. In this case, for $r > 0$ no radial turning point exists, so the nature of the repulsive barrier is not significant, while for $r < 0$ it is, and some photons can continue to the area of negative radii while others are repelled by the repulsive barrier back into the positive radius region. In the case $q = 0$ (right column), photons with $X \le X_{\max(q2)}$ or $X \ge 0$ are confined to the equatorial plane (see Sec. III C 3). The value of $X_{\max(q2)}$ [see Eq. (78) below] is indicated by the horizontal gray line. They may terminate in the ring singularity or are repelled towards the cosmological horizon. Photons with $X_{\max(q2)} < X < 0$ travel from $r > 0$ through the interior of the disc $r = 0, \theta \neq \pi/2$ back to region of $r > 0$.

$q_2(X; y, a)$. It is therefore the lower limit of the allowed values of the parameter q. The relationship between the functions $q_1(X)$, $q_2(X; y, a)$, $q^{\theta}_{\rm min}(X)$ and $q_{\rm min}(X; \theta_e)$ is illustrated in Fig. 7.

We can conclude that the values of the parameter q, that allow photons to pass from the region of positive radii to the region of negative radii, cover the interval

$$-a^2 \le q \le 0. \tag{79}$$

The admissible values of the impact parameter X depend on the given motion constant q. In the following section we will show that there are qualitative differences between the cases $-a^2 \le q < 0$ and $q = 0$, so we will consider these cases separately.

2. The case $-a^2 \le q < 0$

As shown in [110], in the case of $q < 0$, the restrictions imposed on the latitudinal motion give stronger constraints on the value of the parameter X than the reality conditions of the radial motion (66) in the region of $r \ge 0$. The limits of the allowed values of the impact parameter X resulting from the condition (74) are given by the inequality

$$X^{\theta}_{+}(\theta; q, a^2, y) \le X \le X^{\theta}_{-}(\theta; q, a^2, y), \tag{80}$$

where the functions $X^{\theta}_{\pm}(\theta; q, a^2, y)$, defined as

$$X^{\theta}_{\pm}(\theta) \equiv \frac{a\cos\theta \pm \sin\theta\sqrt{\Delta_\theta}[a^2\cos^2\theta + q(1 + a^2 y \sin^2\theta)]}{\cos\theta(a^2 y \sin^2\theta - 1)}, \tag{81}$$

are the effective potentials governing the latitudinal motion. Note that the following relationship holds

$$X^{\theta}_{+}(\theta) = X^{\theta}_{-}(\pi - \theta), \tag{82}$$

and the inequality (80) holds for $0 \le \theta \le \pi/2$. For $\pi/2 \le \theta \le \pi$ the labels "+," "−" have to be interchanged.

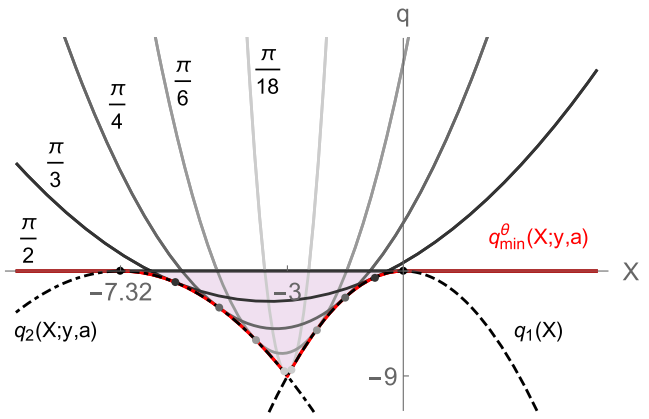

FIG. 7. The functions $q_1(X)$, $q_2(X;y,a)$, $q^{\theta}_{\min}(X)$ and $q_{\min}(X;\theta_e)$ given for the spacetime parameters $y=0.02$, $a^2=9$, representing the case $a^2y<1$. The function $q_{\min}(X;\theta_e)$ is shown in different shades of gray for different angles θ_e. Given θ_e, the latitudinal motion is allowed in the region $q \geq q_{\min}(X;\theta_e)$. The graph of $q_{\min}(X;\theta_e=\pi/2)$ is partially overlapped by the graph of the function $q^{\theta}_{\min}(X)$ shown in red. The range of parameters that allow negative radii is highlighted by a light red shading. The points of contact of the functions $q_{\min}(X;\theta_e)$ with the function $q_1(X)$ represent the motion constants of the PNC photons maintaining the initial coordinate $\theta_e=\theta_{\rm PNC}$; correspondingly, points of contact with the graph $q_2(X;y,a)$ correspond to another class of the θ^* photons, but with different properties than the PNC photons (cf. [131]).

The functions $X^{\theta}_{\pm}(\theta,q<0)$ meet at their common points at $\theta=0$, $\theta_{\rm com}\equiv \arcsin\sqrt{\frac{a^2+q}{a^2(1-qy)}}$, and $\pi-\theta_{\rm com}$, π, so that their graphs form closed curves, placed symmetrically with respect to $\theta=\pi/2$, whose interiors in the $(\theta-X)$-plane form the regions of allowed θ-motion. In the range $\theta_{\rm com}\leq\theta\leq\pi-\theta_{\rm com}$, the functions $X^{\theta}_{\pm}(\theta)$ are not defined. The functions $X^{\theta}_{\pm}(\theta,q=0)$ are not defined at $\theta=\pi/2$, but

$$\lim_{\theta\to\pi/2^+} X^{\theta}_{+}(\theta,q=0)=\lim_{\theta\to\pi/2^-} X^{\theta}_{-}(\theta,q=0)=0$$

and

$$\lim_{\theta\to\pi/2^-} X^{\theta}_{+}(\theta,q=0)=\lim_{\theta\to\pi/2^+} X^{\theta}_{-}(\theta,q=0)=X_{\max(q_2)},$$

(see Fig. 8).

The function $X^{\theta}_{+}(\theta,q<0)$ has a local minimum

$$X^{\theta}_{\min}(a^2,y,q)=\frac{I\sqrt{-q}-2a}{1-a^2y} \tag{83}$$

on the interval $0<\theta<\pi/2$, while the function $X^{\theta}_{-}(\theta,q<0)$ has a local maximum

$$X^{\theta}_{\max}(q)=-\sqrt{-q} \tag{84}$$

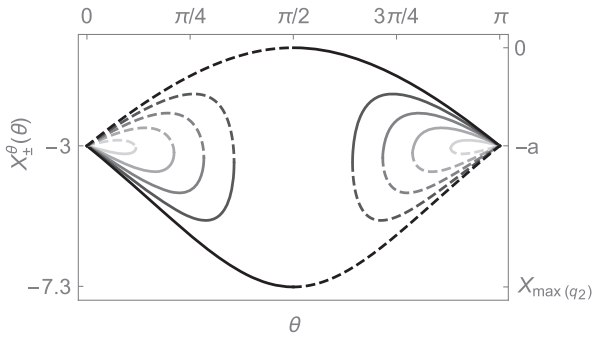

FIG. 8. The functions X^{θ}_{+} (full curves), X^{θ}_{-} (dashed curves) for spacetime parameters $y=0.02$, $a^2=9$ and for the motion constant q decreasing from $q=0$ (black) to $q=-8$ in steps of $\delta q=-2$, shown in decreasing shades of gray. The interior of the closed curves delimit the region that allows latitudinal motion.

on this interval. Of course, for $\pi/2\leq\theta\leq\pi$ the extrema (83) and (84) correspond to the local minimum and local maximum of the function X^{θ}_{-}, X^{θ}_{+}, respectively. The above statement about the constraints on the value of the parameter X means that the latitudinal motion is allowed for

$$X^{\theta}_{\min}\leq X\leq X^{\theta}_{\max} \tag{85}$$

in the case of $q<0$; in the limit $q\to 0^-$ this interval approaches the interval

$$X_{\max(q_2)}\leq X\leq 0, \tag{86}$$

or, in terms of the impact parameter ℓ,

$$\ell_{\max(q_2)}\equiv X_{\max(q_2)}+a\leq\ell\leq a. \tag{87}$$

In the Sec. III D 1 we will show that the local maxima $X^{\theta}_{\max}$ and the local minima $X^{\theta}_{\min}$ correspond to the impact parameters $X_{\rm PNC}$ and X^*, respectively, of photons of a special type that follow trajectories with constant latitude.

The case $q<0$ corresponds to the "vortical" motion (see, e.g., [88]), while for $r>0$ no radial turning point of the vortical motion exists. However, there may be a radial turning point at $r<0$ due to the radial potential barrier formed at $r<0$ (see Fig. 6). Typical orbits of this type are constructed in the $(r-\theta)$-plane by the numerical integration of the equation

$$s_r\int_{re}^{r}\frac{{\rm d}r}{\sqrt{R}}=s_\theta\int_{\theta_e}^{\theta}\frac{{\rm d}\theta}{\sqrt{W}} \tag{88}$$

with appropriately chosen integration limits and signs $s_{r,\theta}=\pm1$. The results are shown in Fig. 9.

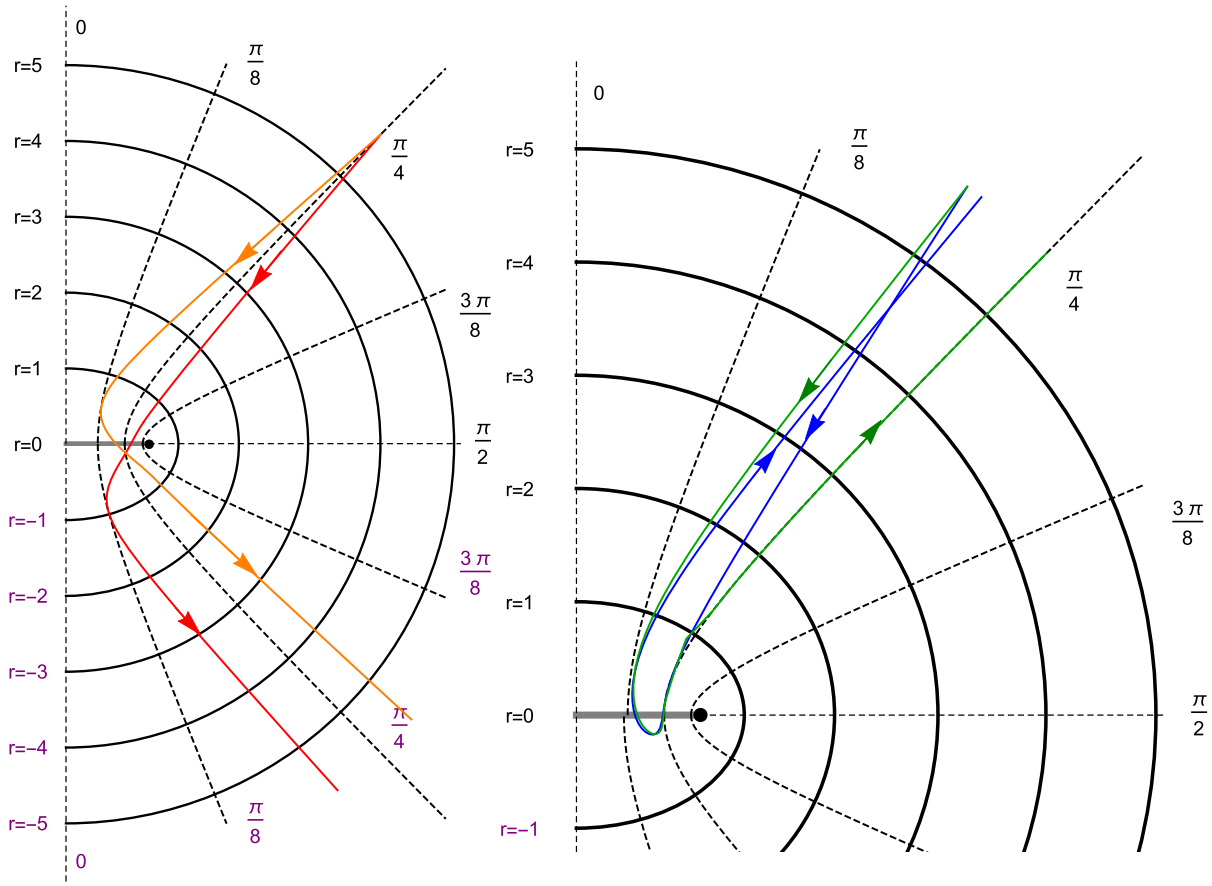

FIG. 9. Photon trajectories entering the $r < 0$ region, shown in the $(r-\theta)$-plane. The trajectories are obtained by integrating Eq. (88) in the KdS NS spacetime with parameters $a^2 = 1.2$, $y = 0.02$. Black semiellipses indicate surfaces of constant Boyer-Lindquist radius, black dashed hyperbolic curves indicate surfaces of constant latitudinal coordinate. The photons start their motion near the cosmological horizon at $r_c = 5.77$ with motion constants $q < 0$ and $X_{\max(q_2)} < X < 0$ allowing the entry of the $r < 0$ sheet. The coordinate surfaces in the $r > 0/r < 0$ sheet are labeled in black/purple. Note that the upper half of the figures shows the "northern" half-space of the $r > 0$ -sheet and the lower half of the figures shows the "northern" half-space of the $r < 0$ sheet, as follows from the construction of the connection of both sheets according to [112]. Red/orange color (left figure) corresponds to the locally prograde photons emitted at $\theta_e = \pi/4$ with motion constant $X = -0.74 > -a$, $q = -0.3$, giving trajectories with the latitudinal turning points θ_N, θ_S at $\theta_N = \pi/8, \theta_S \approx 1$ and allowing the continuation of the trajectories in the northern half-space of the $r < 0$ region, without radial turning point, to $r \to r_c^-$, initially oriented in positive/negative latitudinal direction. the blue/green color (right figure) describes the locally retrograde photons starting at $\theta_e = \pi/5$, $X = -1.44 < -a$, $q = -0.5$ with the latitudinal turning point $\theta_N \approx \pi/7, \theta_S = \pi/4$ and the radial turning point at $r = -0.2$ in the northern half-space of the $r < 0$ region, which return back to the "northern" half-space of the $r > 0$ region, initially oriented in positive/negative latitudinal direction. The azimuthal motion is suppressed, so the full 3D orbits can spiral many times around the spin axis.

3. The case $q = 0$

For $q = 0$ and

$$X \le X_{\max(q_2)} \quad \text{or} \quad X \ge 0 \tag{89}$$

only the equality $W = 0$ in the condition (71) is fulfilled for the emission angle $\theta_e = \pi/2$, thus the motion is restricted to the equatorial plane. However, there is now an additional restriction of the intervals in (89) induced by the reality condition of the radial motion (66) and the associated effective potential $X^r_{\pm}(r; q, y, a^2)$.

In Fig. 6 we show that for $q = 0$ some kind of the RB is formed at $r > 0$ for incoming photons from large radii and an infinitely high barrier exists at $r = 0$. Therefore, these photons cannot enter the region of $r < 0$ and either terminate at the ring singularity at $r = 0$, $\theta = \pi/2$, or are repelled backwards by the repulsive barrier at the radius $r = 0$.

For $X_{\max(q_2)} < X < 0$ and the emission angle $\theta_e \neq \pi/2$, $W > 0$ holds and the photon has a latitudinal turning points between latitudes given by the inequality (80). However, for $\theta = \pi/2$ it is now $\mathrm{d}\theta/\mathrm{d}\lambda = 0$ and $\mathrm{d}^2\theta/\mathrm{d}\lambda^2 = 0$, hence the possible achievement of $\theta = \pi/2$ means stopping in the

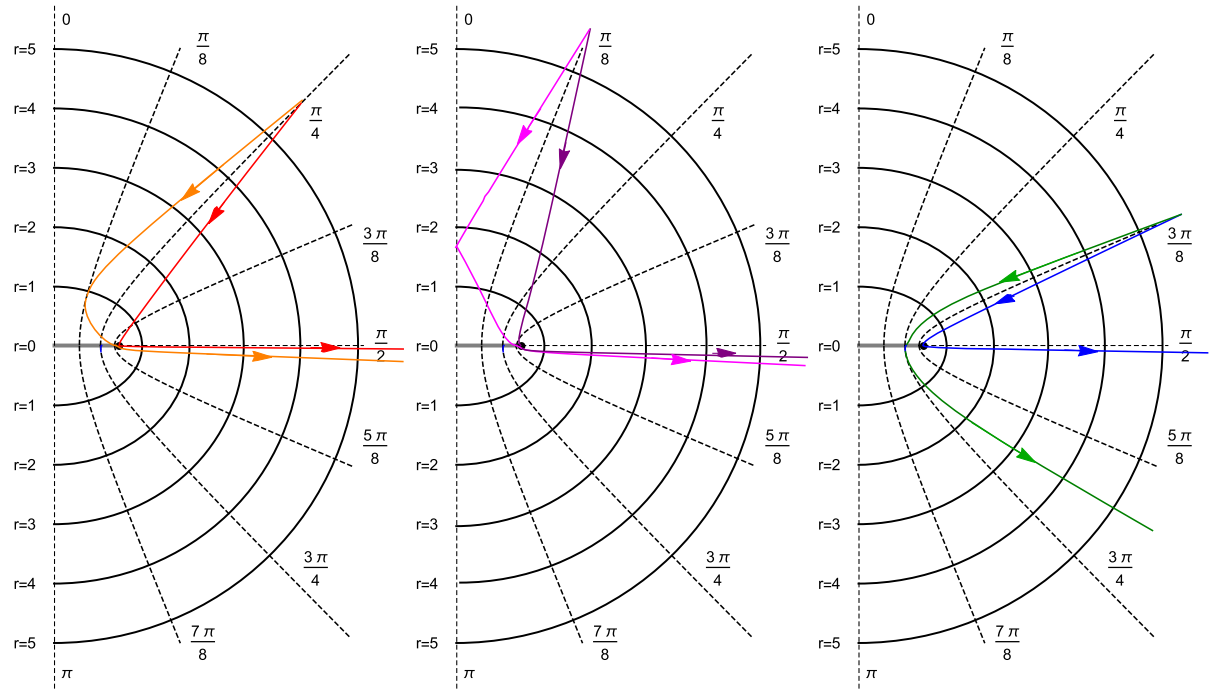

FIG. 10. Photon trajectories crossing the surface $r = 0$ from the "northern" to the "southern" half-space of the $r > 0$ region, shown in the $(r - \theta)$-plane. The trajectories are obtained by integrating Eq. (88) in the KdS NS spacetime with parameters $a^2 = 1.2$, $y = 0.02$ for photons arriving from the vicinity of the cosmological horizon at $r_c = 5.77$ with motion constants $q = 0$ and $X_{\max(q_2)} < X < 0$, which do not allow continuation to the $r < 0$ region, since a radial turning point occurs at $r = 0$ according to the behavior of the effective potentials [see Figs. 6(c) and 6(f)]. This is interpreted as a transit through the $r = 0$ surface and continuation to larger radii in the "southern" half-space of the $r > 0$ sheet. Red/orange curve (left figure) describes trajectory with no/one latitudinal turning point, corresponding to photons initially directed in a positive/negative latitudinal direction; both curves correspond to the locally prograde photons with motion constant $X = -0.67 > -a$, giving the latitudinal turning point $\theta_t = \pi/8$ (orange curve). Purple/magenta curve (middle figure) describes trajectory with no/one latitudinal turning point, corresponding to photons initially directed in a positive/negative latitudinal direction; both curves correspond to a photon with $X = -1.10 = -a$, i.e., with zero covariant angular momentum ℓ, and thus with zero locally measured motion in the azimuthal direction [see Eq. (134)]; the magenta curve shows the trajectory crossing the spin axis. Blue/green color (right figure) describes trajectory with no/one latitudinal turning point, corresponding to photons initially directed in a positive/negative latitudinal direction; both curves correspond to the locally retrograde photons with $X = -1.90 < -a$; the green curve shows a trajectory with latitudinal turning point $\theta_t = \pi/4$. The trajectories without latitudinal turning point approach the final latitude $\theta_f \sim \pi/2$ in the "southern" half-space. The azimuthal motion is suppressed, so the real trajectories may spiral many times around the spin axis.

equatorial plane. If $\theta_e = \pi/2$ at the beginning of the motion, the motion is unstably confined to the equatorial plane and terminates at the ring singularity. For $\theta_e \neq \pi/2$ the photons travel from $r > 0$ through the interior of the disc $r = 0$, $\theta \neq \pi/2$ back to $r > 0$.

In Fig. 10 we show typical trajectories of photons with $q = 0$ and $X_{\max(q_2)} < X < 0$ obtained by direct integration of Eq. (88). It is shown that none of these photons terminate at the ring singularity, regardless of whether they are locally prograde with respect to the LNRF $(k^{(\phi)}/k^{(t)} > 0)$, with $X > -a$, or retrograde $[k^{(\phi)}/k^{(t)} < 0]$, with $X < -a$ (for clarification of the terms "prograde/retrograde," see Sec. III E), and independent of the initial direction of the latitudinal motion. It is shown that the trajectories asymptotically approach the equatorial plane after passing through the disc $r = 0$.

D. Some important cases of photon trajectories

We now discuss cases of the null geodesics of the KdS NS spacetimes, which play a crucial role in the treatment of the shadow (silhouette) of the NS spacetimes, taking into account the region of negative radii; namely, we study the photons following trajectories with constant latitudinal coordinate or constant radial coordinate.

1. Trajectories of constant latitude

The motion constants X, q corresponding to the local maxima $X^{\theta}_{\max}$ of the functions $X^{\theta}_{+/-}(\theta)$ [see Eq. (84)] satisfy the equality

$$q = q_1(X), \tag{90}$$

and they belong to the special class of the PNC geodesics of the KdS geometry, privileged by the geometry [15]. The PNC photon 4-vectors appear in the Kerr-Schild coordinates as "generators" of the Kerr(dS) metric [112]—the KdS spacetime can be expressed as de Sitter-plus-squared-null form related to these photons [61], while the Kerr spacetime can be expressed as Minkowski-plus-squared-null form [15]. Photons moving along the PNC geodesics maintain a constant latitude $\theta = \theta_{\rm PNC}$. This can be verified by inserting the equality in (76) into (59), which implies that the reality condition for the latitudinal motion reduces to $W(\theta) = 0$, which can only be true for

$$\theta_{\rm PNC} = \arccos\sqrt{-\frac{X}{a}} = \text{constant}. \tag{91}$$

The motion constants are then

$$X_{\rm PNC} = -a\cos^2\theta_{\rm PNC}, \tag{92}$$

or equivalently [88,131],

$$\ell_{\rm PNC} = a\sin^2\theta_{\rm PNC} \tag{93}$$

and

$$q_{\rm PNC} = -a^2\cos^4\theta_{\rm PNC}. \tag{94}$$

According to the relations (92) and (94), the following inequalities have to be satisfied:

$$-a \le X_{\rm PNC} \le 0, \tag{95}$$

or equivalently,

$$0 \le \ell_{\rm PNC} \le a \tag{96}$$

and

$$-a^2 \le q_{\rm PNC} \le 0, \tag{97}$$

where the lower limits apply to photon emission on the spin axis and the upper limits to emission on the equatorial plane. According to the relation (96) [see Eq. (134)] the PNC photons are locally corotating with respect to the LNRF. Of course, the azimuthal coordinate component of the PNC photon 4-momentum is also in the positive ϕ direction in the stationary region $\Delta_r > 0$, as can be seen from the azimuthal Eq. (56), which now has the form

$$\frac{{\rm d}\phi}{{\rm d}\lambda} = \frac{aI^2E}{\Delta_r}. \tag{98}$$

The "radial" equation (58) for the PNC photons with motion constants given by Eqs. (92)–(94) reduces to

$$\frac{{\rm d}r}{{\rm d}\lambda} = \pm IE, \tag{99}$$

where the $+/-$ sign corresponds to the outgoing/ingoing photons with $E > 0$. From Eq. (99) it follows that there are no turning points in the radial direction for the PNC photons with $E \neq 0$, i.e., if they are initially directed inwards, they either reach $r = -\infty$ for $\theta_{\rm PNC} \neq \pi/2$, or hit the ring singularity for $\theta_{\rm PNC} = \pi/2$.

It follows from the discussion above that of particular interest is the PNC photon at $\theta_{\rm PNC} = \pi/2$, with $q_{\rm PNC} = 0$, $X_{\rm PNC} = 0$, which is the marginal photon confined in the equatorial plane that still hits the ring singularity. It also corresponds to the edge of the ring singularity silhouette as seen in the equatorial plane (cf. [133]).

Another class of the null geodesics of constant latitude, which we denote $\theta = \theta^*$ for short, has the motion constant given by

$$q = q_2(X; y, a) \tag{100}$$

corresponding to the local minima $X^\theta_{\rm min}$ of the functions $X^\theta_{+/-}(\theta)$ [see Eq. (83)]. The associated motion constants together

$$X^* = a\frac{\cos^2\theta^*(1-a^2y)-2}{\Delta_{2\theta^*}}, \tag{101}$$

or equivalently,

$$\ell^* = \frac{-aI\sin^2\theta^*}{\Delta_{2\theta^*}}, \tag{102}$$

and

$$q^* = -\frac{a^2I^2\cos^4\theta^*}{\Delta^2_{2\theta^*}}, \tag{103}$$

where we define

$$\Delta_{2\theta^*} \equiv 1 + a^2y\cos 2\theta^* > 0. \tag{104}$$

From Eq. (102) it follows that $\ell^* \le 0$, i.e., such photons are oriented in negative ϕ-direction with respect to the LNRF. A comparison of Eqs. (93), (94) and (102), (103) indicates that in the pure Kerr case $y = 0$, $\ell_{\rm PNC} = -\ell^*$, $q_{\rm PNC} = q^*$ (see [131]).

Inspecting the radial motion of photons with motion constants given by Eqs. (101)–(103), we find the radial function in Eq. (54) in the form

$$R(r;X^*,q^*) \equiv R^*(r;\theta^*) = \frac{I^2r^4 + 2I^2a^2\cos^2\theta^* r^2 + 8a^2\sin^2\theta^*\Delta_{\theta^*} r + I^2a^4\cos^4\theta^*}{\Delta^2_{2\theta^*}}, \tag{105}$$

which means that for this class of null geodesics there are no turning points of the radial motion at positive radii $r > 0$, but a turning point can exist at negative radii $r \leq 0$ for a sufficiently large latitude θ^*.

Obviously, the $\theta^* = \pi/2$ photons must hit the ring singularity, so for the incoming photons a "turning" point at $r = 0$ exists, as confirmed by the equality

$$R^*(r;\theta^* = \pi/2) = \frac{I^2r^4 + 8a^2r}{(1-a^2y)^2}. \tag{106}$$

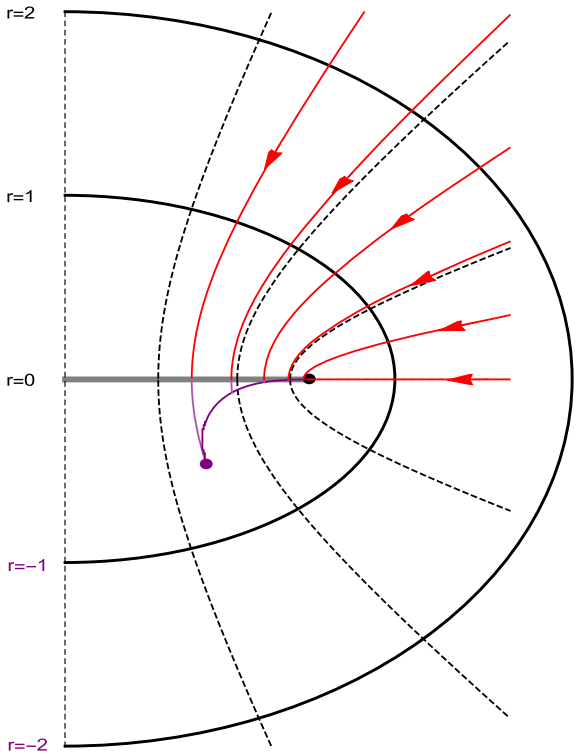

FIG. 11. The null geodesics of constant latitude θ^* in the KdS NS spacetime with $a^2 = 1.2$, $y = 0.02$, with radial turning points at negative radii. The phases in the region $r > 0$ are shown in red, those in the region $r < 0$ in light purple. The radial turning points $r^* < 0$ lie on the purple curve, the purple point represents the deepest "turning point" at $r^*_{\rm SPO} = -0.54$ of a photon with $\theta^*_{\rm min} = 31.3°$, which is actually an unstable circular photon orbit lying in a plane parallel with the equatorial plane with the symmetry axis aligned with the spin axis. As shown below, this radius corresponds to the lowest SPO of given spacetime. For θ^* growing to $\theta^* = \pi/2$, the radial turning points approach the value $r = 0$, i.e. the $(\theta^* = \pi/2)$ photons hit the ring singularity.

On the other hand, there is a free path to $r \to -\infty$, at least for photons moving along the spin axis since

$$R^*(r;\theta^* = 0) = (r^2 + a^2)^2 > 0. \tag{107}$$

The radial equation then has the form of Eq. (99) which is valid for the PNC photons. It can be shown that for any pair (a^2, y) there exists indeed an angle $\theta^*_{\rm min}$, $0 < \theta^*_{\rm min} < \pi/2$, such that for $\theta^* \geq \theta^*_{\rm min}$ a radial turning point $r^* < 0$ exists for the incoming θ^* photons (see Fig. 11).

The radial turning points descent from $r^* = 0$ for $\theta^* = \pi/2$ to the lowest value $r^* = r^*_{\rm SPO} < 0$ for $\theta^* = \theta^*_{\rm min}$, which is in fact an unstable off-equatorial circular photon orbit (see Fig. 11), which is, as shown in Sec. III E, locally counter-rotating. As we will show in the next section, the radius $r^*_{\rm SPO}$ corresponds to the lowest ever spherical photon orbit, which represents the lower limit of the SPO region at negative radii of given spacetime [see Figs. 15(a), 18(f), and 20]. The dependence of both quantities, $\theta^*_{\rm min}$, $r^*_{\rm SPO}$, on the spacetime parameters a^2, y is shown in Figs. 12 and 13.

According to Eqs. (101)–(103), for $a^2y < 1$ the motion constants of the θ^* photons are restricted by the relations

$$X_{\max(q_2)} \leq X^* \leq -a, \tag{108}$$

where the lower (upper) limit corresponds to $\theta^* = \pi/2$ $(\theta^* = 0)$ and

$$-a^2 \leq q^* \leq 0, \tag{109}$$

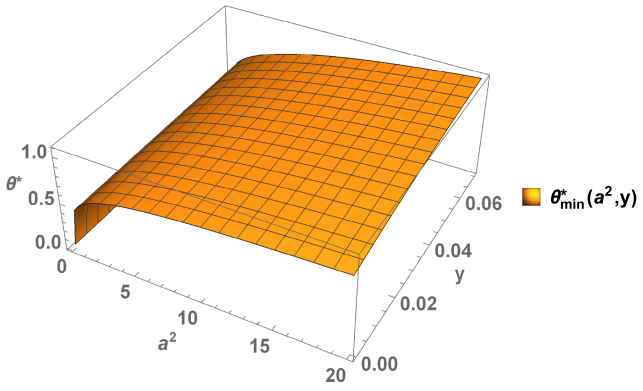

FIG. 12. The dependence of the latitude $\theta^*_{\rm min}$, to which the lowest SPO of a given spacetime with radius $r^*_{\rm SPO} < 0$, i.e., the unstable retrograde circular photon orbit, is confined, on the cosmological parameters a^2, y.

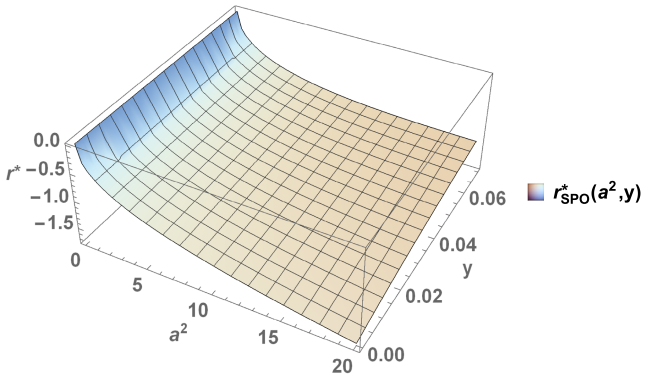

FIG. 13. Dependence of the off-equatorial circular photon orbits with negative radii $r^*_{\rm SPO}$ on which the $\theta^*_{\rm min}$-photons are wound on the spacetime parameters a^2, y. These are the radii of the lowest SPOs of a given spacetime that enclose the region of the SPOs from below.

where, as in Eq. (97), the lower limit applies to the photon emission on the spin axis, the upper to emission in the equatorial plane.

The pair $X^* = X_{\max(q_2)}, q^* = 0$ corresponds to the local maximum of the function $q_2(X; y, a)$. Photons with motion constants approaching these values, i.e., with $\theta^* \to \pi/2$, have a turning point at $r < 0$ close to the ring singularity. Thus, the θ^* photons, similarly to the PNC photons, delimit the angular size of the escape light cone coming through the ring singularity [see Fig. 29(a)] as $\theta_e \approx \pi/2$. Of course, when constructing the shadows, they also delineate the silhouette of the ring singularity as the observer's inclination approaches the equatorial plane.

2. Spherical photon orbits

The SPOs are determined by the conditions

$$R(r) = 0, \qquad \frac{{\rm d}R}{{\rm d}r} = 0, \tag{110}$$

whose simultaneous solution gives the motion constants for the photons on the SPOs

$$X = X_{\rm SPO}(r) \equiv \frac{r[(1-ya^2)r^2 - 3r + 2a^2]}{a[2yr^3 + (ya^2-1)r + 1]}, \tag{111}$$

or alternatively,

$$\ell = \ell_{\rm SPO}(r) \equiv \frac{Ir^3 - 3r^2 + a^2 Ir + a^2}{a[2yr^3 + (ya^2-1)r + 1]}, \tag{112}$$

and

$$q = q_{\rm SPO}(r) \equiv -\frac{r^3 y^2 a^4 r^3 + 2ya^2 r^2 (r+3) + r(r-3)^2 - 4a^2}{a^2 [2yr^3 + (ya^2-1)r + 1]^2}. \tag{113}$$

The functions $X_{\rm SPO}(r)$, $\ell_{\rm SPO}(r)$, $q_{\rm SPO}(r)$ have common divergence points at radii $r^{(-)}_{d({\rm SPO})}$, $r^{\pm}_{d({\rm SPO})}$ for $a^2 y < 1$, where

$$r^{(-)}_{d({\rm SPO})} = -2\sqrt{\frac{1-a^2 y}{6y}} \cos\left[\frac{1}{3}\arccos\sqrt{\frac{27y}{2(1-a^2y)^3}}\right], \tag{114}$$

and

$$r^{\pm}_{d({\rm SPO})} = 2\sqrt{\frac{1-a^2 y}{6y}} \cos\left[\frac{\pi}{3} \pm \frac{1}{3}\arccos\sqrt{\frac{27y}{2(1-a^2y)^3}}\right], \tag{115}$$

which satisfies the relation $r^{(-)}_{d({\rm SPO})} < 0 < r^{+}_{d({\rm SPO})} < r^{-}_{d({\rm SPO})}$.

The positive radii are related to the marginal spherical photon orbits. They coalesce for $a^2 = a^2_{d({\rm SPO})}(y)$, where

$$a^2_{d({\rm SPO})}(y) \equiv \frac{1}{y} - \frac{3\sqrt[3]{4}}{2\sqrt[3]{y^2}}. \tag{116}$$

Note that the function $a^2_{d({\rm SPO})}(y)$ in the $(a^2 - y)$ plane determines the boundary between the KdS spacetime classes VI and VII, as introduced in [110]. For $a^2 \lesseqgtr a^2_{d({\rm SPO})}(y)$, the functions $X_{\rm SPO}(r)$, $q_{\rm SPO}(r)$ have two/no divergence points. Their typical behavior is shown in Fig. 14.

For the SPOs at negative radii, the point $r^{(-)}_{d({\rm SPO})} < 0$ is relevant. It can be verified that for $r \to r^{(-)}_{d({\rm SPO})}$ from the right, $q_{\rm SPO}(r) \to -\infty$ holds (see Fig. 14). Since $-a^2 \le q \le 0$ necessarily holds, it follows that the range of the SPOs with negative radii is restricted to the interval $r^{(-)}_{d({\rm SPO})} < r_{\rm SPO} < 0$. More precisely, the radius of the lowest SPO is given by the equality

$$q_{\rm SPO}(r) = q^{\theta}_{\rm min}(X_{\rm SPO}(r)), \tag{117}$$

which is represented in Fig. 15 as the intersection of the curve $q_{\rm SPO}(X_{\rm SPO})$, parametrized by the radii $r_{\rm SPO}$ of the unstable spherical photon orbits $[(X_{\rm SPO}(r_{\rm SPO}), q_{\rm SPO}(r_{\rm SPO})]$, with the curve $q^{\theta}_{\rm min}(X)$. As follows from the comment to Fig. 7, this intersection corresponds to the θ^* photon. Since it is the lowest orbit, according to the notation introduced in the previous subsection, it corresponds to the designation $r^*_{\rm SPO}$, to which the $\theta^*_{\rm min}$ photons are wound (see Fig. 11). Due to the vortical character of the motion of photons with $q < 0$, the SPOs at negative radii have a different shape than

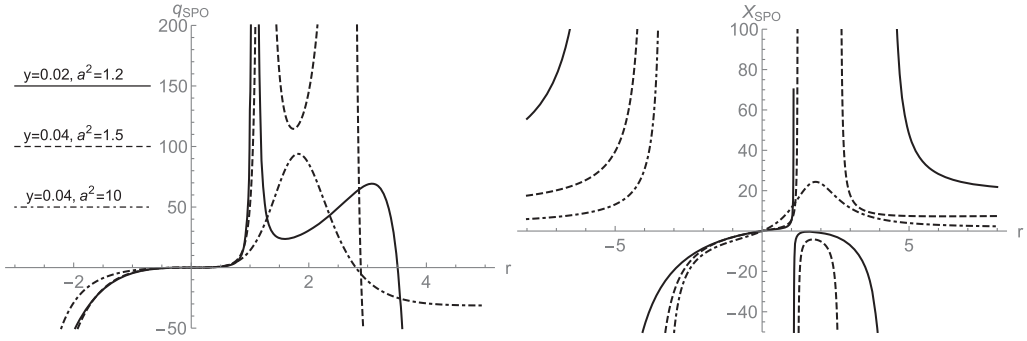

FIG. 14. Illustration of the effective potentials governing the photon motion. Typical behavior of the functions $X_{\rm SPO}(r)$, $q_{\rm SPO}(r)$ is shown. The solid lines correspond to the KdS NS spacetimes of the classes IV, V, as introduced in [110], characterized by the DRB of the radial photon motion and two divergences of $X_{\rm SPO}(r)$, $q_{\rm SPO}(r)$; the dashed lines correspond to the class VI with the RRB and two divergences of $X_{\rm SPO}(r)$, $q_{\rm SPO}(r)$, and the dot-dashed lines correspond to the classes VII, VIII with RRB and no divergences of $X_{\rm SPO}(r)$, $q_{\rm SPO}(r)$. Note the qualitatively unchanged behavior of both functions $X_{\rm SPO}(r)$, $q_{\rm SPO}(r)$ for $r^{(-)}_{d({\rm SPO})} < r \le 0$. Since $-a^2 \le q \le 0$, the range of the spherical orbits at negative radii $r_{\rm SPO}$ must be $r^{(-)}_{d({\rm SPO})} < r^{*}_{\rm SPO} < r_{\rm SPO} < 0$. The asymptotic behavior $X_{\rm SPO} \to +\infty$ at $r < r^{(-)}_{d({\rm SPO})}$ is therefore irrelevant.

at $r > 0$ (cf. [134,135]). The lowest SPOs at $r = r^{*}_{\rm SPO}$ are the special case of SPOs reduced to off-equatorial circular photon orbits, which are unstable and counterrotating (see Sec. III E).

Formally we can get the solution $r_{\rm SPO} = 0$, which however corresponds to the physical singularity and therefore cannot be regarded as an orbit.

Another solution of the system of equations (110) is

$$X = \frac{r^2}{a}, \tag{118}$$

and

$$q = -\frac{r^4}{a^2}. \tag{119}$$

The relations (118) and (119) represent a parametric determination of the descending part of the function $q_1(X)$ defined in the relation (76), where r is the parameter. However, this part is in the region that negates the inequalities (74) and (75) which reflects the reality of the latitudinal motion (see Fig. 7), and should therefore be excluded from further considerations.

The condition for stable/marginally stable/unstable spherical orbits [136]

$$\mathrm{d}^2R/\mathrm{d}r^2 \gtreqless 0 \tag{120}$$

implies the inequality

$$8r(3yr^4 - I^2r^3 + 3(1 - a^2y)r^2 - 3r + a^2) \gtreqless 0, \tag{121}$$

which has been checked on the radii of the spherical orbits $r = r_{\rm SPO}$ considered here. The equality in (120) gives the radii $r_{\rm ms}$ of the marginally stable orbits.

The curve $q_{\rm SPO}(X_{\rm SPO})$ plays crucial role in the construction of LECs/shadows, because in the parameter plane $(X - q)$ the curve determines the boundary between the photons with radial turning point and the photons escaping to "our" infinity ($r \to +\infty$), or to the secondary infinity ($r \to -\infty$). Therefore, the curve forms a "critical locus" in the $(X - q)$-plane (see [137]).

In the case of photon motion in the region of negative radii $r < 0$, there are no qualitative changes in its character for the spacetimes with $a^2y < 1$. This can be proved by analyzing the functions $X_{\rm SPO}(r)$, $q_{\rm SPO}(r)$ using the so-called "Chinese boxes" method (see [130]). The same applies to the critical locus, with typical behavior shown in Fig. 15.

3. Polar SPOs

The polar SPOs are of particular interest because the photons following these orbits cross the spin axis. The polar SPOs are characterized by the impact parameter $X_{\rm SPO} = -a$ $(\ell_{\rm SPO} = 0)$ which allows crossing of the symmetry axis. Using the definition of the impact parameter $\ell_{\rm SPO} = 0$ in Eq. (112), we get the equation

$$\frac{Ir^3 - 3r^2 + a^2Ir + a^2}{a[2yr^3 + (ya^2 - 1)r + 1]} = 0, \tag{122}$$

which has two positive roots

$$r^{\pm}_{\rm pol} = \frac{1}{I}\left[1 + 2\sqrt{1 - \frac{a^2I^2}{3}}\cos\left(\frac{\pi \pm \psi}{3}\right)\right], \tag{123}$$

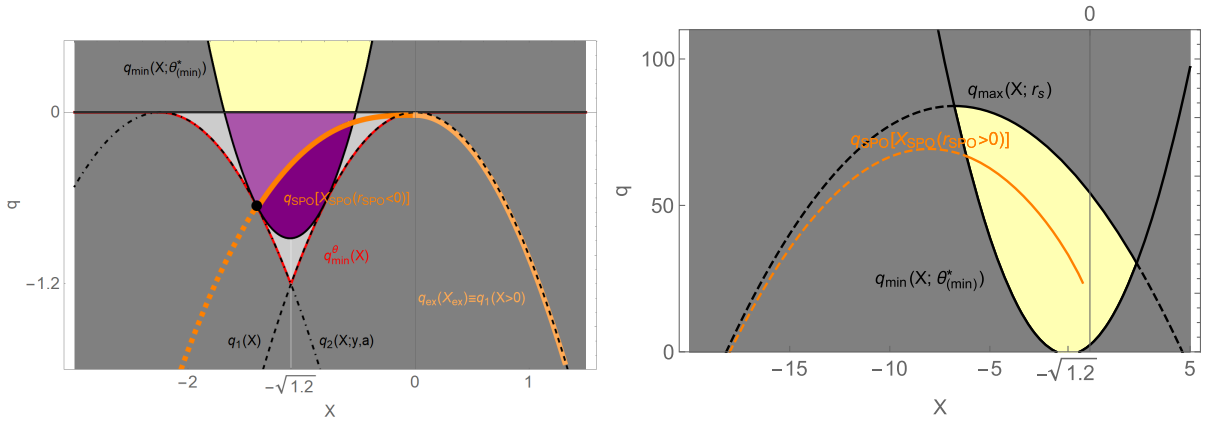

FIG. 15. (a) Representation of the NS shadow in the space of the photon motion constants $(X-q)$. The boundary of the shadow corresponds to the motion constants associated with the SPOs. Typical behavior of the critical locus $q_{\rm SPO}(X_{\rm SPO})$ (orange curve) corresponding to SPOs with negative radii $r_{\rm SPO}<0$ in spacetimes with $a^2y<1$, here represented by the case $y=0.02$, $a^2=1.2$. Above the locus there is a barrier (lighter purple area) which repels the incoming photons back to the region $r>0$, while the area below (darker purple) corresponds to photons, which can reach the other infinity $r\to-\infty$ depending on the latitude θ_e, which determines the opening of the function $q_{\rm min}(X;\theta_e)$. It is shown here for a deliberately chosen parameter $\theta_e=\theta^*_{\rm min}$, which represents a latitude of the off-equatorial unstable counter-rotating circular photon orbit, that is the lowest SPO of the given spacetime with radii $r^*_{\rm SPO}$. The corresponding motion constants are represented by the black dot and $\theta^*_{\rm min}=31.3°$, $r^*_{\rm SPO}=-0.54$. The curve denoted as $q_{ex}(X_{ex})$ and shown in lighter orange is obtained from the parametric expression of the dependence of the function (119) on the function (118) by eliminating of the parameter $r<0$. It coincides with the descending part of the function $q_1(X)$ and is completely in forbidden region (gray area), so it does not matter. (b) Continuation of the left figure—behavior of the critical locus corresponding to the SPOs of positive radii $r_{\rm SPO}>0$. The yellow area shows the allowed range of the motion constants determined by the conditions (68) and (72).

where

$$\cos\psi=\frac{a^2I^2-1}{\left(1-\frac{a^2I^2}{3}\right)^{3/2}}. \tag{124}$$

The maximum spin parameter $a^2_{\rm max(pol)}$ allowing the existence of the polar SPOs at positive radii, is determined by the condition

$$\cos\psi=1, \tag{125}$$

which gives

$$a^2_{\rm max(pol)}(y)\equiv\frac{2}{3y}\left(\cosh\frac{\xi}{3}-1\right). \tag{126}$$

Here

$$\cosh\xi=\frac{27}{2}ya^2_{{\rm max(pol)}K}+1 \tag{127}$$

and

$$a^2_{{\rm max(pol)}K}=6\sqrt{3}-9=1.3923 \tag{128}$$

is the maximum value of a^2 that allows for the existence of polar SPOs in the Kerr case (cf. [134]).

There is always one other solution of Eq. (122) corresponding to the polar SPO at negative radii $r^{(-)}_{\rm pol}$, which is as follows:

$$r^{(-)}_{\rm pol}\equiv\begin{cases}\frac{1}{I}\left[1-2\sqrt{1-\frac{a^2I^2}{3}}\cos\left(\frac{\hat\psi}{3}\right)\right], & \text{for } a^2I^2<3;\\ \frac{1}{I}\left[1-2\sqrt{\frac{a^2I^2}{3}-1}\sinh\left(\frac{\bar\psi}{3}\right)\right], & \text{for } a^2I^2\geq 3,\end{cases} \tag{129}$$

where

$$\cos\hat\psi=\frac{a^2I^2-1}{\left(1-\frac{a^2I^2}{3}\right)^{3/2}} \tag{130}$$

and

$$\sinh\bar\psi=\frac{a^2I^2-1}{\left(\frac{a^2I^2}{3}-1\right)^{3/2}}. \tag{131}$$

E. Orientation of the SPOs

We define the orientation of the SPOs in the LNRFs according to the sign of the azimuthal component $k^{(\phi)}$ of the four-momentum (wave vector) $\mathbf{k}$ of the future-directed

photon, $k^{(t)} > 0$. For this purpose it is convenient to introduce an angle Ψ (see [110]) such that

$$\sin\Psi \equiv k^{(\phi)}/k^{(t)}, \tag{132}$$

i.e., $\Psi = 0$ for motion in the direction of the latitudinal basis vector $e_{(\theta)}$, $\Psi = \pi/2$ for motion in the direction of the azimuthal basis vector $e_{(\phi)}$. According to Eq. (65) it is $k^{(\phi)} = k_{(\phi)}, k^{(t)} = -k_{(t)}$, and we can write

$$\sin\Psi = -\frac{k_{(\phi)}}{k_{(t)}} = -\frac{k_\mu e^\mu_{(\phi)}}{k_\nu e^\nu_{(t)}} = -\frac{k_\phi e^\phi_{(\phi)}}{k_t e^t_{(t)} + k_\phi e^\phi_{(t)}}. \tag{133}$$

Using the relations (36), (37), and (48), and after substituting from Eqs. (28) and (31), we finally get

$$\sin\Psi = \rho^2\sqrt{\frac{\Delta_r\Delta_\theta}{A^2\sin^2\theta}}\cdot\frac{\ell}{1-\Omega_{\mathrm{LNRF}}\ell}. \tag{134}$$

In general, the function $\sin\Psi$ defined in relation (134) determines the instantaneous locally measured azimuthal orientation of a photon passing through the current coordinates (r,θ), with a generally nonzero locally measured radial velocity, these measurements being made by the observer in the LNRF. As this equation implies, this instantaneous orientation at a given photon location depends only on the impact parameter ℓ. In the case of SPO photons at a given radius r, the impact parameter ℓ is fixed at $\ell = \ell_{\mathrm{SPO}}(r)$, along with the impact parameter $q = q_{\mathrm{SPO}}(r)$, which is irrelevant for the orientation of the motion.

Now we can show that the sign of the function $\sin\Psi$ remains unchanged for the SPOs of a fixed radius, independently of the latitudinal coordinate of the photon, so that it does indeed express the orientation of any given SPO.

1. Orientation and latitudinal range of the SPOs

To discuss the locally measured orientation of the azimuthal motion of a photon at a given SPO in a given KdS spacetime, it is convenient to introduce the function

$$Z_\theta \equiv \rho^2\sqrt{\frac{\Delta_r\Delta_\theta}{A^2\sin^2\theta}}, \tag{135}$$

where the subscript θ indicates only the dependence on the photon latitude. It is obvious that $Z_\theta > 0$ for any latitude at the stationary region $\Delta_r > 0$. Equation (134) can then be written in the form

$$\sin\Psi = \frac{Z_\theta\ell}{1-\Omega_{\mathrm{LNRF}}(r,\theta)\ell}. \tag{136}$$

We can easily see that the metric coefficients imply the relation

$$g_{tt} = g_{\phi\phi}(\Omega^2_{\mathrm{LNRF}} - Z^2_\theta). \tag{137}$$

In the region of positive radii, $g_{\phi\phi} > 0$, so in the ergosphere, where $g_{tt} > 0$, the inequality $0 < Z_\theta < \Omega_{\mathrm{LNRF}}$ holds, while outside the ergosphere, $g_{tt} < 0$, the inequality $0 < \Omega_{\mathrm{LNRF}} < Z_\theta$ holds. At the ergosphere boundary, i.e., at the ergosurface where $g_{tt} = 0$, the equality $\Omega_{\mathrm{LNRF}} = Z_\theta$ holds, so the quantity Z_θ corresponds to the angular velocity of the LNRF observer located at the ergosurface.

However, there is a causality violation region where $g_{tt} > 0$ and $g_{\phi\phi} < 0$ in the region of negative radii. In such a case the function A, defined in relation (27), is negative and the relations (28)–(31) and (32)–(35) for the local tetrads and hence the locally measured quantities have to be redefined. We will leave the discussion for this case for the next study, and here we restrict ourselves to the noncausal violation region where $g_{tt} < 0$ and $g_{\phi\phi} > 0$ in the case of negative radii.

Now we can easily determine the sign of the function $\sin\Psi$ for given spacetime parameters a^2, y and photons orbiting on a given SPO with radius $r = r_{\mathrm{SPO}}$ and with a given impact parameter $\ell(r_{\mathrm{SPO}})$. A direct analysis of the function $\sin\Psi$ with respect to the variable θ is rather tedious, but, as we shall see below, it is sufficient for our purposes to compare the values of the expressions $(\Omega_{\mathrm{LNRF}} - Z_\theta)^{-1}$, $(\Omega_{\mathrm{LNRF}} + Z_\theta)^{-1}$ as a function of the angle θ with the motion constant ℓ. Typical behavior of the functions $(\Omega_{\mathrm{LNRF}} + Z_\theta)^{-1}$, $(\Omega_{\mathrm{LNRF}} - Z_\theta)^{-1}$ and the regions of the prograde and retrograde orbits defined by them are shown in Figs. 16–18, which provides an overview for the following discussion.

We first investigate the condition for prograde orbits, which reads

$$0 \le \sin\Psi \le 1. \tag{138}$$

We solve this double-sided inequality separately for the positivity condition

$$0 \le \sin\Psi, \tag{139}$$

and separately for the reality condition

$$\sin\Psi \le 1, \tag{140}$$

which must be satisfied simultaneously. Obviously, the positivity condition (139) implies

$$0 \le \ell < \Omega^{-1}_{\mathrm{LNRF}}, \tag{141}$$

as can be seen from the auxiliary Table I.

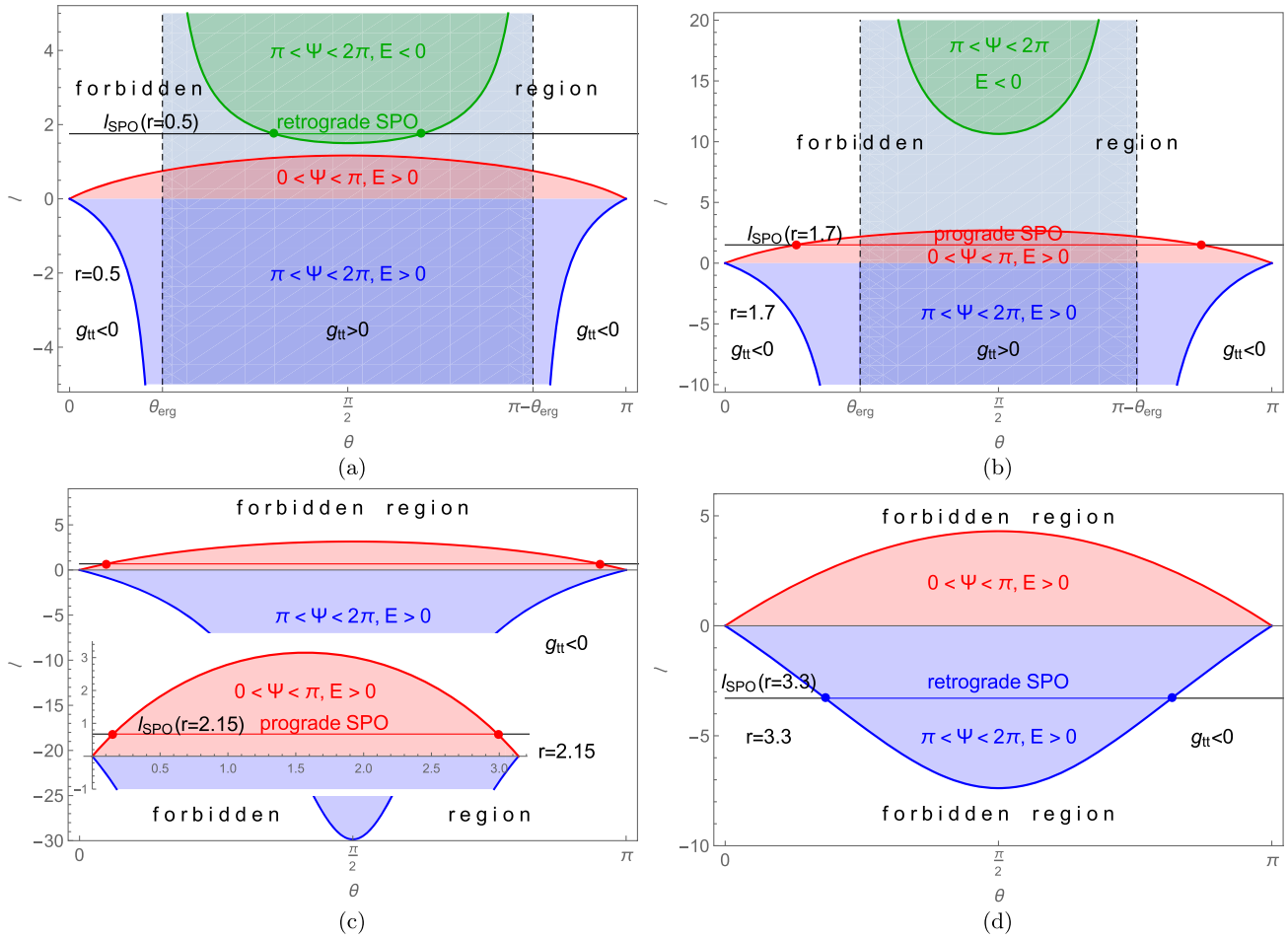

FIG. 16. The latitudinal range of motion of the photons and the orientation of their azimuthal motion given for typical radii at the Kerr–de Sitter naked singularity spacetimes with parameters $a^2 = 1.001$, $y = 10^{-5}$. The extension in the latitudinal coordinate θ is given in terms of the impact parameter ℓ. A photon with a certain impact parameter ℓ moves in the latitudinal direction between two latitudinal turning points, symmetrically located with respect to the equatorial plane, which correspond to the intersections of the line $\ell = \text{const.}$ with the curves $(\Omega_{\text{LNRF}} + Z_\theta)^{-1}$ (red curve), $(\Omega_{\text{LNRF}} - Z_\theta)^{-1}$ (blue curve), where the intersections with the curve $(\Omega_{\text{LNRF}} + Z_\theta)^{-1}/(\Omega_{\text{LNRF}} - Z_\theta)^{-1}$ define motion in the positive/negative azimuthal direction, i.e., prograde/retrograde trajectories (red/blue region), with a generally nonzero radial component of motion. The SPO photons in a particular radius r_{SPO} are determined by the special $\ell = \ell_{\text{SPO}}(r)$. Such photons have $q = q_{\text{SPO}}(r)$, that does not matter for the orientation of the motion. Such photons are forced to oscillate between two latitudes, represented as the red/blue dots, while the motion continues in fixed azimuthal direction. Photons with $\ell \neq \ell_{\text{SPO}}(r)$- case have the turning point of the θ-motion at this r_{SPO}, if their impact parameter q is chosen properly, but they move in the radial direction. Therefore, the SPOs of photons with motion retrograde to the local LNRFs are shown in the blue region, while prograde SPOs are shown in the red region; the special case of retrograde SPOs of photons with $\ell > 0$ and $E < 0$, which lie entirely in the ergosphere, is shown in green. The region of the ergosphere is shown in Figs. 16(a) and 16(b) by a band of gray color overlaying other colored regions, defined by vertical dashed lines, which also represent asymptotes of the function $(\Omega_{\text{LNRF}} - Z_\theta)^{-1}$. The latitudinal extent of the ergosphere at a given radius r_{SPO} is $\theta_{\text{erg}}(r_{\text{SPO}}) \leq \theta \leq \pi - \theta_{\text{erg}}(r_{\text{SPO}})$, where $\theta_{\text{erg}}(r_{\text{SPO}})$ is given by the relation (23). The radii of SPOs of a certain type of stability, orientation and sign of covariant energy E fall into intervals defined by specific values of $r^{+}_{d(\text{SPO})}$, $r^{\pm}_{\text{pol}}$, r_{ms}, r^{-}_{ph} as described in the text. (a) Radius $r_{\text{SPO}} = 0.5$ corresponds to the case $0 < r_{\text{SPO}} < r^{+}_{d(\text{SPO})}$; the SPO photons move in a retrograde direction along a stable SPO that is completely embedded in the ergosphere, with a positive impact parameter ℓ and with a negative covariant energy $E < 0$. (b) Radius $r_{\text{SPO}} = 1.7$ corresponds to the case $r_{\text{ms}} < r_{\text{SPO}} < r^{-}_{\text{pol}}$; the SPO photons move in a prograde direction along an unstable SPO that partially interferes with the ergosphere, with a positive impact parameter ℓ and with a positive covariant energy $E > 0$. (c) Radius $r_{\text{SPO}} = 2.15$ is in the same interval as in case (b) but now the SPO is outside the ergosphere. (d) Radius $r_{\text{SPO}} = 3.3$ corresponds to the case $r^{-}_{\text{pol}} < r_{\text{SPO}} < r^{-}_{\text{ph}}$; the SPO photons move retrogradely along an unstable SPO, completely outside the ergosphere, with a negative impact parameter and positive covariant energy $E > 0$. The selected radii are highlighted by horizontal dotted lines in Fig. 19(a), which shows the distribution of different types of SPOs in the considered spacetime. Other qualitatively different cases of orbits are shown in Fig. 17 for a spacetime with parameters $a^2 = 1.2$, $y = 0.02$, for which they can be displayed more clearly, and which differs from the one considered here in that its ergosphere extends into a region of unstable retrograde orbits [cf. cases (a), (b) in Fig. 19].

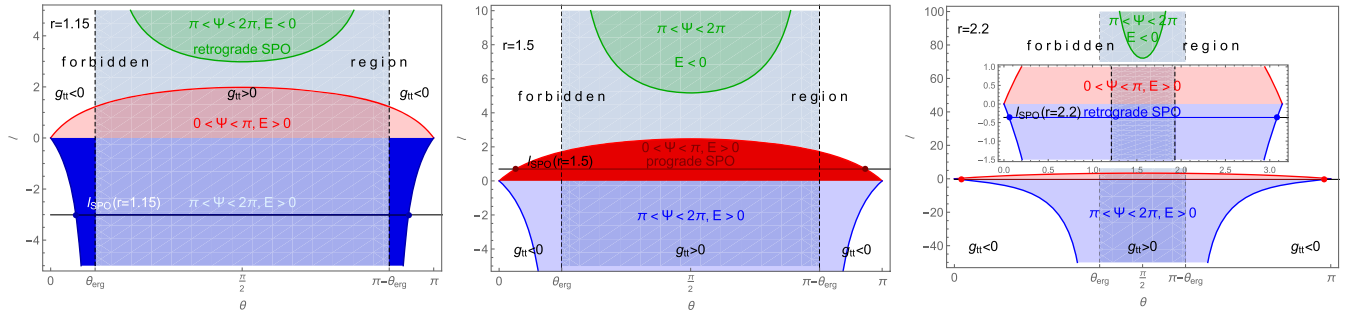

FIG. 17. The latitudinal range of motion of the photons and the orientation of their azimuthal motion given for typical radii at the Kerr–de Sitter naked singularity spacetimes with parameters $a^2 = 1.2$, $y = 0.02$. This figure follows Fig. 16 in an analogous way and shows other qualitatively different cases of SPOs, which for the spacetime case in Fig. 16 either do not occur or could not be displayed clearly due to disproportions. (a) Radius $r_{\rm SPO} = 1.15$ corresponds to the case $r^+_{d({\rm SPO})} < r_{\rm SPO} < r^+_{\rm pol}$; the SPO photons move in a retrograde direction along a stable SPO that partially interferes with the ergosphere, with a negative impact parameter ℓ and with a positive covariant energy $E > 0$. (b) Radius $r_{\rm SPO} = 1.5$ corresponds to the case $r^+_{\rm pol} < r_{\rm SPO} < r_{\rm ms}$; the SPO photons move in a prograde direction along a stable SPO that partially interferes with the ergosphere, with a positive impact parameter ℓ and with a positive covariant energy $E > 0$. (c) Radius $r_{\rm SPO} = 2.2$ corresponds to the case $r^-_{\rm pol} < r_{\rm SPO} < r^-_{\rm ph}$; the SPO photons move in a retrograde direction along an unstable SPO that partially interferes with the ergosphere, with a negative impact parameter ℓ and with a positive covariant energy $E > 0$. The selected radii are highlighted by horizontal dotted lines in Fig. 19(b), which shows the distribution of different types of SPOs in the considered spacetime.

The reality condition (140) implies an inequality

$$\sin\Psi - 1 = \frac{(\Omega_{\rm LNRF} + Z_\theta)\ell - 1}{1 - \Omega_{\rm LNRF}\ell} \le 0, \tag{142}$$

which has solutions

$$\ell \le (\Omega_{\rm LNRF} + Z_\theta)^{-1} \quad \text{or} \quad \Omega^{-1}_{\rm LNRF} < \ell, \tag{143}$$

as follows from the auxiliary Table II. The conjunction of the inequalities (141) and (143) gives the solution to the inequality (138) in the form

$$0 \le \ell \le (\Omega_{\rm LNRF} + Z_\theta)^{-1} < \Omega^{-1}_{\rm LNRF}, \tag{144}$$

which corresponds to the red regions shown in Figs. 16–18.

The condition for retrograde orbits

$$-1 \le \sin\Psi \le 0 \tag{145}$$

is treated in the same way. From the Table I it can be seen that the negativity condition

$$\sin\Psi \le 0 \tag{146}$$

is satisfied for

$$-\infty < \ell \le 0 \quad \text{or} \quad \Omega^{-1}_{\rm LNRF} \le \ell. \tag{147}$$

The reality condition

$$-1 \le \sin\Psi \tag{148}$$

implies the inequality

$$0 \le \frac{(Z_\theta - \Omega_{\rm LNRF})\ell + 1}{1 - \Omega_{\rm LNRF}\ell} = \sin\Psi + 1, \tag{149}$$

which must be solved separately for the motion inside the ergosphere, $g_{tt} > 0$, where $Z_\theta - \Omega_{\rm LNRF} < 0$, and outside the ergosphere, $g_{tt} < 0$, where $Z_\theta - \Omega_{\rm LNRF} > 0$ in the case of positive radii.

In the case of motion inside the ergosphere, the inequality (149) has solutions

$$-\infty < \ell < \Omega^{-1}_{\rm LNRF} \quad \text{or} \quad (\Omega_{\rm LNRF} - Z_\theta)^{-1} \le \ell < \infty, \tag{150}$$

as follows from the auxiliary Table III. The conjunction of the inequalities (147) and (150) then gives the solution of the inequality (145) in the form

$$-\infty < \ell \le 0 \tag{151}$$

or

$$(\Omega_{\rm LNRF} - Z_\theta)^{-1} \le \ell < \infty. \tag{152}$$

The inequality (151)/(152) corresponds to the blue/green regions shown in Figs. 16(a), 16(b), and 17 between the vertical dashed lines. Note that by the relation (152) there are locally retrograde photons with positive-impact parameter ℓ. In order to preserve the standard physical meaning for the locally measured $k^{(t)}$, i.e., $k^{(t)} > 0$, we have to set

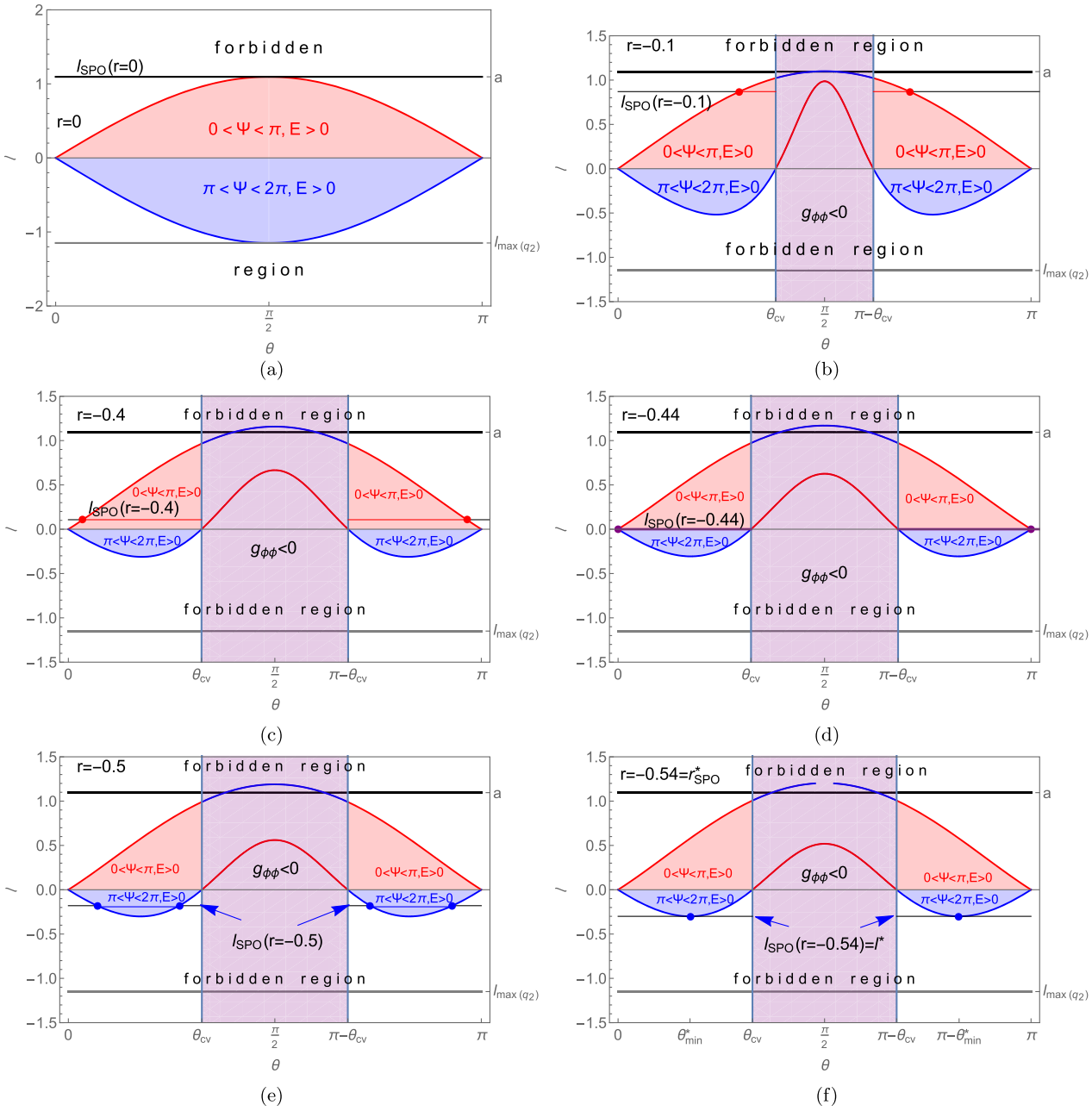

FIG. 18. The latitudinal range of motion of the photons and the orientation of their azimuthal motion given for selected negative radii in the Kerr–de Sitter naked singularity spacetimes with parameters $a^2 = 1.2$, $y = 0.02$. The coloring follows Figs. 16 and 17 in an analogous way and shows other qualitatively different cases of SPOs. The black and gray horizontal lines define the range of allowed values of the impact parameter ℓ, which are given by the constraints imposed on the latitudinal motion according to Eq. (87). The purple vertical band corresponds to the region of causality violation where $g_{\phi\phi} < 0$ ($A < 0$), restricted in the latitudinal direction at a given radius r to the interval $\theta_{CV} \leq \theta \leq \pi - \theta_{CV}$. Note that in the causality violation region the equations of motion have to be modified due to the interchange of the character of the ϕ, t coordinates. Here we are not discussing these subtleties, as ϕ is not spacelike coordinate in the causality violation region being thus irrelevant for our discussion. Outside the causality violation region the behavior is standard, but partly it corresponds to the vortical motion. The individual cases correspond to the following situations: (a) Radius $r_{SPO} = 0$ does not correspond to a SPO, but the photon trajectory terminates in the ring singularity. (b) and (c) Unstable prograde SPOs; photons enter the causality violation region. (d) Unstable polar SPO at radius $r^{(-)}_{pol}$ given by Eq. (129); photons oscillate above the "north"/"south" pole with latitudinal turning point $\theta_{pol}/(\pi - \theta_{pol})$, which merges with the boundary point $\theta_{CV}/(\pi - \theta_{CV})$ of the causality violation region. (e) Unstable retrograde SPOs; vortical motion between two latitudinal turning points "above"/"below" the equatorial plane outside the area of causality violation. (f) Off-equatorial unstable retrograde circular photon orbit of the θ^* photons with the motion constants given by Eqs. (102) and (103), following the constant latitude $\theta^*_{min} = 31.3°$, cf. Figs. 11 and 15(a). The radius r^*_{SPO} corresponds to the "deepest" SPO enclosing the region of the SPOs.

TABLE I. Auxiliary table for determining the sign of $\sin\Psi$.

ℓ	$(-\infty;0]$	$[0;\Omega_{\mathrm{LNRF}}^{-1})$	$(\Omega_{\mathrm{LNRF}}^{-1};\infty)$
$Z_\theta\ell$	$-$	$+$	$+$
$1-\Omega_{\mathrm{LNRF}}\ell$	$+$	$+$	$-$
$\sin\Psi$	$-$	$+$	$-$

TABLE II. Auxiliary table for solving the inequality $\sin\Psi\leq 1$.

ℓ	$(-\infty;\frac{1}{\Omega_{\mathrm{LNRF}}+Z_\theta}]$	$[\frac{1}{\Omega_{\mathrm{LNRF}}+Z_\theta};\frac{1}{\Omega_{\mathrm{LNRF}}})$	$(\frac{1}{\Omega_{\mathrm{LNRF}}};\infty)$
$(\Omega_{\mathrm{LNRF}}+Z_\theta)\ell-1$	$-$	$+$	$+$
$1-\Omega_{\mathrm{LNRF}}\ell$	$+$	$+$	$-$
$\sin\Psi-1$	$-$	$+$	$-$

TABLE III. Auxiliary table for solving the inequality $-1\leq\sin\Psi$ in the case of $g_{tt}>0$.

ℓ	$(-\infty;\frac{1}{\Omega_{\mathrm{LNRF}}})$	$(\frac{1}{\Omega_{\mathrm{LNRF}}};\frac{1}{\Omega_{\mathrm{LNRF}}-Z_\theta}]$	$[\frac{1}{\Omega_{\mathrm{LNRF}}-Z_\theta};\infty)$
$(Z_\theta-\Omega_{\mathrm{LNRF}})\ell+1$	$+$	$+$	$-$
$1-\Omega_{\mathrm{LNRF}}\ell$	$+$	$-$	$-$
$\sin\Psi+1$	$+$	$-$	$+$

$k^{(\phi)}<0$, or, equivalently, $\Phi<0$, as follows from $k^{(\phi)}=k_{(\phi)}=\Phi e^{\phi}_{(\phi)}$. Therefore, by the definition (48), such photons must have negative covariant energy $E<0$ and such SPOs must be completely immersed in the ergosphere (see [110]). The area of these orbits is marked in green.

In the case of motion outside the ergosphere, the inequality (149) has a solution

$$(\Omega_{\mathrm{LNRF}}-Z_\theta)^{-1}\leq\ell<\Omega_{\mathrm{LNRF}}^{-1}, \tag{153}$$

as follows from the auxiliary Table IV. The conjunction of inequalities (147) and (153) now gives the solution of the inequality (145) in the form

$$(\Omega_{\mathrm{LNRF}}-Z_\theta)^{-1}\leq\ell\leq 0, \tag{154}$$

which corresponds to the blue regions shown in Figs. 16(a), 16(b), and 17 outside the belt bounded by the vertical dashed lines and the blue region shown in Figs. 16(c), 16(d), and 18.

TABLE IV. Auxiliary table for solving the inequality $-1\leq\sin\Psi$ in the case of $g_{tt}<0$.

ℓ	$(-\infty;\frac{1}{\Omega_{\mathrm{LNRF}}-Z_\theta}]$	$[\frac{1}{\Omega_{\mathrm{LNRF}}-Z_\theta};\frac{1}{\Omega_{\mathrm{LNRF}}})$	$(\frac{1}{\Omega_{\mathrm{LNRF}}};\infty)$
$(Z_\theta-\Omega_{\mathrm{LNRF}})\ell+1$	$-$	$+$	$+$
$1-\Omega_{\mathrm{LNRF}}\ell$	$+$	$+$	$-$
$\sin\Psi+1$	$-$	$+$	$-$

As shown above, the orientation of the photon motion relative to the LNRFs is governed only by the impact parameter ℓ. In Figs. 16 and 17, we show several typical cases of the extension of the latitudinal motion of the SPO photons at positive radii along with to the motion orientation relative to the LNRFs for a given choice of the impact parameter ℓ_{SPO} for KdS NS spacetimes represented by the spacetime parameters $a^2=0.001, y=10^{-5}$ with comparison to the situation for the KdS NS spacetimes with larger parameters—$a^2=1.2, y=0.02$ where the retrograde SPOs enter the ergosphere.

In the region of positive radii $r>0$, for a given radius r, the allowed values of the impact parameter ℓ are given by the constraints imposed on radial motion by Eq. (66). Therefore, in Figs. 16 and 17 the values of the local extrema of the functions $(\Omega_{\mathrm{LNRF}}+Z_\theta)^{-1}(\theta;r)$, $(\Omega_{\mathrm{LNRF}}-Z_\theta)^{-1}(\theta;r)$ at the point $\theta=\pi/2$, which determine the range of the allowed values of the impact parameter ℓ at given radius r, are given by the values of the effective potentials $\ell^r_\pm(r;q=0,y,a^2)$, i.e.,

$$(\Omega_{\mathrm{LNRF}}+Z_\theta)^{-1}(\theta=\pi/2,r)=\ell^r_-(r,q=0), \tag{155}$$

$$(\Omega_{\mathrm{LNRF}}-Z_\theta)^{-1}(\theta=\pi/2,r)=\ell^r_+(r,q=0), \tag{156}$$

where we have introduced the notation

$$\ell^r_\pm(r,q)\equiv X^r_\pm(r,q)+a, \tag{157}$$

with $X^r_\pm(r,q)$ defined in relation (70).

In Fig. 18, we show for completeness the latitudinal extent of the SPOs and their orientation on the negative radii. The photon motion at negative radii does not differ qualitatively between the KdS spacetimes of different cosmological parameters, so we consider here the representative case of a spacetime with parameters $a^2=1.2$, $y=0.02$. The local extrema of the functions $(\Omega_{\mathrm{LNRF}}+Z_\theta)^{-1}(\theta;r)$, $(\Omega_{\mathrm{LNRF}}-Z_\theta)^{-1}(\theta;r)$ at $\theta=\pi/2$ in the case of $r<0$ fall into the domain of causality violation, the discussion of which we postpone for another detailed study of the character of the motion in the causality violation region.

From the comment to Figs. 16–18 it follows that although the individual functions $(\Omega_{\mathrm{LNRF}}+Z_\theta)^{-1}$, $(\Omega_{\mathrm{LNRF}}-Z_\theta)^{-1}$ change their value depending on the latitude θ, a photon with a given impact parameter ℓ does not change the azimuthal direction of motion with respect to the LNRF observer currently orbiting at the photon location, i.e., the photon remains to be at either a prograde or retrograde SPO. The photons following the prograde/retrograde SPO in given reference frame we also call locally corotating/counterrotating, but these attributes can be generalized to any motion, where the term corotating/counterrotating

means a motion that satisfies the condition (138)/(145), i.e., in accordance with our intuition, particles following them are proceeding in a positive/negative azimuthal direction relative to the local LNRF.

2. Distribution of the SPOs

In Figs. 19 and 20 we give for the same KdS NS spacetimes the dependence of the extension of the latitudinal motion and in Figs. 21 and 22 the dependence of the motion constants $\ell_{\rm SPO}$, $q_{\rm SPO}$ of the SPO photon on the radius of the SPO. For a class IVa KdS NS which belongs to the family of observationally acceptable spacetimes, at the region of positive radii the SPOs are located in the interval $0 < r_{\rm SPO} < r^{-}_{\rm ph}$, where $r^{-}_{\rm ph}$ denotes the retrograde equatorial circular photon orbit (ECPO), which is given by the positive root of the function $q_{\rm SPO}(r)$. There are two polar SPOs, the stable one at $r^{+}_{\rm pol}$ and unstable one at $r^{-}_{\rm pol}$ given by Eq. (123), $r^{+}_{\rm pol} < r^{-}_{\rm pol} < r^{-}_{\rm ph}$. The distribution of the SPOs is shown in Figs. 19 and 20. The prograde SPOs are located in the interval $r^{+}_{\rm pol} < r < r^{-}_{\rm pol}$; stable at $r^{+}_{\rm pol} < r_{\rm ms}$ and unstable at $r_{\rm ms} < r^{-}_{\rm pol}$, where $r_{\rm ms}$ denotes the radius of the marginally stable SPO, which is given by the local maximum of the function $\ell_{\rm SPO}(r)$ [or local minimum of the function $q_{\rm SPO}(r)$]. The retrograde unstable SPOs are at $r^{-}_{\rm pol} < r^{-}_{\rm ph}$, and stable at $0 < r < r^{+}_{\rm pol}$. The SPOs that are completely embedded in the ergosphere, orbited by locally retrograde photons with positive impact parameter $\ell_{\rm SPO}$ and with negative covariant energy $E < 0$, are in the interval $0 < r < r^{+}_{d({\rm SPO})}$, orbits with positive covariant energy $E > 0$ are in the interval $r^{+}_{d({\rm SPO})} < r < r^{-}_{\rm ph}$, where $r^{+}_{d({\rm SPO})}$ is the point at which the functions $\ell_{\rm SPO}(r)$, $q_{\rm SPO}(r)$ diverge, defined in relation (115).

In the case of negative radii, only unstable SPOs exist. The prograde SPOs are at $r^{(-)}_{\rm pol} < r < 0$, which enter the region of the causality violations in the vicinity of the equatorial plane $\theta = \pi/2$ and which study we postpone to another paper. The retrograde SPOs are in the interval $r^{*}_{\rm SPO} < r < r^{(-)}_{\rm pol}$. Photons in these SPOs perform so-called vortical motion, during which they oscillate between two latitudinal turning points that are in the same half-space with the equatorial boundary plane. The lowest SPO at $r = r^{*}_{\rm SPO}$ is purely circular.

For completeness, we still investigate the radial extent of the causality violation region, which is given by the condition $g_{\phi\phi} < 0$. As shown in Fig. 20, this radial extent is largest for $\theta = \pi/2$, where it is limited by the value of

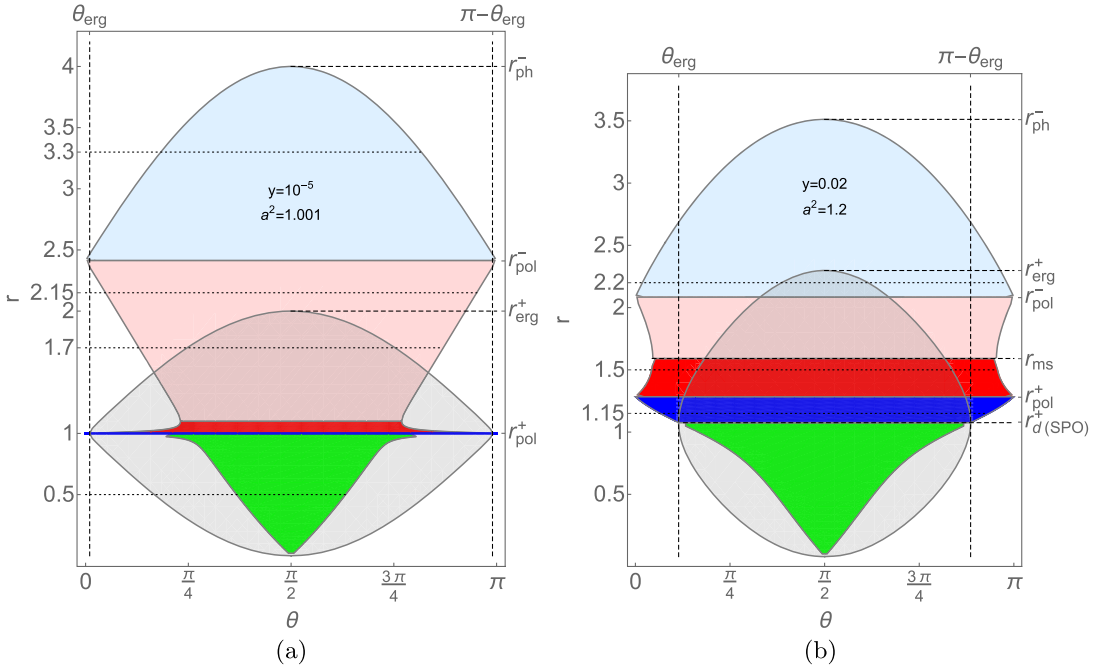

FIG. 19. Distribution of the SPOs in the class IVa KdS NS spacetimes. The red/blue color corresponds to the locally prograde/retrograde SPOs, the full/faint shades correspond to the stable/unstable SPOs. The green color corresponds to the locally retrograde SPOs with negative covariant energy $E < 0$. The gray area shows the ergosphere. The dashed/dotted lines indicate prominent orbits/orbits for which the latitudinal motion ranges are shown in Figs. 16 and 17. The intersections of the dotted horizontal lines with the gray curve determine the latitudinal extent of the ergosphere at a given radius $r_{\rm SPO}$. Figure 19(a) shows spacetimes where unstable prograde SPOs exist outside the ergosphere, while the Fig. 19(b) corresponds to spacetimes where the ergosphere extends into the region of unstable retrograde SPOs. The region of stable retrograde orbits in Fig. 19(a) a is faint due to the small scale, and the radii $r_{\rm ms}$, $r^{+}_{d({\rm SPO})}$ are not marked for clarity, since they almost merge with the radius $r^{+}_{d({\rm SPO})}$.

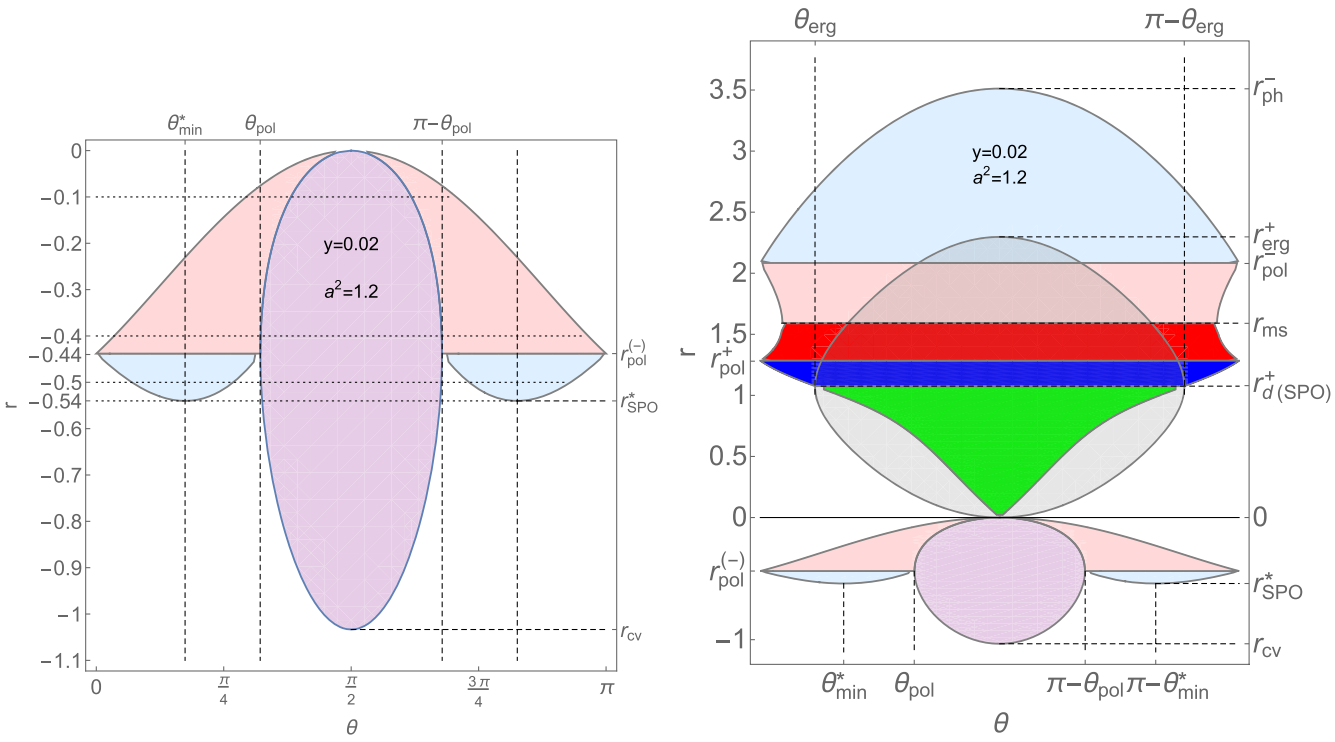

FIG. 20. (a) Distribution of the SPOs in the region of negative radii in the class IVa KdS NS spacetimes. The color distinction has the same meaning as in Fig. 18. The dashed/dotted lines indicate prominent orbits/orbits for which the latitudinal motion ranges are shown in Fig. 18. The radius r_{cv} denotes the radial extent of the causality violation region. (b) Distribution of the SPOs in the region of negative radii of the same KdS NS spacetime in comparison to the region of the SPOs at positive radii. The prominent radii and latitudes are marked.

r_{CV}. This radius is given by the condition $g_{\phi\phi} = 0$, which implies the equality $A = 0$. Substituting $\theta = \pi/2$ into the definitional relation (27) for the function A gives the equation,

$$r(Ir^3 + a^2 Ir + 2a^2) = 0, \tag{158}$$

which is obviously satisfied for $r = 0$. The cubic polynomial in Eq. (158) always has two complex conjugate roots and one negative root,

$$r_{CV} = \frac{-2\sqrt{3}}{3} a \sinh\left[\frac{1}{3}\sinh^{-1}\frac{3\sqrt{3}}{Ia}\right]. \tag{159}$$

It can be shown that the following inequality holds

$$r^{(-)}_{erg} < r^{(-)}_{d(SPO)} < r_{CV} < r^{*}_{SPO} < r^{(-)}_{pol} < 0. \tag{160}$$

The radial extent in the equatorial plane of the causality violation region is then given by the interval $r_{CV} \leq r \leq 0$.

3. *Spacetime differentiation according to the relative position of the ergosphere and the SPOs region*

The KdS NS spacetimes represented by the spacetime parameters $a^2 = 0.001, y = 10^{-5}$ and $a^2 = 1.2, y = 0.02$, for which we have constructed the figures above, differ in the extension of the SPOs relative to the ergosphere. The limiting values of the cosmological parameters that separate spacetimes with ergosphere in the region of unstable prograde orbits from spacetimes with ergosphere extending into the region of unstable retrograde orbits are given by

$$r^{+}_{erg} = r^{-}_{pol}, \tag{161}$$

whose solution can be written in the parametric form,

$$a^2 = a^2_{erg-pol}(r) \equiv \frac{3r^2 - r^3}{2r - 1}, \tag{162}$$

$$y = y_{erg-pol}(r) \equiv \frac{2r^2 - 5r + 2}{r^3(r + 2)}, \tag{163}$$

with respect to the variables a^2, y. It follows from the Eqs. (162) and (163) that in the case of pure Kerr spacetime ($y = 0$) the ergosurface just meets the region

of unstable retrograde SPOs at $r = 2$ for $a^2 = 4/3$, which corresponds to Kerr NS spacetime, while in the case of SdS spacetime ($a^2 = 0$) this situation occurs at $r = 3$ for $y = 1/27 = y_{\mathrm{crit(SdS)}}$, which corresponds to the extreme SdS BH spacetime.

For completeness, let us note that equality $r^+_{\mathrm{erg}} = r^-_{\mathrm{ph}}$ is satisfied if and only if $r^+_{\mathrm{erg}} = r^-_{\mathrm{erg}}$, i.e., the inner ergosphere reaches the limit of the unstable retrograde SPOs at r^-_{ph} simultaneously with the limit of the cosmological ergosphere, which occurs at the static radius r_s. Therefore, in such situation, $r^+_{\mathrm{erg}} = r^-_{\mathrm{ph}} = r^-_{\mathrm{erg}} = r_s$, and the spacetime parameters a^2, y corresponding to this limiting case are described in the parameter plane (a^2, y) by the $a^2_{\mathrm{erg}-s}(y)$ curve defined by the relation (18).

Furthermore, in paper [110] we defined classes I, and II of the KdS BH spacetimes, which differ in that in the equatorial plane in class I the radius r^+_{erg} of the inner ergosphere boundary lies above the outer BH horizon at r_o and below the unstable corotating equatorial circular photon orbit ECPO at r^+_{ph}, forming the inner boundary of the SPOs region, $r_o < r^+_{\mathrm{erg}} < r^+_{\mathrm{ph}}$, while in class II the ergosphere extends into the SPOs region, $r^+_{\mathrm{ph}} < r^+_{\mathrm{erg}}$. Here we denote the curve that separates the two classes of spacetimes in the parameter plane (a^2, y) by $a^2_{I-II}(y)$. The curve $(a^2_{\mathrm{erg-pol}}(r), y_{\mathrm{erg-pol}}(r))$, hereafter denoted by $a^2_{\mathrm{erg-pol}}(y)$ for short, parametrized by $2 < r < 3$, and the curves $a^2_{I-II}(y)$, $a^2_{\mathrm{erg}-s}(y)$ are shown in comparison to the curves $a^2_{\mathrm{min}(h)}(y)$, $a^2_{\mathrm{max}(h)}(y)$, which determine the boundary between the BH and NS spacetimes, in Fig. 23.

F. Classification of the KdS spacetimes due to photon motion

The separation of the KdS BH and NS spacetimes in the parameter space $(a^2 - y)$ by the relations of the horizons and ergosurfaces is shown in Fig. 5. A more detailed classification of the KdS spacetimes into individual classes, first introduced in [110] and denoted by Roman numerals I–VIII, is shown in Fig. 24—it also takes into account the character of the SPOs, including their number, their stability with respect to the radial perturbations, their orientation, their relative position to the ergosphere and the existence of polar SPOs, i.e., SPOs crossing the symmetry axis. All these characteristics of the photon motion, together with the special class of the photons moving along constant latitudes,

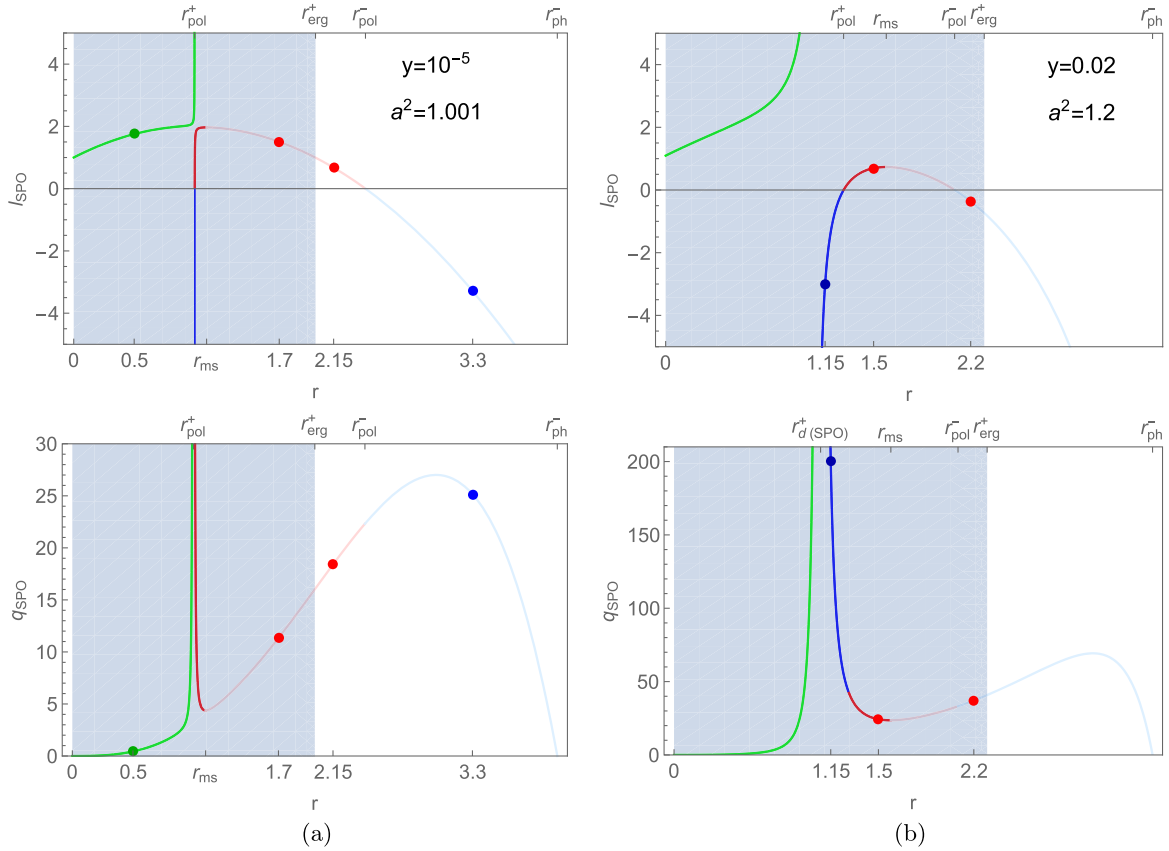

FIG. 21. Dependence of the motion constants ℓ_{SPO}, q_{SPO} of the SPO photons on the radius r_{SPO} of the corresponding orbit for the spacetimes considered above. The different sections of the curves are color-coded according to the orbital type in the color style as in Figs. 16–19. The colored dots highlight the radial coordinates of the characteristic SPOs considered in Figs. 16–19.

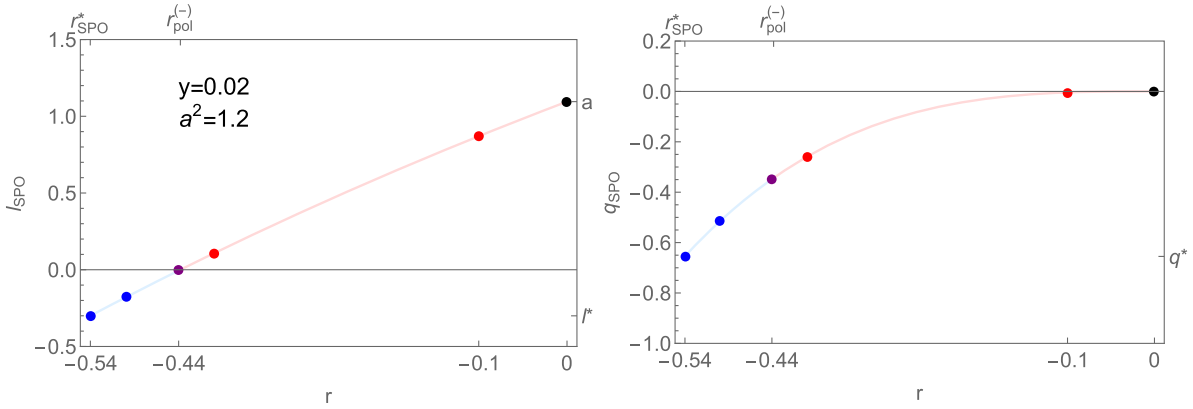

FIG. 22. Dependence of the motion constants ℓ_{SPO}, q_{SPO} of the SPO photons at the negative radii on the radius r_{SPO} of the corresponding orbit for the spacetime considered above. The different sections of the curves are color coded according to the orbital type in the color style as in Figs. 18 and 20. The colored dots highlight the radial coordinates of the selected SPOs considered in Fig. 18.

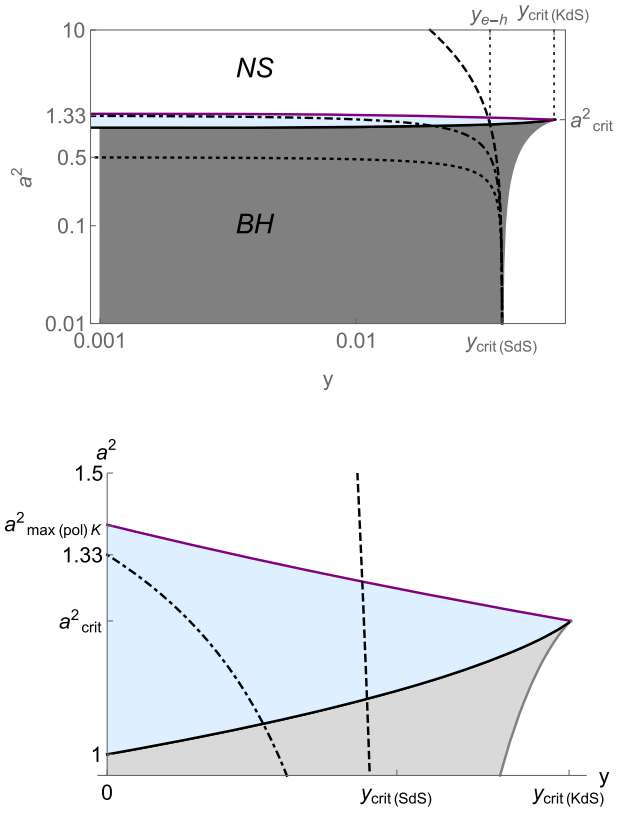

FIG. 23. Behavior of the curves $a^2_{I-II}(y)$ (black dotted), $a^2_{erg-pol}(y)$ (black dot-dashed) and $a^2_{erg-s}(y)$ in comparison to the curves $a^2_{min(h)}(y)$ (full gray) and $a^2_{max(h)}(y)$ (full black) that separates the cosmological parameters corresponding to the KdS BH spacetimes (gray region) from the cosmological parameters corresponding to the KdS NS spacetimes (white region). The purple curve is the function $a^2_{max(pol)}(y)$, determining the boundary of spacetimes, where the polar SPOs exist (blue region).

are important for the appearance of astrophysical phenomena in the vicinity of BHs and NSs, in particular for determining the shape and extension of the shadow. We give a complete classification of the KdS spacetime due to the photon motion in the region of $r > 0$, but in the following we concentrate on the KdS NS spacetimes with parameters that do not contradict the astrophysical constraints. It must be emphasized that this is the first time that we have presented a detailed discussion of the photons reaching the region of $r < 0$.

In the KdS BH spacetimes, there are both corotating and counterrotating ECPOs, located at radii r^+_{ph}, r^-_{ph} respectively, which in the equatorial plane delimit the range of SPOs, which can be both prograde or retrograde, but unstable. In all classes of the KdS NS spacetimes, only one unstable counterrotating ECPO exists at $r = r^-_{ph}$. Furthermore, in contrast to the BH spacetimes, there exist stable SPOs in all the NS spacetimes. In each class of the KdS NS spacetimes there together retrograde SPOs, which are completely immersed in the ergoregion. It was shown in [110] that photons on such SPOs have positive locally measured energy only if they have negative covariant energy, $E < 0$. Such negative covariant energy SPOs also exist in the Class III KdS BH spacetimes (see below), i.e., in BH spacetimes with RRB.

In all previous studies of KdS spacetimes, we considered only the $r > 0$ region. Here we have for the first time discussed the region of negative radii, although we have not considered the region of causal disturbances, which we intend to address in a future study. From our analysis, we can conclude that the region of negative radii remains qualitatively the same for all types of KdS spacetimes and therefore does not affect the classification of the spacetimes as proposed in [110]. The classification of the KdS spacetimes according to the properties of their geodesic structure at $r > 0$ can be summarized as follows [110]:

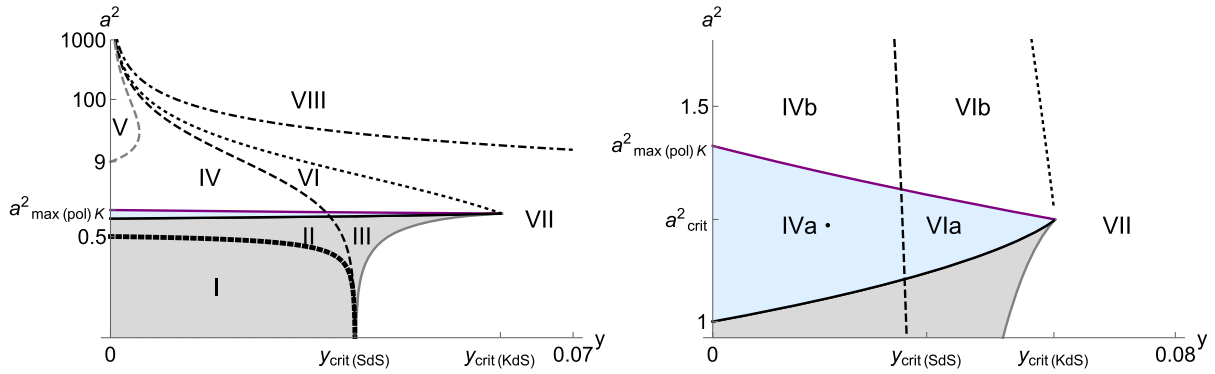

FIG. 24. Classification of the KdS BH and NS spacetimes in the parameter space $(a^2 - y)$ according to the properties of the horizons, the ergospheres, and the properties of the null geodesics. Here detailed character of SPOs is reflected, including their number, stability, orientation, relative position to the ergosphere, and existence of the polar SPOs. In order to clearly display distant regions of the parameter plane, the vertical axis in the left figure is in logarithmic scale, so that the individual regions, according to the induced classification first proposed in [110], are vertically compressed. The figure on the right shows in detail the blue region, where the black dot corresponds to the selected KdS NS spacetime discussed in this article, with parameters $a^2 = 1.2, y = 0.02$ belonging to the astrophysically relevant region, but with values of the parameters large enough to enable a clear demonstration of all the relevant effects—in this region the NS spacetimes allow existence of the polar SPOs. The significance of each of the individual classes is described in the text of the Sec. III F.

Class I: BH spacetimes with DRB of radial photon motion; the region of the SPOs, all of which are unstable, intersects the equatorial plane between the radii $r = r^+_{\rm ph}$ of the inner ECPO, which are corotating, and the radii $r = r^-_{\rm ph}$ of the outer ECPO, which are counter-rotating. The prograde and retrograde SPOs are separated by the polar SPOs at radii $r = r_{\rm pol}$. The characteristic radii are related by the inequalities $0 < r_i < r_o < r^+_{\rm erg} < r^+_{\rm ph} < r_{\rm pol} < r^-_{\rm ph} < r_s < r^-_{\rm erg} < r_c$. The structure of the outer BH and cosmological horizon, the inner and outer ergosurface and the static radius are shown in Fig. 5(a).

Class II: BH spacetimes with the same properties as in the case of Class I, but now the region of the SPOs partially extends into the BH ergoregion. The corresponding inequalities together $0 < r_i < r_o < r^+_{\rm ph} < r^+_{\rm erg} < r_{\rm pol} < r^-_{\rm ph} < r_s < r^-_{\rm erg} < r_c$.

Class III: BH spacetimes with RRB. The SPOs completely interfere with the ergoregion in the equatorial plane, since it extends over the entire stationary region in the range $r_o < r < r_c$, as shown in Fig. 5(c). The characteristic radii are related by the inequalities $0 < r_i < r_o < r^+_{\rm ph} < r_{\rm pol} < r^-_{\rm ph} < r_c$. The borderline case, corresponding to the transition between classes II and III, is shown in Fig. 5(b).

Class IVa: NS spacetimes with DRB, an unstable counter-rotatimg ECPO at $r = r^-_{\rm ph}$ and two polar SPOs, the inner one at $r = r^+_{\rm pol}$ being stable, the outer one at $r = r^-_{\rm pol}$ being unstable. The polar SPOs separate regions of SPOs with different orientations; the prograde SPOs are enclosed between the two polar SPOs at $r = r^\pm_{\rm pol}$; for $r^+_{\rm pol} < r < r_{\rm ms}$ they are stable, for $r_{\rm ms} < r < r^-_{\rm pol}$ they are unstable, where $r_{\rm ms}$ stands for the marginally stable SPO; the stable retrograde SPOs are located in the region $0 < r < r^+_{\rm pol}$, the unstable retrograde SPOs are located in the region $r^-_{\rm pol} < r < r^-_{\rm ph}$. There are two separate ergoregions, the inner toroidal one touching the ring singularity, that partially overlaps the area of the SPOs of both types of orientation and stability, and the outer cosmological ergoregion touching the cosmological horizon; the ergosurfaces are shown in Fig. 5(d). The characteristic radii are related by the inequalities $0 < r^+_{\rm pol} < r_{\rm ms} < r^-_{\rm pol} < r^+_{\rm erg} < r^-_{\rm ph} < r^-_{\rm erg} < r_c$.

Class IVb: NS spacetimes that differ from the Class IVa by the absence of the polar SPOs. There are only counter-rotating SPOs, the stable ones being in the range $0 < r < r_{\rm ms}$, the unstable ones are in the range $r_{\rm ms} < r^-_{\rm ph}$. The inner ergosphere partially covers both stable and unstable SPOs. The characteristic radii are related by the inequalities $0 < r_{\rm ms} < r^+_{\rm erg} < r^-_{\rm ph} < r^-_{\rm erg} < r_c$.

Class V: NS spacetimes with the same properties as in the case of Class IVb, but now the inner ergosphere partially covers the stable SPOs

only. The relationships between the characteristic radii are given by the inequalities $0 < r^{+}_{\mathrm{erg}} < r_{\mathrm{ms}} < r^{-}_{\mathrm{ph}} < r^{-}_{\mathrm{erg}} < r_c$.

Class VIa: NS spacetimes with RRB and the same structure of the SPOs as in the Class IVa. The presence of the RRB is related to the modified structure of the ergoregion, depicted in Fig. 5(f). The ergoregion partially covers the area of the SPOs of both types of orientation and stability. The characteristic radii are ordered as follows: $0 < r^{+}_{\mathrm{pol}} < r_{\mathrm{ms}} < r^{-}_{\mathrm{pol}} < r^{-}_{\mathrm{ph}} < r_c$. The borderline case, corresponding to the transition between classes IV and VI, is illustrated in Fig. 5(e).

Class VIb: NS spacetimes with RRB and the same structure of the SPOs as in the Class IVb. The presence of the RRB is again related to the modified structure of the ergoregion, as shown in Fig. 5(f). The characteristic radii are ordered as follows: $0 < r_{\mathrm{ms}} < r^{-}_{\mathrm{ph}} < r_c$.

Class VII: NS spacetimes with RRB and the same structure of the SPOs as in the Class VIb, but now the SPOs are completely immersed in the ergosphere. As a consequence, there are only SPOs with negative covariant energy $E < 0$. The shape of the ergosurface is shown in Fig. 5(f) and approaches the shape shown in Fig. 5(g) as $a^2 y \to 1$.

Class VIII: NS spacetimes with RRB and the same structure of the SPOs as in the Class VII, but with different behavior of the latitudinal photon motion, allowing, unlike all previous cases, the vortical motion of retrograde photons with negative covariant energy, $E < 0$. The ergosurface is ellipsoidal in shape as shown in Fig. 5(h).

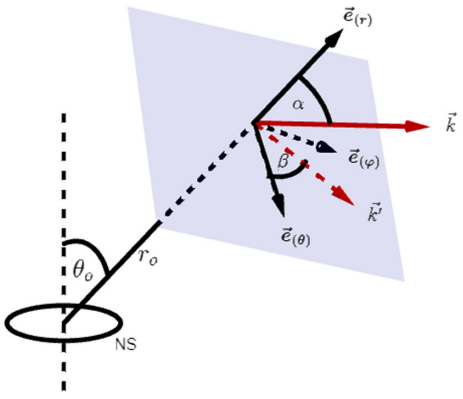

FIG. 25. Definition of the locally measured directional angles α, β. The small circle represents the naked singularity, the dashed vertical line is its spin axis. The observer's radial and latitudinal coordinates are r_o, θ_o. The arrows labeled $\vec{e}_{(r)}, \vec{e}_{(\theta)}, \vec{e}_{(\phi)}$ illustrate the local radial, latitudinal and azimuthal orthonormal basis vectors, respectively; the red arrow marked $\vec{k}$ depicts a photon 3-momentum, the red dashed arrow represents its projection into the local (θ, ϕ) plane.

The study of the SPOs, polar SPOs and their stability is extended to the region of negative radii, $r < 0$, in Sec. III D 2. For the reasons of astrophysical relevance, we will consider in the following the KdS NS spacetimes with $a^2 y < 1$, similarly to the study realized for KdS BH spacetimes in [97])—we restrict the following investigations to the KdS NS spacetimes of the Class IVa as they correspond to the astrophysically relevant spacetimes implied by the magnitude of the relic cosmological constant ($\Lambda \sim 10^{-52}$ m^{-2}) indicated by the recent cosmological tests [94], and the observed high masses of central objects in the active galactic nuclei ($M \sim 10^{10} M_{\odot}$), or those assumed to be the largest gravitationally bounded systems in the dark matter halos of large galaxies or their clusters ($M \sim 10^{15} M_{\odot}$), for details see e.g. [91,93,95].

IV. NS SHADOWS IN LOCALLY NONROTATING FRAMES

We have analyzed special classes of null geodesics of the KdS NS spacetimes relevant the for construction of their shadow as seen by distant static observers, that could be well represented by observers located in the locally nonrotating reference frames near the static radius of the KdS spacetimes; such observers are similar to static observers at large distances in asymptotically flat spacetimes [88,91,107]. The special geodesic classes include null geodesics terminating in the ring singularity, and null geodesics entering the region of negative radii; namely, null geodesics remaining on fixed latitude, and the null geodesics corresponding to the spherical photon orbits (SPOs) at negative radii. Of standard relevance are the photons that wind up onto the SPOs at positive radii.

The shadow of a BH (compact object) was introduced in [18] as an apparent shape of the dark region seen by a distant observer in his celestial sphere, created by the BH located between the observer and an illumination source with an angular size exceeding that of the BH. This definition can also be useful in more complex situations, such as the appearance of a Keplerian disk or radiating torus orbiting the BH (compact object); see [17,54]

The shadows (silhouettes) of a compact object on a bright background, constructed in a local reference frame of an axially symmetric stationary spacetime, are related to the LECs and the complementary LCCs. If the reference frame is considered as a source of radiation, the LECs (LCCs) are defined as complementary parts of the celestial sphere of isotropically radiating source located in the field of a compact object (BH or NS), corresponding to photons escaping to infinity (captured by the compact object) [54]. The method of determining the shadow by using the LECs is especially useful when we are interested in determining

the BH or NS shadow for observers orbiting in their close vicinity, where complex radiating structures such as accretion disks can exist.

Here we concentrate on the construction of the shadow with relation to distant observers—in such a case, the shadow as seen on the observer's sky can be constructed directly by inverting the LCC of the photons emitted by the source, located at the same position, about the celestial projection of the symmetry axis of the spacetime. The boundary between the LEC and LCC at a given source is determined by the parameters of the photons corresponding to the SPOs. This feature is explained in the comment to Fig. 26, demonstrating the construction of the shadow.

The shadows in the observer's sky are determined by the system of the angular coordinates representing the photon's directional angles. The angular coordinates are related to the components of the photon 3-momentum measured in the observer's frame that are generally governed by the photon motion constants [97].

Here we present the resulting shadows of the KdS NSs for a representative spacetime with parameters $a^2 = 1.2$, $y = 0.02$, corresponding to the class IVa of the KdS NS spacetimes with its structure expected in the realistic universe models with relic cosmological constant implied by cosmic observations of the accelerated expansion and the observed magnitude of the mass of cosmic objects. The parameter y is chosen high for the illustrative purposes; in situations that are realistic from an astrophysical point of view, the parameter $y \ll 1$, but the qualitative features of the shadow remain unchanged, only the scales are modified.

In construction of the shadows we apply the method of establishing the boundary between the LEC and the LCC using the observers related to the LNRFs located near the static radius in the KdS spacetime, that are qualitatively close to the static distant observers in asymptotically flat spacetimes [107]. For more complex situations, see the discussion in [54,97].

A. Directional angles of photons in the LNRFs

The directional angles (α, β) (see Fig. 25) of a photon are related to the locally measured frame components $k^{(a)}$ of the photon 4-momentum by the standard definitions ([54])

$$\cos\alpha = k^{(r)}/k^{(t)}, \tag{164}$$

$$\sin\alpha\cos\beta = k^{(\theta)}/k^{(t)}, \tag{165}$$

$$\sin\alpha\sin\beta = k^{(\phi)}/k^{(t)}. \tag{166}$$

In the relations (164)–(166) we can put $k^{(t)} = 1$ without loss of generality.

Therefore, the Eqs. (54)–(57), (60), (61), and (164)–(166) give the correspondence between the pair of directional angles (α, β) and the pair of motion constants (X, q). To get an insight into the notion of the motion constants, we present the corresponding $(X - q)$ plane together with each of the constructed shadows.

Note that there is a third directional angle γ used in the literature (e.g. [138]), defined by the relation

$$\cos\gamma = k^{(\phi)}/k^{(t)} \tag{167}$$

that can replace any of the angles α, β. For our purposes, however, the pair (α, β) is a more appropriate choice.

B. Construction of the KdS NS shadows and relation to the LECs (LCCs)

the construction of the shadows of the KdS NS related to local observers, by using the LECs (and related LCCs) of these observers, requires a simple redefinition of the directional angles that should be related to photons reaching these observers, not to photons emitted by them. In Fig. 26 the construction of the shadows is explained and new coordinates $\tilde{\alpha}, \tilde{\beta}$ characterizing the shadows are introduced. The basic step is the construction of the shadow boundary by finding the directional angles related to the photons reaching the SPOs. Using Fig. 26 and its comment, the directional angles of the shadow boundary can be obtained by the following procedure:

(1) For given radial and latitudinal coordinates r_o, θ_o of the observer, we determine the motion constants $X_{\rm SPO}, q_{\rm SPO}$ which, in the $(X - q)$ parameter plane, represent the so-called critical locus, for which the photon emitted from the observer's position reaches some unstable SPO with radius $r_{\rm SPO}$.

(2) From the relations Eqs. (32)–(35), (54)–(57), (60), and (61) we determine the locally measured 4-momentum components $k^{(a)}$ of this photon escaping towards the SPO. In the case of the radial component $k^{(r)}$ we get

$$k^{(r)} = \omega^{(r)}[\mathbf{k}] = \omega^{(r)}_r k^r, \tag{168}$$

where we must correctly choose the sign for the radial component k^r determined from the Eq. (54). Apparently we have to take $k^r = s_r|k^r|$, where $s_r = \mathrm{sign}(r_{\rm SPO} - r_o)$.

(3) According to the relations (164)–(166) we compute directional angles $\tilde{\alpha}$, $\tilde{\beta}$ corresponding to virtual photons with locally measured components $(-k^{(r)}, \pm k^{(\theta)}, -k^{(\phi)})$. These angles then correspond to two points of the shadow, which are placed symmetrically with respect to the axis perpendicular to the projection of the spin axis, (see the points L', M' in Fig. 26).

In the illustrations of the constructed shadows, the angle $\tilde{\alpha} \in \langle 0; \pi\rangle$ is used as a radial coordinate measured in radians in the polar plots, while $\tilde{\beta} \in \langle 0°; 360°\rangle$ is operated as the polar coordinate measured in degrees.

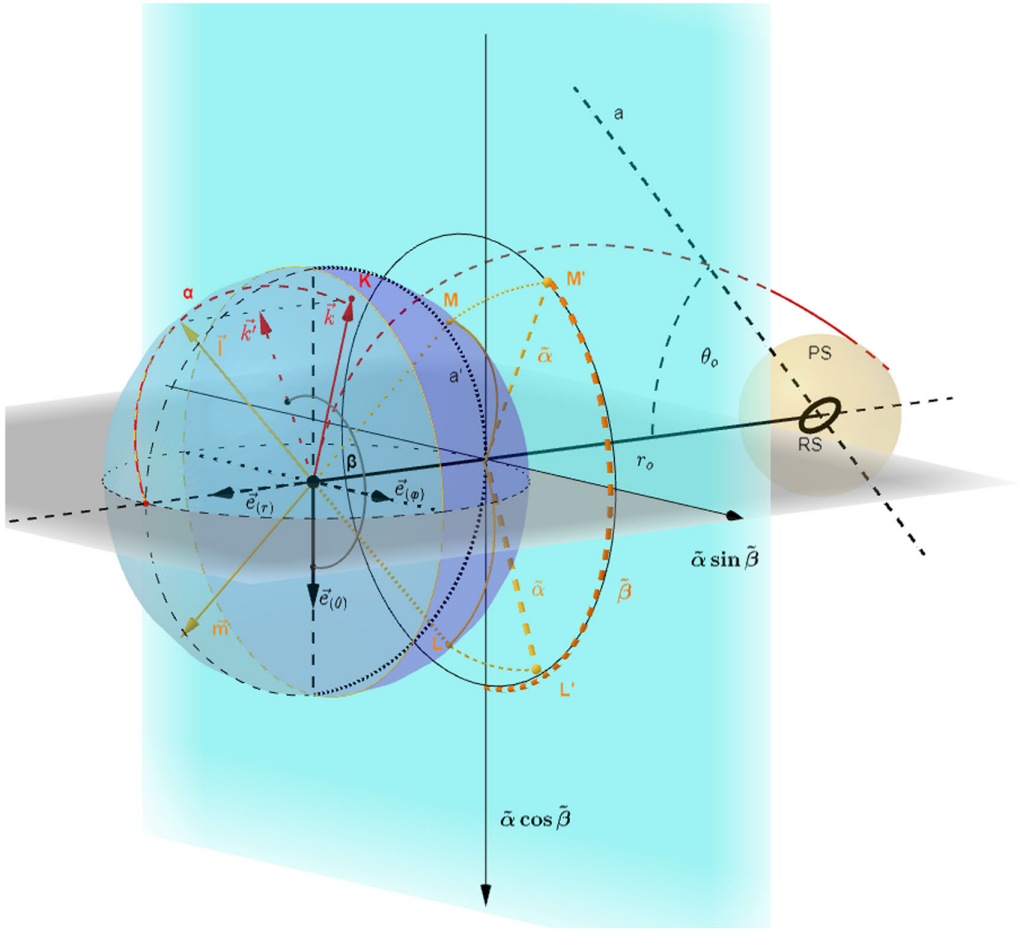

FIG. 26. Construction of the shadow of a KdS NS on a local observer's sky with the use of the concept of the LEC and the complementary LCC of the observer; the boundary of these complementary cones is determined by the motion constants of the photons related to the SPOs. The observer (black dot) located at radial distance r_o from the center of the ring singularity (RS) represented by the small black circle, at latitudinal coordinate θ_o, is endowed with a local tetrad of orthonormal basis vectors $\vec{e}_{(t)}$, $\vec{e}_{(r)}$, $\vec{e}_{(\theta)}$, $\vec{e}_{(\phi)}$. Let $\vec{k}$ be a 3-momentum of a photon emitted from the observer location (red arrow) with locally measured radial, latitudinal and azimuthal components $(k^{(r)}, k^{(\theta)}, k^{(\phi)})$, respectively, defining the directional angles α, β on the observer's sky according to the relations (164)–(166). The photon 3-momentum components correspond to motion constants $X_{\rm SPO}$, $q_{\rm SPO}$ tuned so that the photons eventually wind up on some SPO (yellow sphere). The vector $\overrightarrow{k'}$ is projection of the vector $\vec{k}$ into the local (θ, ϕ)-plane perpendicular to $\vec{e}_{(r)}$. The apparent point K (red point) on the observer's celestial sphere (consisting of two half-spheres of different shades of blue) in the direction of the 3-vector $\vec{k}$ defines a point of the boundary of the local LEC (LCC). Two 3-vectors, $\vec{l} = (-k^{(r)}, k^{(\theta)}, k^{(\phi)})$, $\vec{m} = (-k^{(r)}, -k^{(\theta)}, k^{(\phi)})$, correspond to virtual photons with the same motion constants $X_{\rm SPO}$, $q_{\rm SPO}$, that cannot reach the observer from a distant bright background since they must be trapped on the photon sphere. Hence the directions of their arrival define two apparent points L, M on the observer's celestial sphere—the observer recognizes them as points constituting the boundary of the KdS NS shadow, appearing as a circlelike curve or an arc (see figures below). Of course, this curve itself is not observable, but is lined with images of stars in the background whose photons, with motion constants slightly different from $X_{\rm SPO}$, $q_{\rm SPO}$, had to orbit near the photon sphere many times before finally reaching the observer. The points K, M are placed symmetrically with respect to the celestial projection a' (black dotted curve) of the spin axis a (black dashed line), the points L, M are placed symmetrically with respect to the local (r, ϕ)–plane perpendicular to $\vec{e}_{(\theta)}$. It is apparent from the symmetry that the same construction would even apply to a photon radiated in the opposite latitudinal direction. Consequently, the LCCs and the shadows (silhouettes) are symmetric with respect to the projection a' of the spin axis. We represent the celestial sphere in a two-dimensional plane defined by two mutually perpendicular axes; the vertical one corresponds to the spin axis a, the intersection of these axes corresponds to the image of a point lying on the celestial sphere in the direction towards the center of the RS. The angular displacement of a particular celestial point, e.g. L, from the direction to the center is used as the radial coordinate $\tilde{\alpha}$ of its image L' in this plane. It can be calculated from the relation (164) for a photon with 3-momentum $\vec{l}$ (see the yellow dashed arc overlapping the red dashed arc representing the angle α), hence $\tilde{\alpha} = \pi - \alpha$. The coordinate $\tilde{\beta}$ is introduced as the angular coordinate of a particular image. Here the coordinate $\tilde{\beta}$ of M' can be calculated from the relations (165) and (166) for the 3-vector $-\vec{m}$. In summary, the coordinates $\tilde{\alpha}, \tilde{\beta}$ of the point L'/M' correspond to the directional angles of a virtual photon with locally measured components $(-k^{(r)}, \mp k^{(\theta)}, -k^{(\phi)})$.

The shape of the KdS NS shadow depends on the latitudinal and radial coordinates of the observer's position. We present the construction of the shadows for some appropriately chosen latitudinal positions, namely the limiting cases on the spin axis $\theta_o = 0°$, and in the equatorial plane $\theta_o = 90°$; as an intermediate position we chose the latitude $\theta_o = 60°$. In order to clearly display a continuous progression of the shape of the shadows as the latitude increases, some specific latitudes are used in addition to those given above. The radial coordinate of the observer is chosen at the static radius $r_s = 3.68$. We used this radial location as it is the most convenient local approximation to the flat Kerr spacetime [107,108].

If we do not expect any source of radiation in the $r < 0$ region of the KdS NS spacetime, the light rays escaping to the secondary infinity $r \to -\infty$ will cause an observer at the static radius to see a dark spot in the corresponding direction. This dark region, representing the shadow, is shown in Figs. 27–29 in purple color, as well as in the accompanying figures of the corresponding $(X - q)$ planes. Accordingly, the light rays that wind around the SPOs at both positive or negative radii are plotted as an orange curve, as they correspond to the critical locus in the $(X - q)$-plane depicted in the same color. The light rays with a radial turning point in the region $r < 0$ and returning to $r > 0$, as illustrated in Fig. 9, make the corresponding region visible. This region is depicted in lighter purple. In addition, the characteristic directions corresponding to the PNC and the $\theta^* = \text{const}$ photons are indicated by dots. The meaning of the other dots follows from the plots of the $(X - q)$-planes in Figs. 27–29.

V. SHADOWS IN RADIALLY ESCAPING FRAMES

Of special interest is the appearance of the KdS NS shadow for observers leaving the static $\Delta_r > 0$ region of the spacetime, located near (or at) the cosmological horizon of the spacetime. Such observers (frames) are strongly influenced by the cosmic repulsion of the spacetime; the LNRFs (and the ZAMOs) must be kept on a fixed radius by forces that increase without limit as the radius approaches the cosmological horizon (or the BH horizon), and surely cannot be considered as physically realistic observers in these situations. In the vicinity of the cosmological horizon, the natural choice of a physically realistic observer is an observer moving freely under the influence of the cosmic repulsion, in particular an observer following radially escaping geodesic [97]. Since the frame dragging persists even up to the cosmological horizon in the KdS spacetimes, the observer moves purely radially with respect to the LNRF, which currently orbits at radius of the observer's position. We can naturally assume that the radially escaping observer starts its motion from the rest state at $r = 0$ (near this radius in the equatorial plane) or at the static radius, where the effective potential of the radial motion demonstrates an unstable equilibrium point [88]; for relations to the Einstein-Straus vacuola model (see [89]).

A. Radially escaping geodesic observer

The locally measured 3-velocity components of a test particle (observer) in a given LNRF are generally determined by the relations

$$v^{(j)} = \frac{u^{(j)}}{u^{(t)}} = \frac{\omega^{(j)}_\mu u^\mu}{\omega^{(t)}_\nu u^\nu}, \qquad j = r, \theta, \phi. \tag{169}$$

Here $\omega^{(j)}_\mu$ are the differential 1-forms given by the relations (32)–(35) and $u^\mu = \frac{\mathrm{d}x^\mu}{\mathrm{d}\tau}$ are the coordinate components of particle's four-velocity given by the Carter equations (40)–(43), where we have replaced the affine parameter λ by the particle proper time τ, i.e., we put $\lambda = \tau/m$.

In order to keep the component $v^{(r)}$ in the LNRFs as the only nonzero 3-velocity component for geodesic motion along any latitude θ_0, the particle motion constants Φ, E, Q have to be restricted to special values [97]. The requirement $v^{(\phi)} = 0$ implies that

$$\Phi = 0. \tag{170}$$

The requirement $v^{(\theta)} = 0$ implies

$$Q = -a^4 y m^2 \cos^4\theta_0. \tag{171}$$

The requirement of stable motion along the latitude $\theta_0 = \text{const}$ implies

$$E = \frac{\Delta_{\theta_0}}{I\sqrt{I}} m. \tag{172}$$

It is explicitly demonstrated in [97] that particles with this particular choice of the motion constants follow purely radial trajectories in the LNRFs at the fixed latitude θ_0, having no turning points in the region between $r = 0$ and the cosmological horizon r_c.

The radial velocity $v^{(r)}$ for the outward directed motion takes the form

$$v^{(r)} = \sqrt{1 - \frac{I\rho^2\Delta_r}{A\Delta_\theta}}, \tag{173}$$

while it takes the opposite sign for the inward motion. During this purely radial motion relative to the LNRFs the particle persists on the constant latitude θ_0, being stable against the perturbations in the latitudinal directions, as shown in [97]. Such radially escaping (falling) particles thus generalize the shell of radially escaping (falling) particles that are falling freely from infinity onto a Kerr naked singularity [117] (for the black hole case see [139]) in all the

The naked singularity shadows for the KdS NS spacetime with parameters $y = 0.02$, $a^2 = 1.2$, for observers at static radius $r_o = r_s = 3.68 > r_{ph}^-$

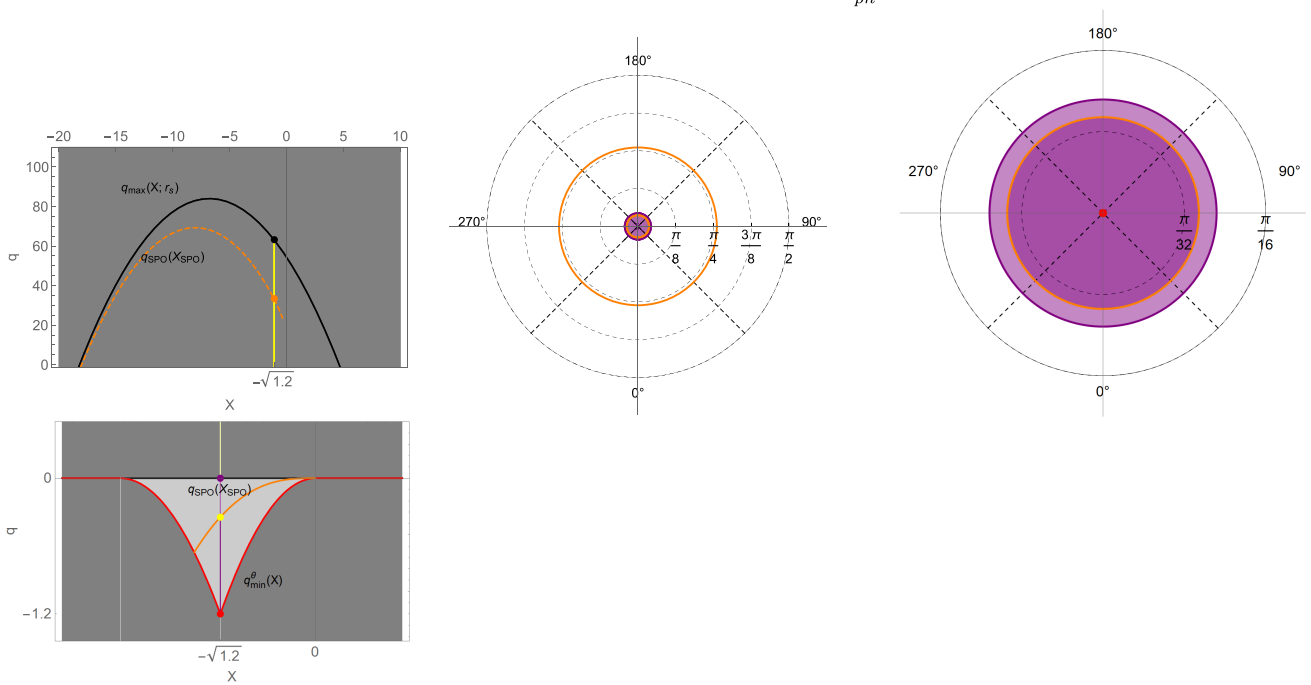

(a) $\theta_o = 0°$

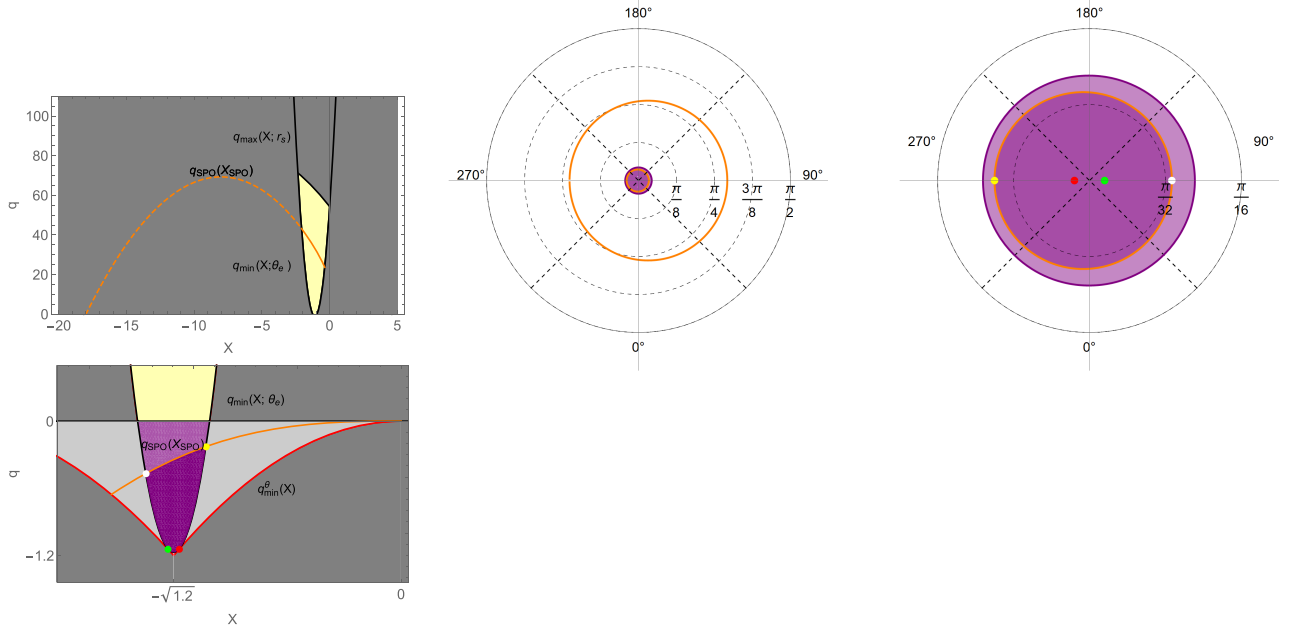

(b) $\theta_o = \theta_{max(circ)} = 8.29°$

FIG. 27. Shadows for small observer inclination angles θ_o. The $(X - q)$ parameter plane (left column) and the corresponding NS shadows (middle column) and the detail of the dark spot (right column) for the observer latitude θ_o corresponding to the position on the spin axis (a), and the marginal angle $\theta_{\text{max(circ)}}$ for which a circle-shaped curve (outer orange curve) appears corresponding to photons winding up the unstable SPOs at $r > 0$ occurs (b). This circle exists in spacetimes with the polar SPOs for observer's latitude less than the critical value, $\theta_o \leq \theta_{\text{max(circ)}}$. The dark spot (dark purple area) is delimited by photons winding up the unstable SPOs at $r < 0$ (inner orange curve). The photons with turning points at $r < 0$ (light purple area) are delimited by photons that hit the ring singularity (purple ellipse). Colored dots indicate the special photons; the PNC photon (red), the θ^*-photon (green), and the photons delimiting the angular diameter of the dark spot (yellow and white). The "polar" coordinate of the shadows is measured in radians and corresponds to the celestial coordinate $\tilde{\alpha}$, while the angular coordinate is measured in degrees and corresponds to the celestial coordinate $\tilde{\beta}$.

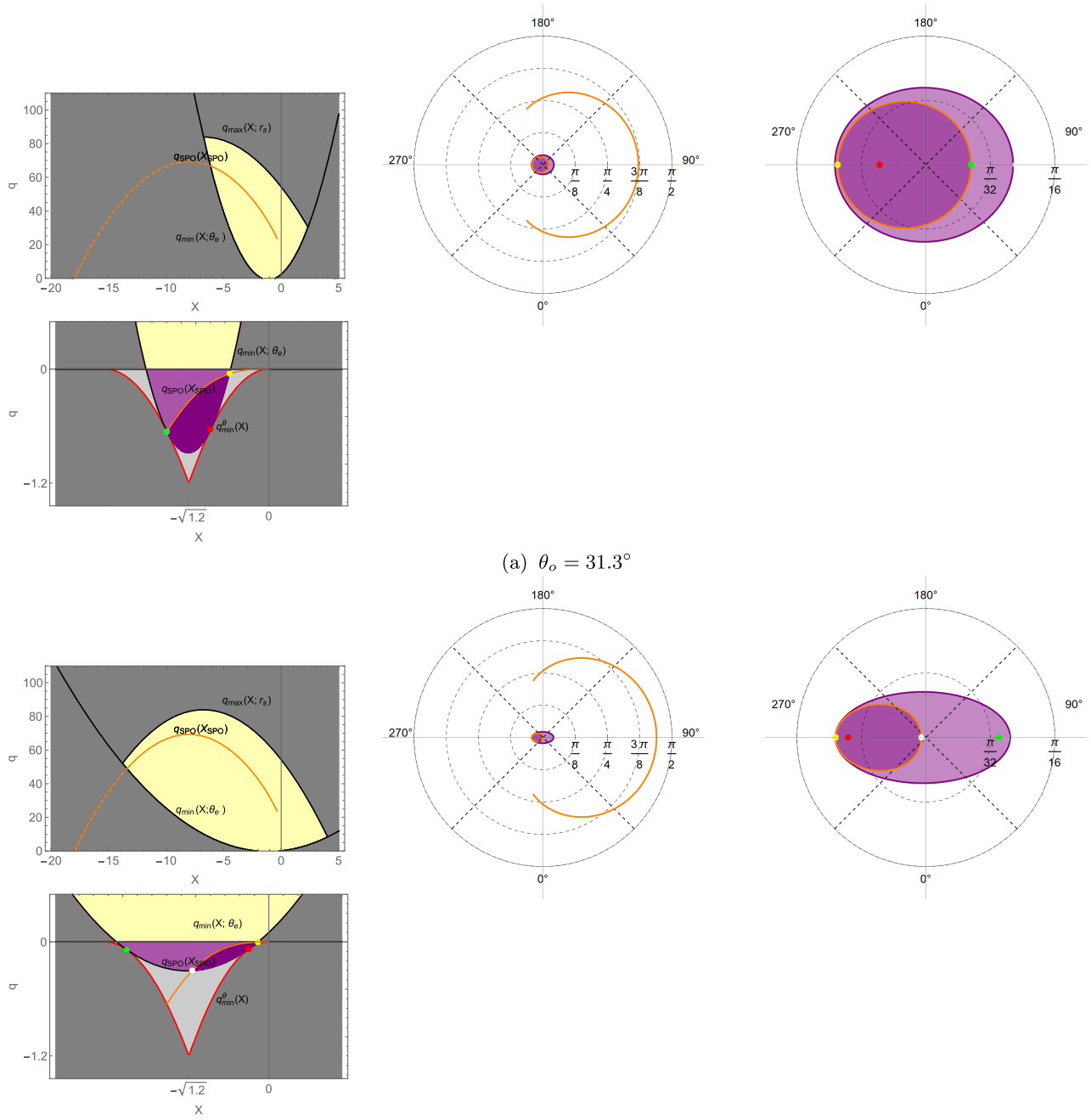

(a) $\theta_o = 31.3°$

(b) $\theta_o = 60°$

FIG. 28. Shadows for mediate inclination angles of the observer. Continuation of the preceding figure for θ_o corresponding to the case when the θ^* photon winds up the lowest SPO of the given spacetime at negative radii, i.e., the unstable counter-rotating off-equatorial circular orbit at $r^*_{\rm SPO}$, thus defining the angular size of the dark spot (a), and when it is repelled in the region of $r < 0$ (b). In both cases the latitude of the observer $\theta_o > \theta_{\rm max(circ)}$, and thus an arc has appeared.

cases the particles move purely radially relative to the LNRFs.

According to Eq. (172), the covariant energy of the radially escaping particles is in the range of

$$\frac{m}{I\sqrt{I}} \leq E \leq \frac{m}{\sqrt{I}}, \tag{174}$$

where the lower limit corresponds to the motion in the equatorial plane, with the motion constant $Q = 0$, while the upper limit corresponds to the motion along the spin axis, with the motion constant $Q = -a^4 y m^2$. It was also shown in [97] that these energies do not allow radial turning point at any radius $0 < r \leq r_c$, i.e., the radial velocity is always nonzero at any radial and latitudinal coordinate; the motion

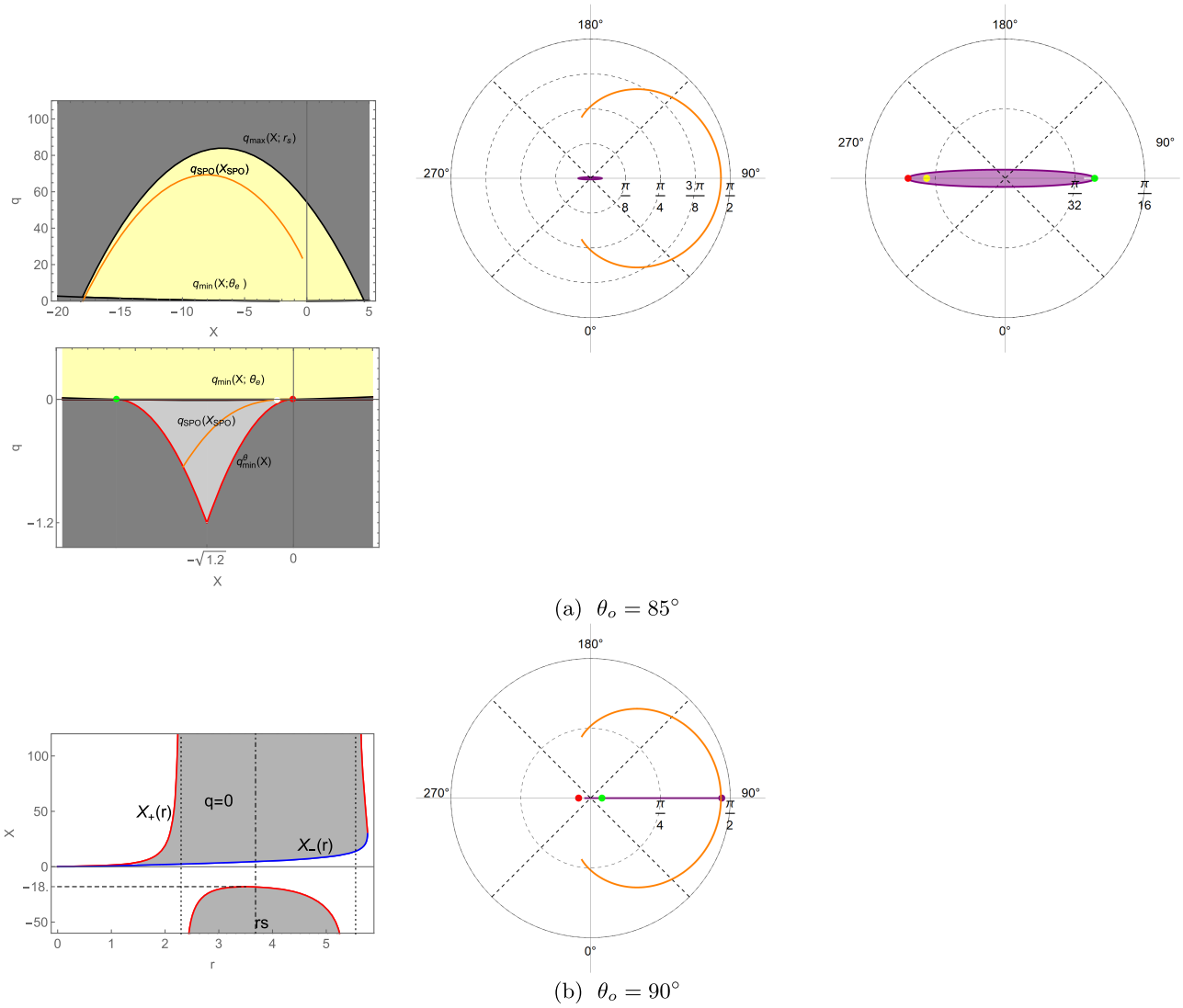

(a) $\theta_o = 85°$

(b) $\theta_o = 90°$

FIG. 29. Shadows for very large inclination angles of the observer. Continuation of Fig. 28 corresponding to the case of $\theta_o \to 90°$ when the PNC photon and the θ^*-photon delimit the angular size of the RS shadow (a). The case (b) is exceptional in the sense that it corresponds to the observer's position in the equatorial plane, when the limits of the parameter X are given by the effective potentials $X_{\pm}(r)$ (left figure). Since the radial position of the observer is on the static radius $r_s > r^{-}_{\rm ph}$, the limits are $X_{\rm ph-} \le X \le 0$, where $X_{\rm ph-} = -18.0$ is the impact parameter of the photon on the equatorial circular photon orbit (purple dot). The RS shadow is represented by the purple abscissa.

is fixed in the outward (inward) direction. Here we will focus on the outward directed motion, so we are considering positive values of the radial velocity.

The minimum radial velocity at any $\theta_o \neq \pi/2$ corresponds to the location at $r = 0$ and reads

$$v^{(r)}(r=0) = \frac{\cos^2\theta_0 a^2 y}{1+\cos^2\theta_0 a^2 y}. \tag{175}$$

Of course, for $\theta_0 = \pi/2$ the formula (175) gives zero, but at $r = 0$ and $\theta_0 = \pi/2$ there is a ring singularity, and analyzing Eq. (173) gives

$$\lim_{r\to 0^+} v^{(r)} = 1. \tag{176}$$

The behavior of the radial velocities depending on the radial coordinate is shown in Fig. 30 for some selected latitudes θ_0.

B. Radially escaping reference frame

In the following we consider a local reference frame that moves outwards purely radially with respect to the LNRF, currently orbiting at the actual particle (r, θ) coordinates, with the velocity given by the relation (173). We call the system introduced in this way the radially escaping frame

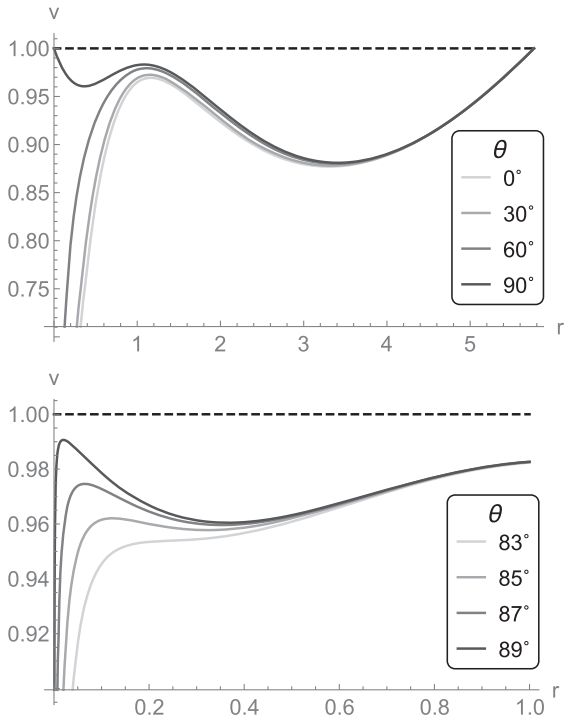

FIG. 30. Velocity of a test particle performing a purely radial motion with respect to the LNRFs currently orbiting at the particle's position with coordinates (r_o, θ_o). The KdS NS spacetime parameters are again $a^2 = 1.2$, $y = 0.02$, the cosmological radius is at $r_c = 5.77$. The motion is stably confined to any constant latitude θ_o, and the velocity is nonzero at any radius $r > 0$. Note that the curves are not drawn down to the intersections with the vertical axis, in order to clearly display the subtle differences between them at their higher values. The local minimum about the radius $r = 0.4$ exists for θ_0 exceeding some critical value, here $\theta_{0(cr)} \sim 83^{\circ}$, that depends generally on the spacetime parameters.

(REF). The 4-momentum $\mathbf{k}$ of a photon can be expressed in this system as

$$\mathbf{k} = k^{(\hat{a})}\mathbf{e}_{(\hat{a})}, \tag{177}$$

where $\mathbf{e}_{(\hat{a})}$, $\hat{a} = \hat{r}, \hat{\theta}, \hat{\phi}, \hat{t}$, is the tetrad of the REF basis 4-vectors, related to the LNRF tetrad $\mathbf{e}_b$, $b = t, r, \theta, \phi$, by transformation equations

$$\mathbf{e}_{(\hat{a})} = \Lambda_{(\hat{a})}{}^{(b)}\mathbf{e}_{(b)}, \tag{178}$$

where $\Lambda_{(\hat{a})}{}^{(b)}$ are the elements of the Lorentz transformation matrix

$$\Lambda_{(\hat{a})}{}^{(b)} = \begin{pmatrix} \gamma & \gamma v & 0 & 0 \\ \gamma v & \gamma & 0 & 0 \\ 0 & 0 & 1 & 0 \\ 0 & 0 & 0 & 1 \end{pmatrix}, \tag{179}$$

with

$$\gamma = \frac{1}{\sqrt{1 - v^2}} \tag{180}$$

being the Lorentz factor. Here and beyond, for brevity, we use the notation v for the relative speed of the LNRF and REF systems, instead of $v^{(r)}$. to find the locally measured 4-momentum components $k^{(\hat{a})}$ of the photon in the REF, we use the local tetrad of the REF differential 1-forms $\omega^{(\hat{a})}$ introduced by the relation

$$\omega^{(\hat{a})}[\mathbf{e}_{(\hat{b})}] = \delta^{(\hat{a})}_{(\hat{b})}, \tag{181}$$

that are related to the LNRF differential 1-forms by the standard local Lorentz transformation

$$\omega^{(\hat{a})} = \Lambda^{(\hat{a})}_{(b)}\omega^{(b)}, \tag{182}$$

where $\Lambda^{(\hat{a})}_{(b)}$ are the elements of the transformation matrix inverse to $\Lambda^{(b)}_{(\hat{a})}$, i.e.,

$$\Lambda^{(\hat{a})}{}_{(b)} = \begin{pmatrix} \gamma & -\gamma v & 0 & 0 \\ -\gamma v & \gamma & 0 & 0 \\ 0 & 0 & 1 & 0 \\ 0 & 0 & 0 & 1 \end{pmatrix}. \tag{183}$$

The locally measured photon's 4-momentum components are then given by

$$k^{(\hat{a})} = \omega^{(\hat{a})}[\mathbf{k}] = \omega^{(\hat{a})}_{\mu}k^{\mu} = \Lambda^{(\hat{a})}{}_{(b)}\omega^{(b)}_{\mu}k^{\mu} = \Lambda^{(\hat{a})}{}_{(b)}k^{(b)}. \tag{184}$$

C. Directional angles of photon measured in REFs

We introduce the photon directional angles $(\hat{\alpha}, \hat{\beta})$ measured in the REF, by using the quantities $k^{(\hat{a})}$ in relations analogous to the Eqs. (164)–(166). Using the transformation law given by (183) and (184), the directional angles measured in LNRF and REF at a given point can be related by the equations

$$\cos\hat{\alpha} = k^{(\hat{r})}/k^{(\hat{t})} = \frac{\cos\alpha - v}{1 - v\cos\alpha}, \tag{185}$$

and

$$\hat{\beta} = \beta. \tag{186}$$

Since we are concerned with reference frames under the cosmic repulsion, we take $v = v^{(r)} > 0$ and Eq. (185) then represents a standard formula for the aberration of light

from a receding source. Equation (186) follows immediately from the obvious transformation relations $k^{(\hat{\theta})} = k^{(\theta)}$, $k^{(\hat{\phi})} = k^{(\phi)}$.

D. Shadows of the NS as seen by REF observer near the cosmological horizon

Here we present the construction of the shadows of the KdS NSs, as seen by the REF observer approaching the cosmological horizon, for typical values of the latitude θ_o. The construction is carried out using the procedure described in Sec. IV B. If we denote the angles describing the resulting boundary of shadows in the local projection plane, which are analogous to the angles $(\tilde{\alpha}, \tilde{\beta})$ related to the LNRF observer, as $(\bar{\alpha}, \bar{\beta})$, then obviously the relations

$$\cos\bar{\alpha} = \frac{\cos\tilde{\alpha} - v}{1 - v\cos\tilde{\alpha}}, \tag{187}$$

and

$$\bar{\beta} = \tilde{\beta} \tag{188}$$

hold. In the figures below we demonstrate the effect of the aberration of light, given by the formula (187), on the dark spot determined by the photons arriving from the vicinity of the polar SPO in the region of negative radii, as it is probably the most conspicuous part of the NS image, when observed on an bright background. We present its angular diameter δ_{ax} as seen from the position on the spin axis, which gives the maximum of the observable dark area. The angular diameter is defined as

$$\bar{\delta}_{ax} \equiv 2\bar{\alpha}, \tag{189}$$

where the angle $\bar{\alpha}$ is computed from Eq. (187) for photons with the motion constants $X = -a$ $(\ell = 0)$ and $q = q_{\mathrm{SPO}}(r^{(-)}_{\mathrm{pol}})$, with $r^{(-)}_{\mathrm{pol}}$ given by relation (129) [see the corresponding yellow point in the $(X - q)$ parameter plane in the detail of Fig. 27(a), left below].

Figures 31 and 32 clearly demonstrate the decrease of the angular diameter of the dark spot for an observer approaching the cosmological horizon. Since, according to the relations (164) and (173), $\cos\tilde{\alpha} \to 1$, $v \to 1$ for $r \to r_c^-$, the formula (187) has a finite limit

$$\lim_{r\to r_c^-} \cos\bar{\alpha} < 1, \tag{190}$$

corresponding to the marginal diameter $\bar{\delta}_{ax}$ at the endpoints of the displayed curves, highlighted by dots. For comparison, we have attached curves that describe the angular diameter as seen by the LNRF observer at the same radius, defined as

$$\tilde{\delta}_{ax} \equiv 2\tilde{\alpha}, \tag{191}$$

and the angular magnification

$$\zeta \equiv \frac{\bar{\alpha}}{\tilde{\alpha}}. \tag{192}$$

In Fig. 33 we present the angular diameter of the dark spot as seen by the radially escaping observer near the cosmological horizon in dependence on the cosmological parameter y for several fixed values of the spin parameter a^2.

In order to have dimensional estimates of the distances of the sources corresponding to some astrophysically relevant mass parameter M, we express the radii of the appropriate

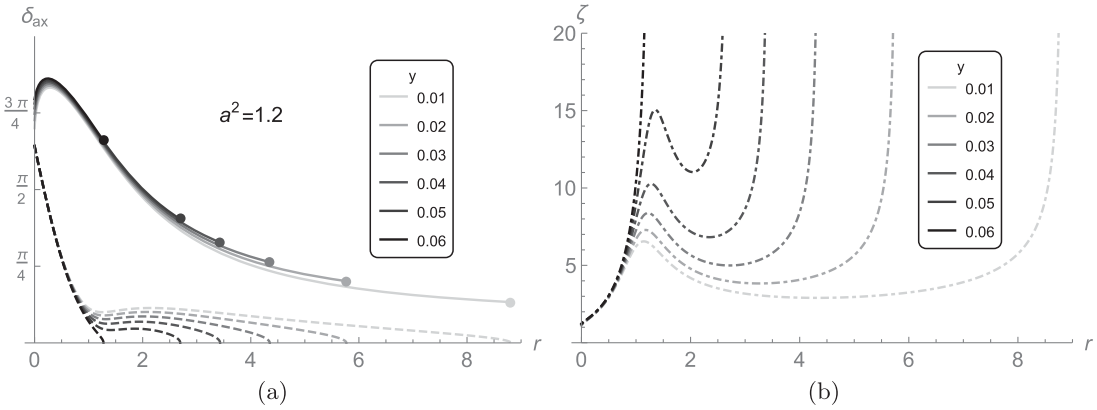

FIG. 31. (a) Angular diameter δ_{ax}, measured in radians, of the dark spot bordered by the bright circle constituted of photons coming from the vicinity of the polar SPO at negative radii $r^{(-)}_{\mathrm{pol}}$, as seen by the REF observer escaping along the spin axis, as a function of his radial distance r in the KdS spacetimes with fixed spin parameter $a^2 = 1.2$ and various cosmological parameters y (full curves), compared to the diameter observed by the LNRF observer at the same radii (dashed curves). The curves are constructed up to the radii corresponding to the loci of the individual cosmological horizons r_c, highlighted by dots. (b) Magnification of the angular diameter due to the radial motion, given by the ratio $\zeta = \bar{\alpha}/\tilde{\alpha}$. The zooming effect grows with increasing cosmological parameter y.

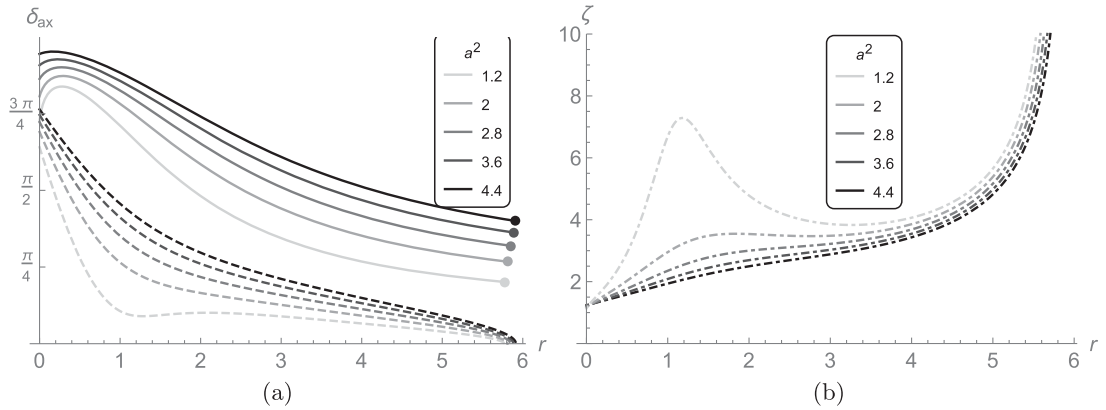

FIG. 32. (a) Angular diameter δ_{ax}, measured in radians, of the dark spot bordered by the bright circle constituted by photons coming from the vicinity of the polar SPO at negative radii $r_{\rm pol}^{(-)}$ as seen by the REF observer escaping along the spin axis, as a function of his radial distance r in the KdS spacetimes with fixed cosmological parameter $y = 0.02$ and various spin parameters a^2 (full curves), compared to the diameter observed by the LNRF observer at the same radii (dashed curves). The curves are constructed up to the radii corresponding to the loci of the individual cosmological horizons r_c, highlighted by dots. (b) Magnification of the angular diameter due to the radial motion, given by the ratio $\zeta = \tilde{\alpha}/\tilde{\alpha}$. The zooming effect grows with decreasing spin parameter a^2.

cosmological horizon in standard astronomical units. It can be shown that for a sufficiently small parameter y, the solution of the Eq. (8) for the cosmological horizon r_c is given with high accuracy in a simple form

$$r_c = \frac{1}{\sqrt{y}}. \tag{193}$$

To get an idea of the value of the parameter y for the currently estimated value of the cosmological constant $\Lambda \sim 1.1 \times 10^{-52}$ m^{-2} and some selected mass parameter M, it is convenient to express the mass parameter M in units of the mass of the Sun, $M_\odot$, that is $M = n_\odot M_\odot$, and to do the same for the parameter y. To do this, we need to express the Sun's geometric mass as

$$M_\odot = \frac{G}{c^2} M_{\odot(\rm dim)} = \left(0.743 \times 10^{-27}\ \frac{\rm m}{\rm kg}\right)(1.989 \times 10^{30}\ {\rm kg}) \sim 1.5 \times 10^3\ {\rm m}, \tag{194}$$

where $M_{\odot(\rm dim)} = 1.989 \times 10^{30}$ kg is the mass of the Sun in standard dimensional units. Now we can write

$$y = \frac{1}{3}\Lambda M^2 = \frac{1}{3}\Lambda (n_\odot M_\odot)^2 = \frac{1}{3}(1.1 \times 10^{-52}\ {\rm m}^{-2})(1.5 \times 10^3\ {\rm m})^2 n_\odot^2 \sim 8 \times 10^{-47} n_\odot^2. \tag{195}$$

It follows from Eq. (195) that the sufficient smallness of the parameter y is safely satisfied for all astrophysically relevant values of $n_\odot \leq 10^{12}$. Now it follows from (193) and (195) that although the cosmological parameter y and the corresponding value r_c can have very different values for different choices of $n_\odot$, the dimensional value

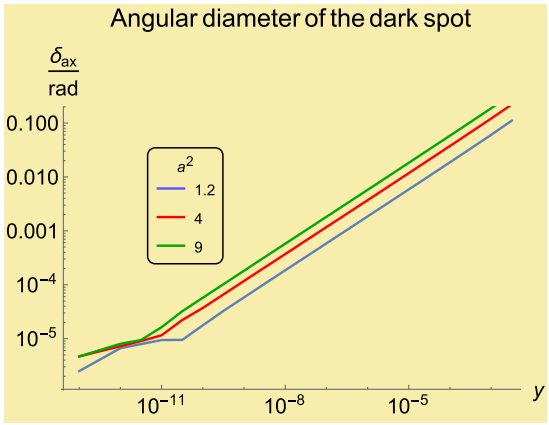

FIG. 33. The angular diameter δ_{ax}, measured in radians, of the dark spot as seen by the REF observer radially approaching the cosmological horizon $[r_o = (1 - 10^{-5})r_c]$ along the spin axis in the KdS spacetimes with fixed spin parameter $a^2 = 1.2$ as a function of the cosmological parameter y. The curves are constructed up to radii corresponding to the loci of the individual cosmological horizons r_c, highlighted by dots.

TABLE V. Angular diameter of the dark spot.

$n_\odot$	$\delta_{ax}(\mu{\rm as})$
4×10^6	3×10^{-5}
6×10^9	4.6×10^{-2}
7×10^{10}	0.53
10^{12}	7.6

$$r_{c(\mathrm{dim})} = r_c M = \frac{M}{\sqrt{1/3\Lambda M^2}} = \sqrt{\frac{3}{\Lambda}} \tag{196}$$

is independent of the mass and spin parameters. Its value reads

$$r_{c(\mathrm{dim})} = \left(\sqrt{\frac{3}{1.1\times 10^{-52}}}\ \mathrm{m}\right)\left(\frac{1}{9.5\times 10^{15}}\ \frac{ly}{\mathrm{m}}\right) = 1.74\times 10^{10}\ ly. \tag{197}$$

In the following table we assume that the shadow is defined by a bright background composed of light sources at distances corresponding to the most distant galaxies observed so far at a redshift of $z \gtrsim 10$ [140]. We therefore put the observer at a radial distance of $r_{o(\mathrm{dim})} = 1.45\times 10^{10}\ ly = 0.83 r_{c(\mathrm{dim})}$.

The mass parameters $M = 4\times 10^6 M_\odot$, $6\times 10^9 M_\odot$, $7\times 10^{10} M_\odot$ and $10^{12} M_\odot$ correspond, respectively, to the BH mass at the center of our galaxy Sgr A*, the galaxy M87, the most massive BHs observed so far TON 618, and a theoretical limit for the BH mass expected in galaxy clusters. It follows from the Table V that the angular diameters are below the angular resolution of the EHT telescope $\sim 10\ \mu$as. However, this result shows that in the extreme cases such subtle details might be within the range of the future space observatories performing the interferometric measurements on long baselines.

We end this section by presenting the KdS NS shadows as seen by the REF observer gradually approaching the cosmological horizon at representative latitudes $\theta_o = 0°, 45°, 90°$ and radii $r_o = 0.8 r_c, 0.9 r_c, 0.999 r_c$, (see Fig. 34).

VI. DISCUSSION AND CONCLUDING REMARKS

We have studied the geometric and geodesic properties of the KdS NS spacetimes, including the region of negative radii, and made a comparison with the properties of the KdS BH spacetimes. We have performed the construction of the shadows of the class IVa KdS NS spacetimes admitted by the astrophysical and cosmological restrictions on the mass and spin of the compact (or gravitationally bound) objects, and the cosmological restrictions on the dark energy or the cosmological constant.

For the construction of the shadow of the considered KdS NSs, we have used two families of reference frames, the first one accelerated, so called LNRFs, where the most convenient choice of the observer's position is on the static radius, and the second one geodesic, so called REFs, where the frame (observer) is pulled outwards by the cosmic repulsion, that can be astrophysically relevant for the construction of the shadows as seen near the cosmological horizon. In all the constructions, the photons entering the region of negative radii are fully taken into account. We summarize some important results related to observations in these two families of reference frames:

LNRF

(1) The apparent shape of the KdS NS shadow, as appears on observer's celestial sky, consists of two parts; an arc or circle, related to the light rays incoming from the bright background and winding up the unstable spherical photon orbits at positive radial coordinates $r > 0$, and a dark spot, determined by the light entering the region of negative radii $r < 0$ and escaping to $r \to -\infty$.

(2) In the region of negative radii $r < 0$, there exists a potential barrier that repels the incoming photons back to $r > 0$. The borderline in the plane $(X - q)$, which divides the motion constants corresponding to repelled photons and photons escaping to $r \to -\infty$, is given by the curve $(X_{\mathrm{SPO}}(r_{\mathrm{SPO}}), q_{\mathrm{SPO}}(r_{\mathrm{SPO}}))$, i.e., by "a critical locus" (Fig. 15), where the parameter r_{SPO} corresponds to unstable spherical photon orbits in the region $r < 0$. Behavior of this curve is qualitatively the same in all classes of the KdS spacetimes with spacetime parameters satisfying condition $a^2 y < 1$. Photons escaping to $r \to -\infty$ are regarded as being captured by the NS.

(3) The SPOs at negative radii determine the really observed boundary of the NS shadow.

(4) The PNC photons and the θ^* photons delimit the angular size of the major axis of the ellipse, which is the NS silhouette for an observer located near the equatorial plane [see Fig. 29(a)].

(5) For the exact position in the equatorial plane, this ellipse shrinks by a leap into the abscissa [Fig. 29(b)] with the angular size delimited by the PNC photon (cf. [133]) and the photon with the impact parameter corresponding to the equatorial circular photon orbit $X = X_{\mathrm{ph}-}$.

(6) The dark purple area represents a dark spot on the observer's celestial sphere, since no photons from a bright background can come from these directions, while the light purple area represents a reflection of the light radiated from the region $r > 0$ at negative radii. the visibility of this region could be highlighted, if there were some sources of illumination, e.g., radiating matter in the accretion disk orbiting the NS. The outer edge of this visible region is bounded by the NS.

REF

(1) The motion of the REF observer causes the aberration of light, resulting in an angular magnification of the NS image compared to the LNRF observer's observation, without distortion.

(2) The angular magnification increases as the cosmological parameter y increases and as the spin parameter a^2 decreases.

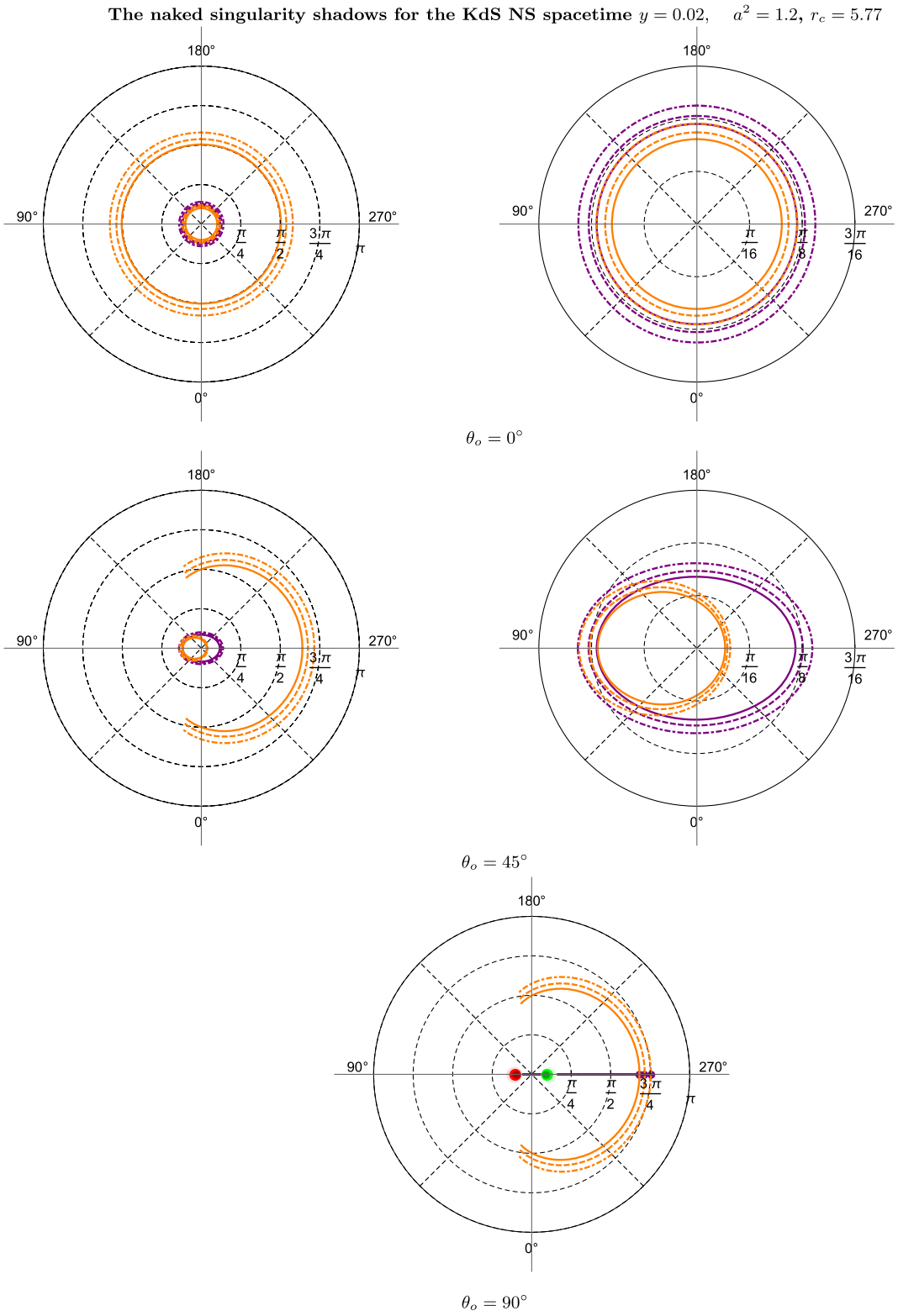

FIG. 34. NS shadows observed in the radially escaping reference frames of the KdS spacetime with spin parameter $a^2 = 1.2$ and cosmological parameter $y = 0.02$ at radii approaching the cosmological horizon at $r_c = 5.77$ and at appropriate observer's latitudes θ_0. Dot-dashed, dashed and full curves correspond to observer's radii $r_o = 0.8r_c, 0.9r_c, 0.999r_c$, respectively; the color of the curves corresponds to their significance as introduced in Figs. 27–29. The figures in pairs, if present, describe the whole $(\bar{\alpha}, \bar{\beta})$ plane (left column) and details of the central parts (right column). The shading corresponding to photons entering the region of negative radii is not displayed for clarity.

(3) The aberration formula (187) implies that the angular diameter of the image of the spot has finite value even at the cosmological horizon $r = r_c$, although it is zero according to the LNRF observation.

We can conclude that KdS NSs, of the type corresponding to the observational limits of their spacetime parameters, exhibit shadows and associated structures that allow them to be clearly distinguished from the BH shadows. Comparing our results with those presented in the case of the KdS BHs [97], we can stress the main differences in the character of the shadow. The main, qualitative difference is given by the existence of the arc, typical of the NS spacetimes; note that for sufficiently small inclination angles of the observer with respect to the rotation axis of the KdS spacetime, the arc is extended to a full circle (see Fig. 27). Inside of the arc an elongated shadow occurs, the elongation of which increases with the angle of inclination of the observer. Both these parts of the NSs shadow demonstrate clear differences from the BHs shadow. We can say that the current observations of the Event Horizon Telescope in the M87 galaxy [1–8], and the Sgr A* in the Galaxy center [9–14], i.e., two sources for which the shadows constructed relative to the LNRFs are relevant, clearly demonstrate the existence of the BH horizon, and give no signatures of the NS effects on the observed shadows.

On the other hand, the hypothetical primordial rotating NSs (superspinars), advocated by some stringy theorists as possible remnants of the very early era of the Universe expansion [62,63], are still in the play, because their evolution by accretion processes suggests that the existence of such NSs could be possible at the cosmological redshifts $z > 2$, as they should later be transformed into BHs [65,66]. Such hypothetical objects, located at large distances and high-cosmological redshifts could be observed by the ATHENA satellite observatory, which is currently under development.

ACKNOWLEDGMENTS

The authors acknowledge support of the Research Centre for Theoretical Physics and Astrophysics, Institute of Physics, Silesian University in Opava.

[1] K. Akiyama *et al.*, First M87 Event Horizon Telescope results. I. The shadow of the supermassive black hole, Astrophys. J. Lett. **875**, L1 (2019).
[2] K. Akiyama *et al.*, First M87 Event Horizon Telescope results. II. Array and instrumentation, Astrophys. J. Lett. **875**, L2 (2019).
[3] K. Akiyama *et al.*, First M87 Event Horizon Telescope results. III. Data processing and calibration, Astrophys. J. Lett. **875**, L3 (2019).
[4] K. Akiyama *et al.*, First M87 Event Horizon Telescope results. IV. Imaging the central supermassive black hole, Astrophys. J. Lett. **875**, L4 (2019).
[5] K. Akiyama *et al.*, First M87 Event Horizon Telescope results. V. Physical origin of the asymmetric ring, Astrophys. J. Lett. **875**, L5 (2019).
[6] K. Akiyama *et al.*, First M87 Event Horizon Telescope results. VI. The shadow and mass of the central black hole, Astrophys. J. Lett. **875**, L6 (2019).
[7] K. Akiyama *et al.*, First M87 Event Horizon Telescope results. VII. Polarization of the ring, Astrophys. J. Lett. **910**, L12 (2021).
[8] K. Akiyama *et al.*, First M87 Event Horizon Telescope results. VIII. Magnetic field structure near the event horizon, Astrophys. J. Lett. **910**, L13 (2021).
[9] K. Akiyama *et al.*, First Sagittarius A* Event Horizon Telescope results. I. The shadow of the supermassive black hole in the center of the Milky Way, Astrophys. J. Lett. **930**, L12 (2022).
[10] K. Akiyama *et al.*, First Sagittarius A* Event Horizon Telescope results. II. EHT and multiwavelength observations, data processing, and calibration, Astrophys. J. Lett. **930**, L13 (2022).
[11] K. Akiyama *et al.*, First Sagittarius A* Event Horizon Telescope results. III. Imaging of the Galactic center supermassive black hole, Astrophys. J. Lett. **930**, L14 (2022).
[12] K. Akiyama *et al.*, First Sagittarius A* Event Horizon Telescope results. IV. Variability, morphology, and black hole mass, Astrophys. J. Lett. **930**, L15 (2022).
[13] K. Akiyama *et al.*, First Sagittarius A* Event Horizon Telescope results. V. Testing astrophysical models of the Galactic center black hole, Astrophys. J. Lett. **930**, L16 (2022).
[14] K. Akiyama *et al.*, First Sagittarius A* Event Horizon Telescope results. VI. Testing the black hole metric, Astrophys. J. Lett. **930**, L17 (2022).
[15] C. W. Misner, K. S. Thorne, and J. A. Wheeler, *Gravitation* (W. H. Freeman and Company, San Francisco, 1973).
[16] J. L. Synge, Escape of photons from gravitationally intense stars, Mon. Not. R. Astron. Soc. **131**, 463 (1966).
[17] J.-P. Luminet, Image of a spherical black hole with thin accretion disk, Astron. Astrophys. **75**, 228 (1979).
[18] J. M. Bardeen, Timelike and null geodesics in the Kerr metric, in *Black Holes (Les Astres Occlus)*, edited by C. Dewitt and B. S. Dewitt (Gordon and Breach Science Publishers, New York, London, Paris, 1973), pp. 215–239.
[19] J. M. Bardeen, W. H. Press, and S. A. Teukolsky, Rotating black holes: Locally nonrotating frames, energy extraction, and scalar synchrotron radiation, Astrophys. J. **178**, 347 (1972).

[20] C. T. Cunningham and J. M. Bardeen, The optical appearance of a star orbiting an extreme Kerr black hole, Astrophys. J. **173**, L137 (1972).

[21] R. Konoplya, Z. Stuchlík, and A. Zhidenko, Echoes of compact objects: New physics near the surface and matter at a distance, Phys. Rev. D **99**, 024007 (2019).

[22] U. Alam and V. Sahni, Confronting braneworld cosmology with supernova data and baryon oscillations, Phys. Rev. D **73**, 084024 (2006).

[23] A. Kotrlová, Z. Stuchlík, and G. Török, Quasiperiodic oscillations in a strong gravitational field around neutron stars testing braneworld models, Classical Quantum Gravity **25**, 225016 (2008).

[24] J. Schee and Z. Stuchlík, Optical phenomena in the field of braneworld Kerr black holes, Int. J. Mod. Phys. D **18**, 983 (2009).

[25] J. Schee and Z. Stuchlík, Profiles of emission lines generated by rings orbiting braneworld Kerr black holes, Gen. Relativ. Gravit. **41**, 1795 (2009).

[26] Z. Stuchlík and A. Kotrlová, Orbital resonances in discs around braneworld Kerr black holes, Gen. Relativ. Gravit. **41**, 1305 (2009).

[27] A. Abdujabbarov, M. Amir, B. Ahmedov, and S. G. Ghosh, Shadow of rotating regular black holes, Phys. Rev. D **93**, 104004 (2016).

[28] J. Bardeen, Non-singular general-relativistic gravitational collapse, in *Conference Proceedings of GR5* (World Scientific Publ Co PTE LTD, Singapore, 1968).

[29] J. Schee and Z. Stuchlík, Effective geometry of the Bardeen spacetimes: Gravitational lensing and frequency mapping of Keplerian disks, Astrophys. J. **874**, 12 (2019).

[30] Z. Stuchlík and J. Schee, Circular geodesic of Bardeen and Ayon-Beato-Garcia regular black-hole and no-horizon spacetimes, Int. J. Mod. Phys. D **24**, 1550020 (2015).

[31] Z. Stuchlík, J. Schee, and D. Ovchinnikov, Generic regular black holes related to nonlinear electrodynamics with Maxwellian weak-field limit: Shadows and images of Keplerian disks, Astrophys. J. **887**, 145 (2019).

[32] Z. Stuchlík and J. Schee, Shadow of the regular Bardeen black holes and comparison of the motion of photons and neutrinos, Eur. Phys. J. C **79**, 44 (2019).

[33] A. Abdujabbarov, B. Toshmatov, J. Schee, Z. Stuchlík, and B. Ahmedov, Gravitational lensing by regular black holes surrounded by plasma, Int. J. Mod. Phys. D **26**, 1741011 (2017).

[34] E. Contreras, J. Ovalle, and R. Casadio, Gravitational decoupling for axially symmetric systems and rotating black holes, Phys. Rev. D **103**, 044020 (2021).

[35] R. Konoplya, Shadow of a black hole surrounded by dark matter, Phys. Lett. B **795**, 1 (2019).

[36] B.-H. Lee, W. Lee, and Y. S. Myung, Shadow cast by a rotating black hole with anisotropic matter, Phys. Rev. D **103**, 064026 (2021).

[37] R. C. Pantig and E. T. Rodulfo, Rotating dirty black hole and its shadow, Chin. J. Phys. **68**, 236 (2020).

[38] Z. Stuchlík and J. Vrba, Supermassive black holes surrounded by dark matter modeled as anisotropic fluid: Epicyclic oscillations and their fitting to observed QPOs, J. Cosmol. Astropart. Phys. 11 (2021) 059.

[39] Z. Stuchlík and J. Vrba, Geodesic model of HF QPOs tested for black holes in spacetimes reflecting the effect of surrounding dark matter, Astrophys. J. **935**, 91 (2022).

[40] A. Belhaj, M. Benali, A. El Balali, W. El Hadri, H. El Moumni, and E. Torrente-Lujan, Black hole shadows in M-theory scenarios, Int. J. Mod. Phys. D **30**, 2150026 (2021).

[41] T. Zhu, Q. Wu, M. Jamil, and K. Jusufi, Shadows and deflection angle of charged and slowly rotating black holes in Einstein-Æther theory, Phys. Rev. D **100**, 044055 (2019).

[42] A. Övgün and z. Sakallı (I. Sakalli), Testing generalized Einstein-Cartan-Kibble-Sciama gravity using weak deflection angle and shadow cast, Classical Quantum Gravity **37**, 225003 (2020).

[43] A. Abdujabbarov, F. Atamurotov, N. Dadhich, B. Ahmedov, and Z. Stuchlík, Energetics and optical properties of 6-dimensional rotating black hole in pure Gauss–Bonnet gravity, Eur. Phys. J. C **75**, 399 (2015).

[44] M. Shahzadi, M. Kolos, Z. Stuchlík, and Y. Habib, Testing alternative theories of gravity by fitting the hot-spot data of Sgr A*, Eur. Phys. J. C **82**, 407 (2022).

[45] K. Nakao, N. Kobayashi, and H. Ishihara, How does a naked singularity look, Phys. Rev. D **67**, 084002 (2003).

[46] R. Shaikh, P. Kocherlakota, R. Narayan, and P. S. Joshi, Shadows of spherically symmetric black holes and naked singularities, Mon. Not. R. Astron. Soc. **482**, 52 (2018).

[47] P. Bambhaniya, D. Dey, A. B. Joshi, P. S. Joshi, D. N. Solanki, and A. Mehta, Shadows and negative precession in non-Kerr spacetime, Phys. Rev. D **103**, 084005 (2021).

[48] M. Churilova, R. Konoplya, Z. Stuchlík, and A. Zhidenko, Wormholes without exotic matter: Quasinormal modes, echoes and shadows, J. Cosmol. Astropart. Phys. 10 (2021) 010.

[49] J. Schee and Z. Stuchlík, Appearance of Keplerian discs orbiting on both sides of reflection-symmetric wormholes, J. Cosmol. Astropart. Phys. 01 (2022) 054.

[50] Z. Stuchlík and J. Vrba, Epicyclic orbits in the field of Einstein–Dirac–Maxwell traversable wormholes applied to the quasiperiodic oscillations observed in microquasars and active galactic nuclei, Eur. Phys. J. Plus **136**, 1127 (2021).

[51] M. Wielgus, J. Horák, F. Vincent, and M. Abramowicz, Reflection-asymmetric wormholes and their double shadows, Phys. Rev. D **102**, 084044 (2020).

[52] A. Abdujabbarov, B. Juraev, B. Ahmedov, and Z. Stuchlík, Shadow of rotating wormhole in plasma environment, Astrophys. Space Sci. **361**, 226 (2016).

[53] J. Schee and Z. Stuchlík, Profiled spectral lines generated in the field of Kerr superspinars, J. Cosmol. Astropart. Phys. 04 (2013) 005.

[54] Z. Stuchlík and J. Schee, Appearance of Keplerian discs orbiting Kerr superspinars, Classical Quantum Gravity **27**, 215017 (2010).

[55] M. Blaschke and Z. Stuchlík, Efficiency of the Keplerian accretion in braneworld Kerr-Newman spacetimes and mining instability of some naked singularity spacetimes, Phys. Rev. D **94**, 086006 (2016).

[56] P. Slaný and Z. Stuchlík, Equatorial circular orbits in Kerr-Newman-de Sitter spacetimes, Eur. Phys. J. C **80**, 587 (2020).
[57] Z. Stuchlík, M. Blaschke, and J. Schee, Particle collisions and optical effects in the mining Kerr-Newman spacetimes, Phys. Rev. D **96**, 104050 (2017).
[58] V. Balek, J. Bičák, and Z. Stuchlík, The motion of the charged particles in the field of rotating charged black holes and naked singularities. II. The motion in the equatorial plane, Bull. Astron. Inst. Czech. **40**, 133 (1989).
[59] M. A. Abramowicz, W. Kluźniak, and J.-P. Lasota, No observational proof of the black-hole event-horizon, Astron. Astrophys. **396**, L31 (2002).
[60] M. Calvani, F. de Felice, B. Muchotrzeb, and F. Salmistraro, Time machine and geodesic motion in Kerr metric, Gen. Relativ. Gravit. **9**, 155 (1978).
[61] B. Carter, Black hole equilibrium states, in *Black Holes (Les Astres Occlus)*, edited by C. Dewitt and B. S. Dewitt (Elsevier, Taiwan, 1973), pp. 57–214.
[62] E. K. Boyda, S. Ganguli, P. Hořava, and U. Varadarajan, Holographic protection of chronology in universes of the Gödel type, Phys. Rev. D **67**, 106003 (2003).
[63] E. G. Gimon and P. Hořava, Astrophysical violations of the Kerr bound as a possible signature of string theory, Phys. Lett. B **672**, 299 (2009).
[64] E. G. Gimon and P. Hořava, Over-rotating black holes, Godel holography and the hypertube (2004).
[65] Z. Stuchlík, S. Hledík, and K. Truparová, Evolution of Kerr superspinars due to accretion counterrotating thin discs, Classical Quantum Gravity **28**, 155017 (2011).
[66] Z. Stuchlík and J. Schee, Observational phenomena related to primordial Kerr superspinars, Classical Quantum Gravity **29**, 065002 (2012).
[67] C. Chakraborty, P. Kocherlakota, and P. S. Joshi, Spin precession in a black hole and naked singularity spacetimes, Phys. Rev. D **95**, 044006 (2017).
[68] V. Perlick and O. Y. Tsupko, Calculating black hole shadows: Review of analytical studies, Phys. Rep. **947**, 1 (2022).
[69] R. Penrose, Gravitational collapse: The role of general relativity, Nuovo Cimento B **1**, 252 (1969).
[70] Y. C. Ong, Spacetime singularities and cosmic censorship conjecture: A review with some thoughts, Int. J. Mod. Phys. A **35**, 2030007 (2020).
[71] S. Shaymatov and N. Dadhich, Extending the weak cosmic censorship conjecture to the charged Buchdahl star by employing the gedanken experiments, J. Cosmol. Astropart. Phys. 06 (2023) 010.
[72] V. E. Hubeny, Overcharging a black hole and cosmic censorship, Phys. Rev. D **59**, 064013 (1999).
[73] S. Shaymatov, M. Patil, B. Ahmedov, and P. S. Joshi, Destroying a near-extremal Kerr black hole with a charged particle: Can a test magnetic field serve as a cosmic censor?, Phys. Rev. D **91**, 064025 (2015).
[74] R. Wald, Gedanken experiments to destroy a black hole, Ann. Phys. (N.Y.) **82**, 548 (1974).
[75] T. Jacobson and T. P. Sotiriou, Overspinning a black hole with a test body, Phys. Rev. Lett. **103**, 141101 (2009).
[76] J. Natario and R. Vicente, Test fields cannot destroy extremal de Sitter black holes, Gen. Relativ. Gravit. **52**, 5 (2020).
[77] J. Natário, L. Queimada, and R. Vicente, Test fields cannot destroy extremal black holes, Classical Quantum Gravity **33**, 175002 (2016).
[78] S. Shaymatov, N. Dadhich, and B. Ahmedov, The higher dimensional Myers–Perry black hole with single rotation always obeys the cosmic censorship conjecture, Eur. Phys. J. C **79**, 585 (2019).
[79] S. Shaymatov, N. Dadhich, and B. Ahmedov, Six-dimensional Myers-Perry rotating black hole cannot be overspun, Phys. Rev. D **101**, 044028 (2020).
[80] J. Sorce and R. M. Wald, Gedanken experiments to destroy a black hole. II. Kerr-Newman black holes cannot be overcharged or overspun, Phys. Rev. D **96**, 104014 (2017).
[81] I. Dwivedi and P. Joshi, Cosmic censorship violation in non-self-similar Tolman-Bondi models, Classical Quantum Gravity **9**, L69 (1992).
[82] P. Joshi and I. Dwivedi, Naked singularities in spherically symmetric inhomogeneous Tolman-Bondi dust cloud collapse, Phys. Rev. D **47**, 5357 (1993).
[83] P. S. Joshi, N. Dadhich, and R. Maartens, Why do naked singularities form in gravitational collapse?, Phys. Rev. D **65**, 101501 (2002).
[84] P. S. Joshi, R. Goswami, and N. Dadhich, Why do naked singularities form in gravitational collapse? II, Phys. Rev. D **70**, 087502 (2004).
[85] K.-i. Nakao, P. S. Joshi, J.-Q. Guo, P. Kocherlakota, H. Tagoshi, T. Harada, M. Patil, and A. Królak, On the stability of a superspinar, Phys. Lett. B **780**, 410 (2018).
[86] A. D. Dolgov, J. B. Zeldovich, and M. V. Sazhin, *Kosmologia Rannej Vcelennoy* (Izd. Moskovskovo Universiteta, Bristol, 1988).
[87] M. Kamionkowski, T. Smith, and A. Heavens, The CMB bispectrum, trispectrum, non-Gaussianity, and the Cramer-Rao bound, Phys. Rev. D **83**, 023007 (2010).
[88] Z. Stuchlík, The motion of test particles in black-hole backgrounds with non-zero cosmological constant, Bull. Astron. Inst. Czech. **34**, 129 (1983).
[89] Z. Stuchlík, An Einstein–Strauss–de Sitter model of the universe, Bull. Astron. Inst. Czech. **35**, 205 (1984).
[90] P. Slaný and Z. Stuchlík, Relativistic thick discs in the Kerr–de Sitter backgrounds, Classical Quantum Gravity **22**, 3623 (2005).
[91] Z. Stuchlík, Influence of the relict cosmological constant on accretion discs, Mod. Phys. Lett. A **20**, 561 (2005).
[92] Z. Stuchlík, P. Slaný, and S. Hledík, Equilibrium configurations of perfect fluid orbiting Schwarzschild–de Sitter black holes, Astron. Astrophys. **363**, 425 (2000).
[93] Z. Stuchlík, P. Slaný, and J. Kovář, Pseudo-Newtonian and general relativistic barotropic tori in Schwarzschild–de Sitter spacetimes, Classical Quantum Gravity **26**, 215013 (2009).
[94] Z. Stuchlík, M. Kološ, J. Kovář, P. Slaný, and A. Tursunov, Influence of cosmic repulsion and magnetic fields on accretion disks rotating around Kerr black holes, Universe **6**, 26 (2020).

[95] Z. Stuchlík, S. Hledík, and J. Novotný, General relativistic polytropes with a repulsive cosmological constant, Phys. Rev. D **94**, 103513 (2016).
[96] Z. Stuchlík and J. Schee, Influence of the cosmological constant on the motion of magellanic clouds in the gravitational field of Milky Way, J. Cosmol. Astropart. Phys. 09 (2011) 018.
[97] Z. Stuchlík, D. Charbulák, and J. Schee, Light escape cones in local reference frames of Kerr–de Sitter black hole spacetimes and related black hole shadows, Eur. Phys. J. C **78**, 180 (2018).
[98] E. Omwoyo, H. Belich, J. C. Fabris, and H. Velten, Remarks on the black hole shadows in Kerr-de Sitter space times, Eur. Phys. J. C **82**, 395 (2022).
[99] J. Ovalle, E. Contreras, and Z. Stuchlík, Kerr–de Sitter black hole revisited, Phys. Rev. D **103**, 084016 (2021).
[100] Z. Chang and Q.-H. Zhu, *Influence of Earth's Orbit on the Shadow of Sgr A** (2021).
[101] I. I. Cotăescu, Light from Schwarzschild black holes in de Sitter expanding universe, Eur. Phys. J. C **81**, 32 (2021).
[102] V. Perlick, O. Y. Tsupko, and G. S. Bisnovatyi-Kogan, Black hole shadow in an expanding universe with a cosmological constant, Phys. Rev. D **97**, 104062 (2018).
[103] R. Roy and S. Chakrabarti, Study on black hole shadows in asymptotically de Sitter spacetimes, Phys. Rev. D **102**, 024059 (2020).
[104] A. Belhaj, M. Benali, A. E. Balali, W. E. Hadri, and H. El Moumni, Shadows of charged and rotating black holes with a cosmological constant (2020).
[105] P.-C. Li, M. Guo, and B. Chen, Shadow of a spinning black hole in an expanding universe, Phys. Rev. D **101**, 084041 (2020).
[106] Z. Chang and Q.-H. Zhu, Revisiting a rotating black hole shadow with astrometric observables, Phys. Rev. D **101**, 084029 (2020).
[107] Z. Stuchlík and S. Hledík, Some properties of the Schwarzschild–de Sitter and Schwarzschild–anti-de Sitter spacetimes, Phys. Rev. D **60**, 044006 (1999).
[108] Z. Stuchlík and P. Slaný, Equatorial circular orbits in the Kerr–de Sitter spacetimes, Phys. Rev. D **69**, 064001 (2004).
[109] Z. Stuchlík, J. Schee, B. Toshmatov, J. Hladík, and J. Novotný, Gravitational instability of polytropic spheres containing region of trapped null geodesics: A possible explanation of central supermassive black holes in galactic halos, J. Cosmol. Astropart. Phys. 17 (2017) 056.
[110] D. Charbulák and Z. Stuchlík, Photon motion in Kerr–de Sitter spacetimes, Eur. Phys. J. C **77**, 897 (2017).
[111] Z. Stuchlík, The motion of test particles in black-hole backgrounds with non-zero cosmological constant, Bull. Astron. Inst. Czech. **34**, 129 (1983).
[112] R. H. Boyer and R. W. Lindquist, Maximal analytic extension of the Kerr metric, J. Math. Phys. (N.Y.) **8**, 265 (1967).
[113] P. T. Chruściel, C. R. Ölz, and S. J. Szybka, Space-time diagrammatics, Phys. Rev. D **86**, 124041 (2012).
[114] S. Akcay and R. A. Matzner, The Kerr–de Sitter universe, Classical Quantum Gravity **28**, 085012 (2011).
[115] M. Kološ, A. Tursunov, and Z. Stuchlík, Radiative Penrose process: Energy gain by a single radiating charged particle in the ergosphere of rotating black hole, Phys. Rev. D **103**, 024021 (2021).
[116] R. Penrose and R. M. Floyd, Extraction of rotational energy from a black hole, Nat. Phys. Sci. **229**, 177 (1971).
[117] Z. Stuchlík, Equatorial circular orbits and the motion of the shell of dust in the field of a rotating naked singularity, Bull. Astron. Inst. Czech. **31**, 129 (1980).
[118] Z. Stuchlík, M. Kološ, and A. Tursunov, Penrose process: Its variants and astrophysical applications, Universe **7**, 416 (2021).
[119] A. Tursunov, Z. Stuchlík, M. Kološ, N. Dadhich, and B. Ahmedov, Supermassive black holes as possible sources of ultrahigh-energy cosmic rays, Astrophys. J. **895**, 14 (2020).
[120] N. Dadhich, A. Tursunov, B. Ahmedov, and Z. Stuchlík, The distinguishing signature of magnetic Penrose process, Mon. Not. R. Astron. Soc. **478**, L89 (2018).
[121] D. Pugliese and H. Quevedo, The ergoregion in the Kerr spacetime: Properties of the equatorial circular motion, Eur. Phys. J. C **75**, 234 (2015).
[122] D. Pugliese and H. Quevedo, Observers in Kerr spacetimes: The ergoregion on the equatorial plane, Eur. Phys. J. C **78**, 69 (2018).
[123] D. Pugliese and H. Quevedo, Disclosing connections between black holes and naked singularities: Horizon remnants, Killing throats and bottlenecks, Eur. Phys. J. C **79**, 209 (2019).
[124] D. Pugliese and Z. Stuchlík, Embedded BHS and multipole globules: Clustered misaligned thick accretion disks around static SMBHs, Classical Quantum Gravity **37**, 195025 (2020).
[125] D. Pugliese and Z. Stuchlík, General relativistic rotational energy extraction from black holes-accretion disk systems, Classical Quantum Gravity **38**, 145014 (2021).
[126] K. Lake and T. Zannias, Global structure of Kerr-de Sitter spacetimes, Phys. Rev. D **92**, 084003 (2015).
[127] At the static radius, introduced for spherically symmetric Schwarzschild-de Sitter spacetimes in [88], the gravitational attraction of the central object is just balanced by the cosmic repulsion, and a "geodesic" observer located at the static radius in an unstable equilibrium position has only a non-zero time component U^t of its four-velocity. In the KdS spacetimes, the unstable equilibrium position of an observer at the static radius again exists in the equatorial plane; the radius is independent of the spin parameter a—for details see [108].
[128] S. Bhattacharya, Kerr-de Sitter spacetime, Penrose process, and the generalized area theorem, Phys. Rev. D **97**, 084049 (2018).
[129] B. Carter, Global structure of the Kerr family of gravitational fields, Phys. Rev. **174**, 1559 (1968).
[130] Z. Stuchlík and S. Hledík, Equatorial photon motion in the Kerr–Newman spacetimes with a non-zero cosmological constant, Classical Quantum Gravity **17**, 4541 (2000).
[131] J. Bičák and Z. Stuchlík, On the latitudinal and radial motion in the field of a rotating black hole, Bull. Astron. Inst. Czech. **27**, 129 (1976).
[132] Z. Stuchlík, G. Bao, E. Østgaard, and S. Hledík, Kerr-Newman-de Sitter black holes with a restricted repulsive

barrier of equatorial photon motion, Phys. Rev. D **58**, 084003 (1998).

[133] K. Hioki and K.-i. Maeda, Measurement of the Kerr spin parameter by observation of a compact object's shadow, Phys. Rev. D **80**, 024042 (2009).

[134] D. Charbulák and Z. Stuchlík, Spherical photon orbits in the field of Kerr naked singularities, Eur. Phys. J. C **78**, 879 (2018).

[135] E. Teo, Spherical photon orbits around a Kerr black hole, Gen. Relativ. Gravit. **35**, 1909 (2003).

[136] In the Kerr and KdS NS spacetimes, there exists a stable SPO located below the unstable SPO, and a vortex of photons following trapped null geodesics is determined by these two SPOs [54,110]. Such vortex of photons may be important in the case of Keplerian accretion disks entering the region of their existence [54], but it is irrelevant for the determination of the shadow of NSs by distant observers, so we do not consider the stable SPOs in the present paper.

[137] S. U. Viergutz, Image generation in Kerr geometry. I. Analytical investigations on the stationary emitter-observer problem, Astron. Astrophys. **272**, 355 (1993).

[138] J. Schee, Z. Stuchlík, and J. Juráň, Light escape cones and raytracing in Kerr geometry, in *RAGtime 6/7: Workshops on Black Holes and Neutron Stars*, edited by S. Hledík and Z. Stuchlík (Silesian University in Opava, Hradec nad Moravicí, Opava, 2005), pp. 143–155.

[139] J. Bičák and Z. Stuchlík, The fall of the shell of dust on to a rotating black hole, Mon. Not. R. Astron. Soc. **175**, 381 (1976).

[140] R. P. Naidu *et al.*, Two remarkably luminous galaxy candidates at $z \approx 10$–12 revealed by JWST, Astrophys. J. Lett. **940**, L14 (2022).